



# Multi-scale Analysis of the Fatigue of Shape Memory Alloys

Lin Zheng

## ► To cite this version:

Lin Zheng. Multi-scale Analysis of the Fatigue of Shape Memory Alloys. Solid mechanics [physics.class-ph]. Université Paris Saclay (COmUE), 2016. English. NNT : 2016SACLY011 . tel-01422026

**HAL Id: tel-01422026**

**<https://pastel.hal.science/tel-01422026>**

Submitted on 23 Dec 2016

**HAL** is a multi-disciplinary open access archive for the deposit and dissemination of scientific research documents, whether they are published or not. The documents may come from teaching and research institutions in France or abroad, or from public or private research centers.

L'archive ouverte pluridisciplinaire **HAL**, est destinée au dépôt et à la diffusion de documents scientifiques de niveau recherche, publiés ou non, émanant des établissements d'enseignement et de recherche français ou étrangers, des laboratoires publics ou privés.

NNT : 2016SACLAY011

THESE DE DOCTORAT  
DE  
L'UNIVERSITE PARIS-SACLAY  
PREPAREE A  
L'ECOLE NATIONALE SUPERIEURE DE TECHNIQUES AVANCEES

ÉCOLE DOCTORALE N°579  
Sciences Mécaniques et Energétiques, Matériaux et Géosciences  
Spécialité de doctorat : Mécanique des Solides

Par

**Mme Lin ZHENG**

Multi-scale Analysis of the Fatigue of Shape Memory Alloys

**Thèse présentée et soutenue à Palaiseau, le 28 septembre 2016:**

**Composition du Jury :**

M. E. Charkaluk, Directeur de Recherche, Université Lille1 Sciences et Technologies, Président  
M. T. Ben Zineb, Professeur des Universités, Université de Lorraine (LEMTA – ESSTIN), Rapporteur  
Mme S. Arbab Chirani, Professeure des Universités, Ecole Nationale d'Ingénieurs de Brest, Rapporteur  
M. J.-J. Marigo, Professeur, Ecole Polytechnique, Examineur  
M. Y.J. He, Maître de Conférences (HDR), ENSTA-ParisTech, Co-directeur de thèse  
M. Z. Moumni, Professeur, ENSTA-ParisTech, Directeur de thèse





**THESE DE DOCTORAT**  
**DE**  
**L'UNIVERSITE PARIS-SACLAY**  
**PREPAREE A**  
**L'ECOLE NATIONALE SUPERIEURE DE TECHNIQUES AVANCEES**

ÉCOLE DOCTORALE N°579  
Sciences Mécaniques et Energétiques, Matériaux et Géosciences  
Spécialité de doctorat : Mécanique des Solides

Par

**Mme Lin ZHENG**

**Multi-scale Analysis of the Fatigue of Shape Memory Alloys**

**Thèse présentée et soutenue à Palaiseau, le 28 septembre 2016:**

**Composition du Jury :**

M. E. Charkaluk, Directeur de Recherche, Université Lille1 Sciences et Technologies, Président  
M. T. Ben Zineb, Professeur des Universités, Université de Lorraine (LEMTA – ESSTIN), Rapporteur  
Mme S. Arbab Chirani, Professeure des Universités, Ecole Nationale d'Ingénieurs de Brest, Rapporteur  
M. J.-J. Marigo, Professeur, Ecole Polytechnique, Examineur  
M. Y.J. He, Maître de Conférences (HDR), ENSTA-ParisTech, Co-directeur de thèse  
M. Z. Moumni, Professeur, ENSTA-ParisTech, Directeur de thèse

Dedicated to my beloved grandmother and mother.

© 2016

Lin ZHENG

All Rights Reserved

## Publications

- L. Zheng, Y.J. He, Z. Moumni, 2015. Frequency-dependent temperature and strain evolutions of NiTi wire during cyclic stress-controlled martensitic transformation, *Proceeding of PCM-CMM-2015*, Gdansk, Poland.
- L. Zheng, Y.J. He, Z. Moumni, 2016. Effects of Lüders-like bands on NiTi fatigue behaviors, *International Journal of Solids and Structures* 83 (2016) 28-44. doi:10.1016/j.ijsolstr.2015.12.021.
- L. Zheng, Y.J. He, Z. Moumni, 2016. Lüders-like band front motion and fatigue life of pseudoelastic polycrystalline NiTi shape memory alloy, *Scripta Materialia* 123 (2016) 46-50. doi:10.1016/j.scriptamat.2016.05.042.
- L. Zheng, Y.J. He, Z. Moumni, 2016. Investigation on fatigue behaviors of NiTi polycrystalline strips under stress-controlled tension via in-situ macro-band observation, under review.

## Acknowledgement

To write this acknowledgement is kind of to recall all the memories I had in this lab for more than three years. There were tough moments but also happy ones and I am grateful for arriving at the final line.

My two supervisors, Ziad Moumni and Yongjun He, this work would not have been possible without you. Ziad, thank you for creating the best working conditions (experimental materials, personal office, etc.) and meeting my other wants as possible as you can. Yongjun, you are the person who has watched me from the very beginning to the end, shared your own experiences (good and bad) in Hong Kong with no reservations, pointed out my faults of doing researches and then encouraged me by saying the merits in me and even listened to my complaints and tolerated my bad moods. So, thank you so much for devoting your precious time to me.

The two department directors, previously Antoine Chaigne and Habibou Maitournam since 2014, thank you for your efforts to advance my work.

I would also like to acknowledge all my committee members, Professors Eric Charkaluk, Jean-Jacques Marigo, Shabnam Arbab Chirani, and Tarak Ben Zineb, for your time and efforts devoted to evaluate my work.

It is a pleasure to thank all the faculty and staff — particularly, Anne-Lise Gloanec, Boumediene Nedjar, Kim Pham, thank you for your advice and concern; Alain Van Herpen and Lahcène Cherfa, thanks so much for your help with my experiments; Nicolas Baudet and Thierry Pichon, thank you for your support on the hardware and software. And all the fellow PhD students and postdocs, Agathe Forré, Ammar Ould Amer, Hao Yin, Jun Wang, Nicolas Thurieau, Oana-Zenaida Pascan, Qi Peng, Qianqiang Chen, Quantin Pierron, Selçuk Hazar, Shaobin Zhang, Xiaojun Gu, Xue Chen, Yahui Zhang, and Yinjun Jiang who is a visiting researcher from China, I have been fortunate to have shared the common moments in the lab with all of you. Also thank you to the two master students, Asma El Elmi and Ren Wei, who were with me on some experiments.

Last, but certainly not least, thank you to Shanshan Geng, who in the past four years has been with me through thick and thin and always believed in me. I am lucky and happy to be your friend.

## Table of Contents

<b>Table of Figures</b> .....	<b>vii</b>
<b>Chapter 1 Introduction</b> .....	<b>1</b>
<b>Chapter 2 Significant Effects of Lüders-like Bands on NiTi Fatigue Behaviors</b>	<b>10</b>
2.1 Introduction .....	10
2.2 Material and experimental details .....	11
2.3 Experimental observation .....	12
2.4 Discussion .....	25
<b>Chapter 3 Relation between Lüders-like Band-front Motion and Fatigue</b> .....	<b>31</b>
3.1 Introduction .....	31
3.2 Results and discussion .....	33
3.3 Summary .....	43
<b>Chapter 4 Band-Pattern Evolutions and Material Fatigue Criterion</b> .....	<b>45</b>
4.1 Introduction .....	45
4.2 Experimental results .....	46
4.3 Discussion .....	78
4.4 Conclusions .....	83
<b>Chapter 5 Conclusions and Prospects</b> .....	<b>85</b>
<b>Appendix: Experimental results of Specimens <i>B</i>, <i>C</i>, <i>E~H</i> of Chapter 2</b> .....	<b>90</b>
<b>References</b> .....	<b>102</b>

## Table of Figures

Fig. 1.1 Schematics of (a) shape memory effect and (b) pseudoelasticity.

Fig. 1.2 Multi-scale structures in NiTi polycrystals.

Fig. 1.3 Specifications of the NiTi dog-bone shaped specimen

Fig. 2.1 Cyclic waveform under stress control

Fig. 2.2 (a) Nominal stress-strain response curve with schematic patterns demonstrating the Lüders-like band evolution in a NiTi strip (Specimen *A*) in a strain-controlled tensile cycle (low strain rate  $\dot{\epsilon} = 8 \times 10^{-5} \text{ s}^{-1}$ , approximated as an isothermal case). The black and white regions of the schematic patterns respectively represent the Martensite (M) and Austenite (A) domains in the gauge section of the dog-bone specimen. (b) Optical observation on the Lüders-like bands. Values of the applied nominal strain  $\epsilon$  are accompanied by the symbol ↗ (↘) denoting the loading (unloading) process.

Fig. 2.3 All the 8 tested specimens have similar stress-strain curves of the isothermal strain-controlled test with strain rate  $\dot{\epsilon} = 8 \times 10^{-5} \text{ s}^{-1}$ .

Fig. 2.4 The stress-controlled tensile fatigue test on Specimen *A* with the maximum stress  $\sigma_{max} = 400 \text{ MPa}$  and the frequency  $f = 1 \text{ Hz}$  (Lüders-like band appeared *before* the “steady-state” cycles): (a) stress-strain curve evolution and schematic patterns, (b) evolutions of the cycle features: strain change  $\Delta\epsilon$  and mechanical energy-dissipation density  $D$  in one cycle, and (c) optical observation on the Lüders-like bands (the leftmost image shows the band nucleation in the isothermal test for reference).

Fig. 2.5 The stress-controlled tensile fatigue test on Specimen *D* with  $\sigma_{max} = 400 \text{ MPa}$  and  $f = 1 \text{ Hz}$  (Lüders-like band appeared *after* the “steady-state” cycles): (a) stress-strain curve evolution and schematic patterns, (b) evolutions of the cycle features  $\Delta\epsilon$  and  $D$ , and (c) optical observation on the Lüders-like bands (the leftmost image shows the band nucleation in the isothermal test for reference).

Fig. 2.6 Effects of the band formation (i.e., *with/without* the band nucleation/annihilation in “steady-state” cycles) on: (a) the fatigue life  $N_f$ , (b) the remaining fatigue life after the 1<sup>st</sup> band formation  $N_{remaining}$ .

Fig. 2.7 Effects of the band formation on the mechanical responses of the “steady stage”: (a) stress-strain curve of the 1<sup>st</sup> “steady-state” cycle, (b) nominal strain change  $\Delta\epsilon^S$ , and (c) mechanical energy-dissipation density  $D^S$ . (Legend of (b) and (c) is the same as in Fig. 2.6)

Fig. 2.8 (a) Comparisons between the band locations in the 1<sup>st</sup> “steady-state” cycles and the fatigue failure positions of Specimens *A*~*C*. (b) Comparisons between the locations of the 1<sup>st</sup> band nucleation and the fatigue failure positions of Specimens *D*~*H*.

Fig. 2.9 Comparisons between the location of the band formation in the reference isothermal test (left) and the fatigue failure position (right).

Fig. 2.10 Correlations between the fatigue life  $N_f$  and the structure responses in the “steady stage”: (a) change of structural nominal strain  $\Delta\epsilon^S$ , and (b) structural mechanical energy-dissipation density  $D^S$ . Correlations between the fatigue life  $N_f$  and the material responses in



the “steady stage”: (c) material’s strain change  $\Delta\varepsilon_{material}^S$ , and (d) material’s mechanical energy-dissipation density  $D_{material}^S$ .

Fig. 3.1 Cyclic waveform under strain control

Fig. 3.2 DIC measurement of the local strains for two typical cases (nominal strain amplitude  $\varepsilon_{ampl} = 1.0\%$  and  $0.5\%$ ): (a) fully-developed “active zone” and (b) partially-developed “active zone” whose size is comparable to the band-front thickness.

Fig. 3.3 (a) Nominal stress-strain curves of fatigue cycles (solid lines: the black, blue, red lines respectively represent the 1<sup>st</sup>, the 100<sup>th</sup>, and the final cycle before failure) of the specimens under a fixed nominal mean strain ( $\varepsilon_{mean} = 3.5\%$ ) with different nominal strain amplitudes ( $\varepsilon_{ampl} = 1.5\% \sim 0.25\%$ ) in comparison with their isothermal curves (dashed lines); (b) The corresponding Lüders-like band evolution (with “active zones” (shaded zones) in Cases I~V and without “active zones” in Case VI) and the final fractured specimens, where the red arrows indicate the fatigue-failure crack nucleation positions.

Fig. 3.4 Dependences of the fatigue life  $N_f$  on (a) the size of “active zones”  $l$  and (b) the local strain amplitude  $\varepsilon_{ampl}^{local}$  of the fatigue-failure material points.

Fig. 3.5 (a) The deformation domains and the final fractured specimens in the fatigue tests with a fixed nominal strain amplitude  $\varepsilon_{ampl} = 0.25\%$  (no “active zones”) and different nominal mean strains  $\varepsilon_{mean}$  (note: the specimen didn’t fail after 32922 cycles in Case I).

Fig. 3.6 (a) The dependence of the fatigue life  $N_f$  on  $\varepsilon_{mean}$ ; (b) The dependence of  $N_f$  on the local mean strain  $\varepsilon_{mean}^{local}$  (solid/open symbols represent the tests with/without fracture failure).

Fig. 3.7 (a) Global observation by optical camera on a specimen with small cyclic “active zones” (shaded zones) under the nominal strain amplitude of  $0.5\%$  and (b) Local observation by microscope on the evolution of a macro crack at the left end of the upper band front in (a).

Fig. 4.1 All the tested specimens have similar stress-strain curves in the isothermal strain-controlled tensile tests with global strain rate of  $8 \times 10^{-5} \text{ s}^{-1}$ .  $\sigma_0^{A \rightarrow M}$  ( $\sigma_0^{M \rightarrow A}$ ) denotes the transformation stress during the Austenite (A)  $\rightarrow$  Martensite (M) (M  $\rightarrow$  A) phase transformation and  $\sigma_0^N$  denotes the band-nucleation stress at room temperature  $T_0 \approx 21^\circ\text{C}$ .

Fig. 4.2 The stress-controlled cyclic tensile test on Specimen  $T$  with the maximum stress  $\sigma_{max} = 500 \text{ MPa}$  and the loading frequency  $f = 0.01 \text{ Hz}$  for 50 cycles: (a) the evolution of the stress-strain  $\sigma - \varepsilon$  curve, (b) evolutions of cycle-minimum nominal strain  $\varepsilon_{min}$ , cycle-maximum nominal strain  $\varepsilon_{max}$ , and nominal strain change  $\Delta\varepsilon = \varepsilon_{max} - \varepsilon_{min}$ , (c) the evolution of the mechanical energy-dissipation density  $D$ . (d) The optical observation on the Lüders-like band patterns of Specimen  $T$ . The values of the applied stress are accompanied by the symbol  $\nearrow$  ( $\searrow$ ) denoting the loading (unloading) process, zones highlighted by the black circles are the newly nucleated M bands during loading (patterns ‘a’~‘e’ and ‘i’~‘j’), the residual A bands at the end of loading (pattern ‘f’), or the residual M bands at the end of unloading (patterns ‘h’ and ‘l’). (e) The DIC full-field strain maps corresponding to the optical patterns in (d). (f) The local strain profiles derived from the DIC strain maps in (e) show the strain distribution along the centerline of the specimen’s gauge section.

Fig. 4.3 The stress-controlled tensile fatigue test on Specimen  $A_{500}^{0.01}$  with  $\sigma_{max} = 500 \text{ MPa}$  and  $f = 0.01 \text{ Hz}$ : (a) the evolution of  $\sigma - \varepsilon$  curve, (b) evolutions of  $\varepsilon_{min}$ ,  $\varepsilon_{max}$ , and  $\Delta\varepsilon = \varepsilon_{max} - \varepsilon_{min}$ , (c) the evolution of  $D$ , and (d) the optical observation on the Lüders-like band patterns.

Fig. 4.4 (a) Illustration of the shaded “active zones” with  $A \leftrightarrow M$  phase transformation and the unshaded “non-active zones” with “elastic” deformation of residual M bands in the 1<sup>st</sup> fatigue cycle of Specimen  $A_{500}^{0.01}$  compared with an image of the specimen after fracture failure; (b) The nominal stress-strain curve, 5 optical and DIC patterns, the associated strain profiles along the centerline of specimen’s gauge section and the calculated local strain amplitude  $\varepsilon_{ampl}^{local}$  in the 1<sup>st</sup> cycle.

Fig. 4.5 (a) Illustration of the shaded “active zones” with  $A \leftrightarrow M$  phase transformation and the unshaded “non-active zones” with “elastic” deformation of residual M bands in the 50<sup>th</sup> fatigue cycle of Specimen  $A_{500}^{0.01}$  compared with an image of the specimen after fracture failure; (b) The nominal stress-strain curve, 5 optical and DIC patterns, the associated strain profiles along the centerline of specimen’s gauge section and the calculated local strain amplitude  $\varepsilon_{ampl}^{local}$  in the 50<sup>th</sup> cycle.

Fig. 4.6 The stress-controlled tensile fatigue test on Specimen  $A_{500}^{0.1}$  with  $\sigma_{max} = 500$  MPa and  $f = 0.1$  Hz: (a) the evolution of  $\sigma - \varepsilon$  curve, (b) evolutions of  $\varepsilon_{min}$ ,  $\varepsilon_{max}$ , and  $\Delta\varepsilon = \varepsilon_{max} - \varepsilon_{min}$ , (c) the evolution of  $D$ , and (d) the optical observation on the Lüders-like band patterns.

Fig. 4.7 (a) Comparison of the “active zones” (shaded zones) and the “non-active zones” (residual A or residual M bands) in the 1<sup>st</sup> cycle, the 7<sup>th</sup> cycle, and the 50<sup>th</sup> fatigue cycle of Specimen  $A_{500}^{0.1}$ ; The nominal  $\sigma - \varepsilon$  curves, the typical strain profiles and the calculated local strain amplitudes  $\varepsilon_{ampl}^{local}$  in the 1<sup>st</sup> cycle (b), in the 7<sup>th</sup> cycle (c) and in the 50<sup>th</sup> cycle (d).

Fig. 4.8 The stress-controlled tensile fatigue test on Specimen  $A_{500}^1$  with  $\sigma_{max} = 500$  MPa and  $f = 1$  Hz: (a) the evolution of  $\sigma - \varepsilon$  curve, (b) evolutions of  $\varepsilon_{min}$ ,  $\varepsilon_{max}$ , and  $\Delta\varepsilon = \varepsilon_{max} - \varepsilon_{min}$ , (c) the evolution of  $D$ , and (d) the optical observation on the Lüders-like band patterns.

Fig. 4.9 (a) Comparison of the “active zones” (shaded zones) and the “non-active zones” (residual A bands) in the 10<sup>th</sup> cycle and the 50<sup>th</sup> fatigue cycle of Specimen  $A_{500}^1$ ; The nominal  $\sigma - \varepsilon$  curves, the typical strain profiles and the calculated local strain amplitudes  $\varepsilon_{ampl}^{local}$  in the 10<sup>th</sup> cycle (b) and in the 50<sup>th</sup> cycle (c).

Fig. 4.10 The stress-controlled tensile fatigue test on Specimen  $A_{400}^{0.01}$  with  $\sigma_{max} = 400$  MPa and  $f = 0.01$  Hz: (a) the evolution of  $\sigma - \varepsilon$  curve, (b) evolutions of  $\varepsilon_{min}$ ,  $\varepsilon_{max}$ , and  $\Delta\varepsilon = \varepsilon_{max} - \varepsilon_{min}$ , (c) the evolution of  $D$ , and (d) the DIC strain maps demonstrating the Lüders-like band patterns.

Fig. 4.11 The stress-controlled tensile fatigue test on Specimen  $A_{400}^{0.1}$  with  $\sigma_{max} = 400$  MPa and  $f = 0.1$  Hz: (a) the evolution of  $\sigma - \varepsilon$  curve, (b) evolutions of  $\varepsilon_{min}$ ,  $\varepsilon_{max}$ , and  $\Delta\varepsilon = \varepsilon_{max} - \varepsilon_{min}$ , (c) the evolution of  $D$ , and (d) the DIC strain maps demonstrating the Lüders-like band patterns.

Fig. 4.12 Significant effects of the Lüders-like band formation in the “steady-state” cycles on the specimen’s mechanical responses and the associated fatigue life: (a) Specimen  $A_{400}^1$  with Lüders-like bands in the “steady-state” cycles and (b) Specimen  $D_{400}^1$  without Lüders-like bands in the “steady-state” cycles.

Fig. 4.13 Comparison of the nominal  $\sigma - \varepsilon$  curves (left), the strain profiles and the calculated local strain amplitude  $\varepsilon_{ampl}^{local}$  (right) in the 50<sup>th</sup> cycles of (a) Specimen  $A_{400}^{0.01}$ , (b) Specimen  $A_{400}^{0.1}$ , and (c) Specimen  $A_{400}^1$ .

Fig. 4.14 Evolutions of  $\sigma - \varepsilon$  curve of the stress-controlled tensile fatigue tests on (a) Specimen  $A_{300}^{0.1}$  with  $\sigma_{max} = 300$  MPa and  $f = 0.1$  Hz and (b) Specimen  $A_{300}^1$  with  $\sigma_{max} = 300$  MPa and  $f = 1$  Hz.

Fig. 4.15 (a) Typical Lüders-like band patterns under different loading conditions (shaded “active zones” with cyclic A $\leftrightarrow$ M phase transformation and the unshaded “non-active zones” with cyclic “elastic” deformation of residual Martensite or residual Austenite) demonstrate the effects of the applied stress and frequency; the fatigue failure always occurred in one of the “active zones” indicated by the arrows; (b) The dependence of the fatigue life  $N_f$  on the local strain amplitude  $\varepsilon_{ampl}^{local}$  in the “steady stage”; (c) The dependence of  $N_f$  on the applied stress and frequency, where  $N_f$  basically decreases with increasing the stress level. (The dashed lines just guide the eyes.)

Fig. 4.16 The dependences of the fatigue life  $N_f$  on (a) the local residual strain  $\varepsilon_{local-res}^{N_f}$  and (b) the average accumulation rate of the local residual strain  $\overline{\varepsilon_{local-res}^{N_f}} = \varepsilon_{local-res}^{N_f} / N_f$ .

Fig. A1 The stress-controlled tensile fatigue test on Specimen  $B$  with  $\sigma_{max} = 400$  MPa and  $f = 1$  Hz (Lüders-like band appeared *before* the “steady-state” cycles): (a) stress-strain curve evolution and schematic patterns, (b) evolutions of the cycle features  $\Delta\varepsilon$  and  $D$ , and (c) optical observation on the Lüders-like bands.

Fig. A2 The stress-controlled tensile fatigue test on Specimen  $C$  with  $\sigma_{max} = 400$  MPa and  $f = 1$  Hz (Lüders-like band appeared *before* the “steady-state” cycles): (a) stress-strain curve evolution and schematic patterns, (b) evolutions of the cycle features  $\Delta\varepsilon$  and  $D$ , and (c) optical observation on the Lüders-like bands.

Fig. A3 The stress-controlled tensile fatigue test on Specimen  $E$  with  $\sigma_{max} = 400$  MPa and  $f = 1$  Hz (Lüders-like band appeared *after* the “steady-state” cycles): (a) stress-strain curve evolution and schematic patterns, (b) evolutions of the cycle features  $\Delta\varepsilon$  and  $D$ , and (c) optical observation on the Lüders-like bands.

Fig. A4 The stress-controlled tensile fatigue test on Specimen  $F$  with  $\sigma_{max} = 400$  MPa and  $f = 1$  Hz (Lüders-like band appeared *after* the “steady-state” cycles): (a) stress-strain curve evolution and schematic patterns, (b) evolutions of the cycle features  $\Delta\varepsilon$  and  $D$ , and (c) optical observation on the Lüders-like bands.

Fig. A5 The stress-controlled tensile fatigue test on Specimen  $G$  with  $\sigma_{max} = 400$  MPa and  $f = 1$  Hz (Lüders-like band appeared *after* the “steady-state” cycles): (a) stress-strain curve evolution and schematic patterns, (b) evolutions of the cycle features  $\Delta\varepsilon$  and  $D$ , and (c) optical observation on the Lüders-like bands.

Fig. A6 The stress-controlled tensile fatigue test on Specimen  $H$  with  $\sigma_{max} = 400$  MPa and  $f = 1$  Hz (Lüders-like band appeared *after* the “steady-state” cycles): (a) stress-strain curve evolution and schematic patterns, (b) evolutions of the cycle features  $\Delta\varepsilon$  and  $D$ , and (c) optical observation on the Lüders-like bands.

## 1. Introduction

Shape Memory Alloys (SMAs) are a group of metallic alloys that can “remember” the original shape when subjected to certain driving forces such as thermo-mechanical or magnetic variations. This unique feature called *shape memory effect* results from a solid-solid displacive (diffusionless) martensitic phase transformation between a phase called *Austenite* (a high-temperature and high-symmetry structure) and a phase called *Martensite* (a low-temperature and low-symmetry structure with several variants). The shape memory effect can be briefly described as follows (see the schematic in Fig. 1.1(a)). If the material is initially Austenite (“A” phase) (i.e., at a certain high temperature), upon cooling below a temperature  $M_s$  (*Martensite start temperature*), the material transforms to Martensite (“M” phase) with the nucleation and growth of M variants of different crystallographic orientations in order to minimize the deformation strain energy. This process (1) is called “*self-accommodation*” or “*twinning*” (because the M variants are internally twinned); macroscopically, there is no shape change since the material’s total volume remains the same. The transformation ends at a temperature  $M_f$  (*Martensite finish temperature*) where the material almost only contains the “*thermal/self-accommodated M*”. Now, at the low temperature, if a stress is applied, the material of different M variants deforms elastically before a certain stress is reached where one of the variants having a favorable orientation aligned with the stress grows, at the expense of the other less favorably oriented variants. So, at the end of the process (2) called “*Martensite reorientation*”, there is almost only the “*tensile/oriented M*” in the material with a large deformation/strain; the strain remains large after the stress is released since the Martensite is stable at this low temperature. Then if the material is heated above a temperature  $A_s$  (*Austenite start temperature*), the original A phase

nucleates and progressively “replaces” the M phase till a total recovery of the initial shape upon a temperature  $A_f$  (*Austenite finish temperature*). So, it is seen that the shape memory effect (including processes (1)(2)(3) or just (2)(3)) is a macroscopic effect of thermally induced crystallographic phase changes.

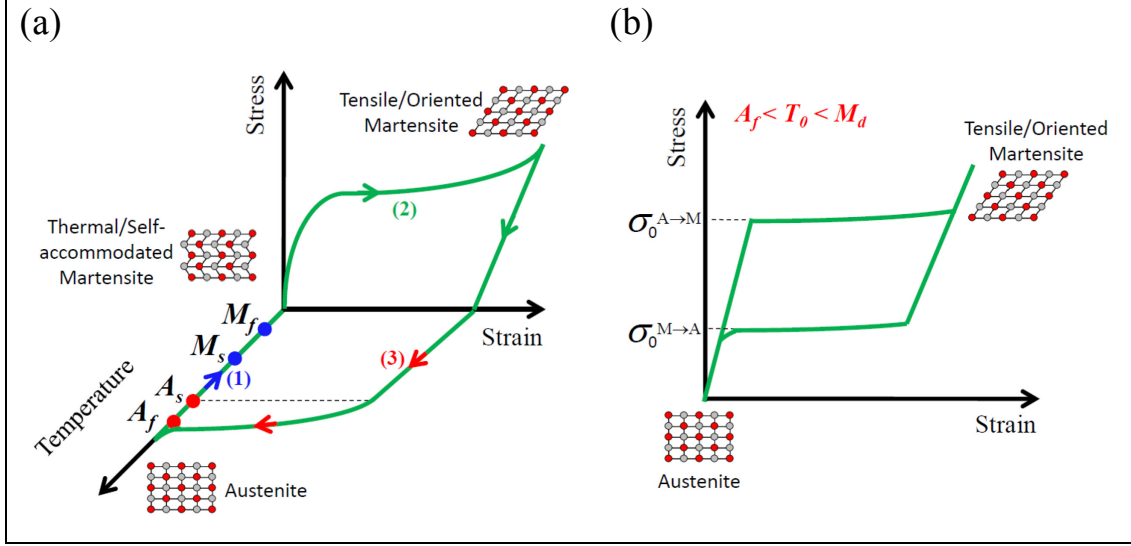


Fig. 1.1 Schematics of (a) shape memory effect and (b) pseudoelasticity.

There is another unique feature of SMAs also originating from the martensitic phase transformation, *pseudoelasticity* (or *superelasticity*), which presents the material’s ability to totally recover from a large “pseudo elastic” strain of up to ~10% induced by a mechanical load (compared with the elastic strain of only ~0.2% for normal metals) [1]. The pseudoelasticity only exists in a certain temperature range, namely, between the characteristic temperature  $A_f$  and the material’s deformation temperature  $M_d$  (above which there is only plastic deformation). As schematically shown in Fig. 1.1(b), at a constant temperature  $A_f < T_0 < M_d$ , the material of initial A phase is stable and then it elastically deforms upon a forced loading to a critical stress level ( $\sigma_0^{A \rightarrow M}$ ) where the A  $\rightarrow$  M phase transformation happens. The Martensite phase (tensile/oriented M) nucleates and then grows till a nearly total “replacement” of Austenite phase at the end of the forward transformation. Under a very slow loading

rate at the constant temperature, the transformation proceeds by forming a plateau-type stress-strain slope with a large transformation strain. Afterwards, upon the unloading to another critical stress level ( $\sigma_0^{M \rightarrow A}$ ), the reverse  $M \rightarrow A$  transformation starts during which the material returns to the original state (Austenite phase with almost zero residual strain). This  $A \leftrightarrow M$  phase transformation is macroscopically reversible but there could exist some irreversible activities at lower levels (i.e., meso-scale or/and micro-scale), for example, the friction or/and dislocation generation caused by the interface movement. As displayed by the stress-strain hysteresis loop in Fig. 1.1(b), the mechanical energy dissipation of the martensitic phase transformation in the loading-unloading cycle actually makes the material capable to dissipate/absorb energy thereby being used as dampers in various mechanical, civil, and aerospace engineering applications; on the other hand, this property could be detrimental to the material's fatigue resistance for the reasons of the irreversible activities mentioned above, when it should sustain a large number of cycles in some applications (e.g., medical stents).

Owning to the unique properties, SMAs have been increasingly demanded in applications from aerospace industry, mechanical and civil engineering, to the biomedical domain (a recent review article [2] can be referred to for an overview of the SMA applications and opportunities). Among all the commercialized SMAs, Nickel-Titanium (NiTi or Nitinol as the acronym for NiTi-Naval Ordnance Laboratory where the alloy's unique features were first discovered in the 1960s) is especially outstanding due to the superior shape memory effect and pseudoelasticity, the resistance to corrosion and biocompatibility, an unusual combination of strength and ductility [3]. However, as mentioned above, the material's fatigue is still a big concern, particularly when the failure of structures or components is unpredictable.

Many research efforts have been made to understand the material's fatigue behaviors and the physical mechanisms. According to Eggeler et al. (2004) [4], the fatigue of SMAs can be generally classified into two categories — functional fatigue and structural fatigue. The functional fatigue describes the cyclic degradation of the unique features of SMAs, such as the decrease of reversible (exploitable) strain, decrease of damping capacity (hysteresis loop), increase of residual/permanent deformation, etc.. It is considered [3] that the study of “functional fatigue” of SMAs has been started earlier by the work of Melton and Mercier (1979) [5], Miyazaki et al. (1986) [6], and Van Humbeeck (1991) [7]. The interest of research on the functional fatigue has then increased with many publications [4, 8-14, and among many others]; many of them have identified that the cyclic degradation of the mechanical responses stabilize after 100-150 cycles (i.e., reaching “steady state”), but from a microscopic point of view, it is argued that the microstructure degradation changes constantly till the fracture failure (i.e., structural fatigue) [3]. On the other hand, the structural fatigue includes the defect accumulation, crack initiation, crack propagation to a critical length, and final fracture [15]; the crack size at the transition from the initiation to propagation varies with the initial defects and thermo-mechanical histories of the material and also the geometry size of the specimen. The two methodologies used to study the fatigue of metals — total-life approaches and defect-tolerant approach [16], are also applied to the structural fatigue of SMAs. The total-life approach is to evaluate the total fatigue life (including crack initiation and propagation periods) based on the mechanical responses such as the mean level/amplitude of the applied stress/strain. By assuming that some micro-cracks preexist in a specimen/structure, the defect-tolerant approach is used to study the growth of a single macro-crack with the number of cycles till the fracture failure (Paris' law); in other words, this approach only considers the crack propagation

period. A majority of fatigue studies have been based on the total-life approaches [3]; moreover, it is identified that the crack initiation dominates the fatigue process thus a macro-crack growing fast before fatigue failure [5, 17-19]. In this thesis, it is focused on the total-life fatigue of NiTi; more details on the defect-tolerant fatigue of NiTi can be found in the review article [1].

As mentioned above, the total-life approach used in NiTi fatigue study attempts to predict the material's fatigue life by plotting the stress-life ( $S-N$ ) or strain-life ( $\varepsilon-N$ ) curve. The  $S-N$  curve is also referred to as Wöhler curve due to the work of A. Wöhler in the nineteenth century. The  $\varepsilon-N$  curve was first developed by Coffin (1954) and Manson (1954) thereby being known as Coffin-Manson relation/equation; the strain term used in the original Coffin-Manson equation for metallic materials is the plastic strain amplitude, while in many studies of NiTi SMAs it is more common to adopt the total strain amplitude as the strain term (many examples can be found in [1] and [3]). Moreover, a relation between the mechanical energy dissipation (stress-strain hysteresis loop) and the fatigue life has been established by some researchers [8, 20-22]. However, these stress-, strain-, and energy-based fatigue approaches usually adopt the structural nominal/global responses, which cannot well represent the material local behaviors of SMAs especially when the martensitic phase transformation proceeds in a heterogeneous mode forming shear bands (Martensite high-strain domains, see Fig. 1.2) due to the material's softening property [23]; for example, in a pseudoelastic NiTi polycrystalline strip (such as the one shown in Fig. 1.2) under uniaxial tension, the local strain of Martensite (M) macro-band is  $\sim 6.4\%$  while the local strain of Austenite (A) phase is only  $\sim 0.8\%$  [19]. The strain-induced shear bands mainly termed as Lüders-like bands (similar to the phenomena observed in mild steels by Lüders (1860)), were first observed by Miyazaki et al. (1981) [24] on



a NiTi wire. Shaw and Kyriakides (1995, 1997a, 1997b) [25-27] pioneered the experimental observation on the Lüders-like band patterns (strain and temperature distributions) on NiTi wires and strips under tension. This localized instability has also been observed in NiTi tubes under tension or bending [28-33].

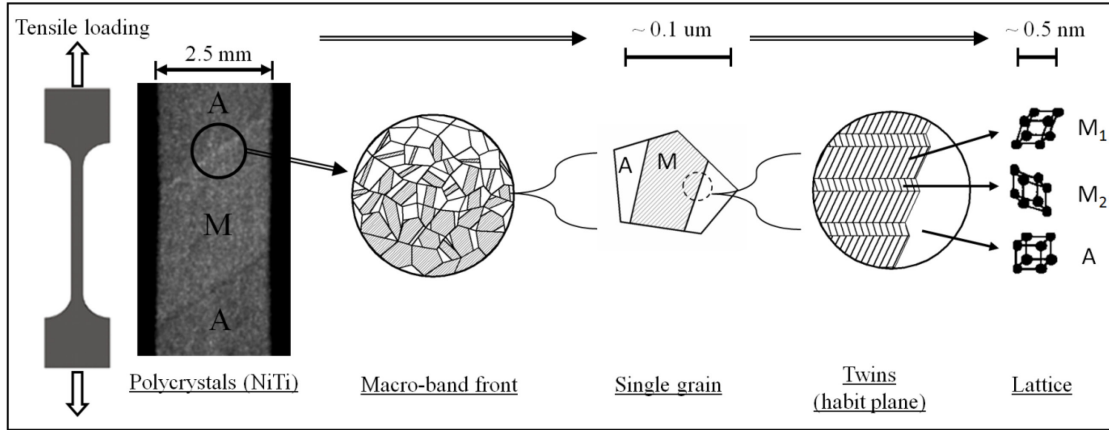


Fig. 1.2 Multi-scale structures in NiTi polycrystals. [19]

As seen in Fig. 1.2, a NiTi polycrystal is indeed a complex system containing many phase-transformable grains that also have patterns at lower levels (e.g., grain boundaries, A-M interfaces, Martensite twins). Moreover, it is verified that the phase transformation is not microscopically completed at the end of the pseudoelastic stress plateau (as schematically shown in Fig. 1.1(b)): Brinson et al. (2004) [34] first observed by microscope that the M macro-bands are regions of more intense transformation, but regions outside the bands are not martensite-free, and even at the end of the forward transformation the specimen is at most 70% martensitic. So, from a material and microscopic point of view, the fatigue analysis of NiTi should adopt the local material responses (e.g., local strain, local temperature) to better understand the physical mechanisms. Many experimental efforts have been made to reveal the microstructure mechanisms behind the macroscopic features of NiTi SMAs with direct observations through optical microscopy [6, 34, 35], X-ray diffraction [36-40], SEM [4, 9, 37, 41, 42], and TEM [43-47], or to interpret the macroscopic behaviors with

microstructure hypotheses [4, 8, 9, 48-51, and among many others]. It is believed that the microstructure damage/degradation in the pseudoelastic NiTi SMAs can be caused by the cyclic plastic deformation (dislocation generation/motion), the cyclic phase transformation, and their interaction [4, 6, 45, 52, 53]. Particularly, the residual deformation (strain) and its accumulation with the number of cycles are usually taken as indicators on the material damage [5, 54-56]. Two physical mechanisms were observed to cause the residual strain — the dislocation generation/motion [39, 43, 45, 47] and the “locked-in” residual Martensite stabilized by dislocations [4, 6, 8, 34, 41, 46, 48-51, 57].

So, it is seen that many research efforts have been made on the fatigue study of NiTi SMAs and the contributions to understand the localized behaviors are also rich, but there is still no experimental study combining these two issues — to study the material’s fatigue process by tracing the Lüders-like band behaviors at a macro or meso scale. To bridge this gap, it is motivated to study the fatigue of SMAs with the in-situ observation of Lüders-like band evolution, to answer several questions such as: can the band-nucleation position be taken as a specimen’s weakest zone (potential failure position)? Does the weakest zone change during the cyclic loadings? Does there exist stabilization of Lüders-like band patterns, in comparing with the stabilization of macroscopic mechanical responses? ... To sum up, this thesis aims at finding the relation between the fatigue damage accumulation and the Lüders-like band evolution.

To this end, systematic pull-pull fatigue experiments on pseudoelastic NiTi polycrystalline strips (dog-bone shaped specimens, see Fig. 1.3) where the material is under simple uniaxial tension are performed with in-situ optical observation on the band patterns. Here, the selection of the material of NiTi, specimen shape of dog-bone,

and loading mode of pull-pull tension is made to simplify the in-situ observation of Lüders-like bands so that the material intrinsic behaviors can be well revealed. Although the material's metallurgical aspects (e.g., chemical composition, grain size, presence of inclusions, thermal treatment, etc.) have effects on its fatigue, they are out of the scope of this thesis and can be the future work. The outline of this work is described as follows.

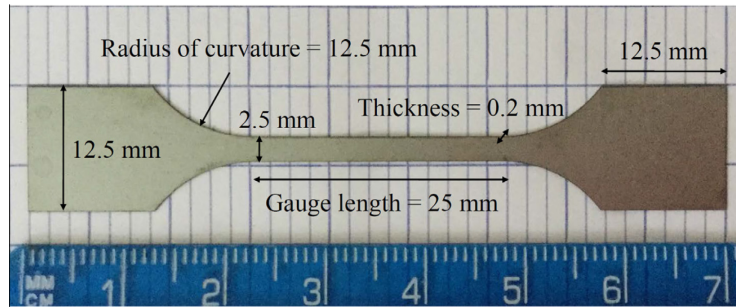


Fig. 1.3 Specifications of the NiTi dog-bone shaped specimen

Chapter 2 investigates the effects of Lüders-like bands on the NiTi fatigue behaviors by the synchronized measurement of the cyclic stress-strain responses and optical observation on the cyclic band nucleation/annihilation in the stress-controlled tensile fatigue tests. Under a critical loading condition with the maximum applied stress close to the isothermal band-nucleation stress and a high frequency, the Lüders-like bands do or do not nucleate in an individual specimen due to the initial defects, leading to a totally different fatigue process. As the band-nucleation site could indicate a specimen's weak zone, the fatigue failure position is checked in comparison with the specimen's initial weakest zone (where the first Lüders-like band nucleates); it's surprising to find that the fatigue failure does not always occur in the initial weakest zone.

Then in Chapter 3, among the specimens with Lüders-like bands, the effects of the band-front motion is further identified in the strain-controlled tensile fatigue tests with the in-situ optical observation focused on the band front; regions cyclically swept

by the moving fronts are then identified as “**active zone**” where the fatigue failure occurs. And the optical images are processed by the method of Digital Image Correlation (DIC) to quantify the local deformation history of the fatigue-failure material point. Interestingly, it is found that when there are no “active zones” (motionless band fronts), the fatigue failure occurs away from the immobile band fronts that are usually considered as weak zones. It is found a quantitative relation between the local strain amplitude and the fatigue life.

In Chapter 4, through systematic stress-controlled fatigue tests, it is found that the applied stress level and frequency change the Lüders-like band formation and evolution thus affecting the material’s fatigue behaviors significantly. The band evolution divides a specimen into “non-active zones” (with the macroscopically elastic deformation of Austenite or/and Martensite) and “active zones” (with the cyclic phase transformation) where fatigue failure occurs. Based on the local strain measurement by DIC, the local residual-strain (damage) accumulation rate is determined and found to have a good correlation with the material’s fatigue life for all the acquired data of different stress levels and loading frequencies.

Chapter 5 summarizes the findings of this doctoral work: general conclusions from this work and some directions for the future work are discussed.

## **2. Significant Effects of Lüders-like Bands on NiTi Fatigue Behaviors**

### **2.1 Introduction**

Lüders-like band in NiTi polycrystals is a complicated phenomenon including multi-scale structures as already illustrated in Fig. 1.2 where a Lüders-like band is formed in a NiTi polycrystalline strip under uniaxial tension. The grains in the high-strain domain (Lüders-like band) almost fully transform to Martensite (M) phase while most of the grains in the low-strain domain remain in Austenite (A) phase and the interface consists of partially transformed grains [34]. The formation of the Lüders-like band is in fact a result of the thermo-mechanical interactions in the lattices and grains. In the literature, the macroscopic observation on Lüders-like band in various NiTi structures (wire/strip/tube) has been reported by some research groups [24-33, 58-62], and several macro-models have been proposed to capture the general features of the macro-band formation [27, 63-69]. At the micro-scale level, many research results have been reported since the discovery of the shape memory effect [70, 71, and among many others]; recently, the interaction between events of the martensitic phase transformation (such as the A-M interface motion, twinning, Martensite reorientation, and heterogeneous martensitic nucleation) and the dislocations/defects was studied [46, 72, 73] which helps to better understand the effects of the phase transformation on the material microstructure degradation and fatigue behaviors.

As seen in Chapter 1, the fatigue behaviors of SMAs have attracted many attentions due to the materials' increasing applications, but there are no experiments that directly show the effects of the Lüders-like band on the material's fatigue behaviors, despite some conjectures that the Austenite-Martensite interfaces are potential sites for the fatigue crack initiation thereby governing the fatigue life [51, 74,

75]. In this chapter, through a comparison on the fatigue behaviors between the specimens with cyclic Lüders-like band formation (cyclic  $A \leftrightarrow M$  phase transformation) and the specimens without Lüders-like bands (cyclic macroscopically elastic deformation of Austenite phase), it is found that the cyclic band formation causes faster microstructure degradation, leading to shorter fatigue lives.

## 2.2 Material and experimental details

The material used in this chapter was a commercial NiTi polycrystalline sheet with a composition of 55.89wt.% Ni with an Austenite finish temperature  $A_f$  around 10°C (Johnson Matthey Inc. USA). Dog-bone shaped specimens were extracted by wire-EDM (Electro-Discharge Machining) from the fresh NiTi sheets where the long axis of the specimen is along the rolling direction. The specimen surfaces are “pickled” as received from the supplier which is proper for the optical observation. The experiments were performed at room temperature  $T_0$  ( $\approx 21^\circ\text{C}$ ), higher than the material’s  $A_f$ . So, the material shows pseudoelastic behaviors in the mechanical tests by a dynamic testing machine (Instron ElectroPuls E3000) — the strain-controlled isothermal quasi-static tests (Section 2.3.1) and the stress-controlled high-frequency fatigue tests (Section 2.3.2).

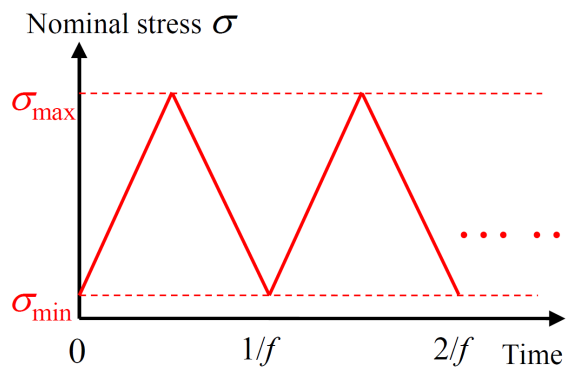


Fig. 2.1 Cyclic waveform under stress control

The tensile fatigue tests were conducted in the stress-controlled mode with the maximum stress  $\sigma_{max}$  of 400 MPa at a loading frequency  $f$  of 1 Hz, and the minimum stress  $\sigma_{min}$  was set to 20 MPa to avoid the compression upon unloading (see the cyclic waveform under stress control in Fig. 2.1). An optical observation system, including a 2048×1088 pixels CMOS fast camera (Basler acA2000-340km), a Nikon lens (Micro-Nikkor Auto 55mm f/3.5), a frame grabber (Matrox Radiant eCL), and software StreamPix 6 (NorPix Inc.), was constructed to in-situ observe the surface morphology (deformation patterns) of the entire gauge section with a recording rate of 50 frames/s. The global nominal strain is determined as the machine's crosshead displacement ( $\delta$ ) divided by the specimen's gauge length ( $L$ ), while the local strain (e.g., the strain inside the Lüders-like band) can be determined by the optical images. The synchronized optical observation on Lüders-like band-pattern evolution and the mechanical stress-strain response curve are used to investigate the material's fatigue behaviors.

## 2.3 Experimental observation

### 2.3.1 Band formation in an isothermal loading-unloading cycle

A slow strain-controlled tensile loading-unloading cycle (under the global nominal strain rate of  $8 \times 10^{-5} \text{ s}^{-1}$  with the maximum nominal strain of 8%, approximated as an isothermal case) was performed on each as-received NiTi dog-bone specimen prior to the stress-controlled fatigue test. Usually, under the low strain rate, the specimen's temperature varies slightly and there is only one band nucleating during the overall martensitic phase transformation [25, 26, 60]. As shown in Fig. 2.2, the specimen deforms homogeneously without Lüders-like bands (macroscopic Martensite domains) until the applied nominal strain  $\varepsilon$  reaches 1.64% where a macro-

band appears (see the schematic pattern ‘b’ in Fig. 2.2(a) and the optical pattern ‘b’ in Fig. 2.2(b)). With the increase of the nominal strain, the macro-band grows with the band-front propagation (the arrows in the optical images in Fig. 2.2(b) show the propagation directions of the band fronts) and occupies the whole gauge section at the end of the loading (pattern ‘f’). When the nominal strain  $\varepsilon$  reduces to 5.46% (the stress decreases to the lower stress plateau) during the unloading, the macro-band shrinks with the propagation of the two fronts (patterns ‘g’~‘i’). Finally the entire specimen returns to the initial state (Austenite phase). It is noted that the strain inside the Lüders-like band (strain of M domain  $\varepsilon_M$ ) and the strain outside the band (strain of A domain  $\varepsilon_A$ ) are not equal to the nominal (global) strain when the two phases coexist, e.g., pattern ‘d’ in Fig. 2.2(b) where  $\varepsilon_M = 6.4\% \pm 0.1\%$  and  $\varepsilon_A = 0.8\% \pm 0.1\%$  measured by the optical images.

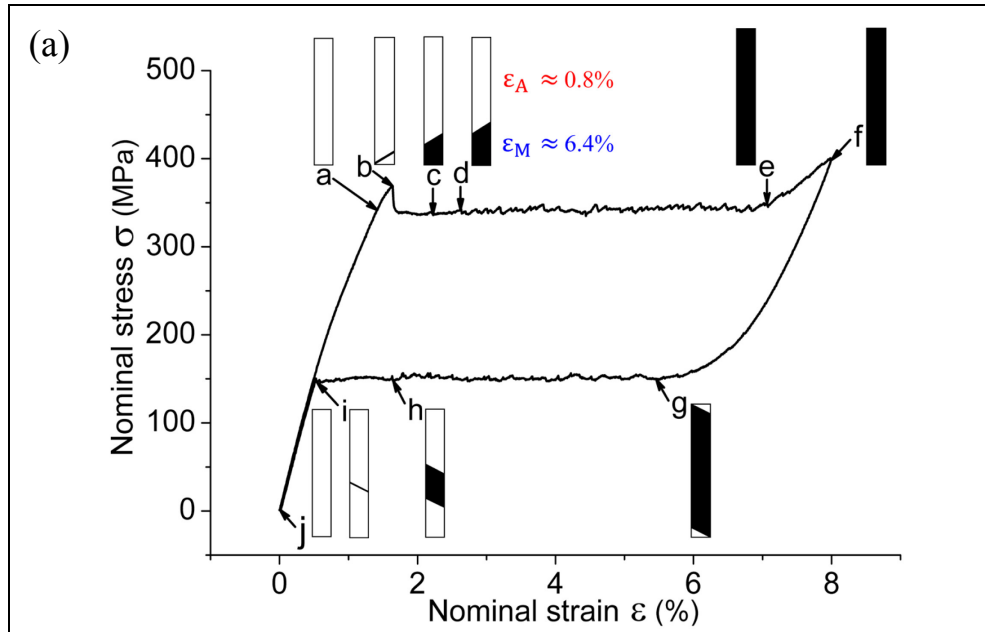


Fig. 2.2 (a) Nominal stress-strain response curve with schematic patterns demonstrating the Lüders-like band evolution in a NiTi strip (Specimen *A*) in a strain-controlled tensile cycle (low strain rate  $\dot{\varepsilon} = 8 \times 10^{-5} \text{ s}^{-1}$ , approximated as an isothermal case). The black and white regions of the schematic patterns respectively represent the Martensite (M) and Austenite (A) domains in the gauge section of the dog-bone specimen.



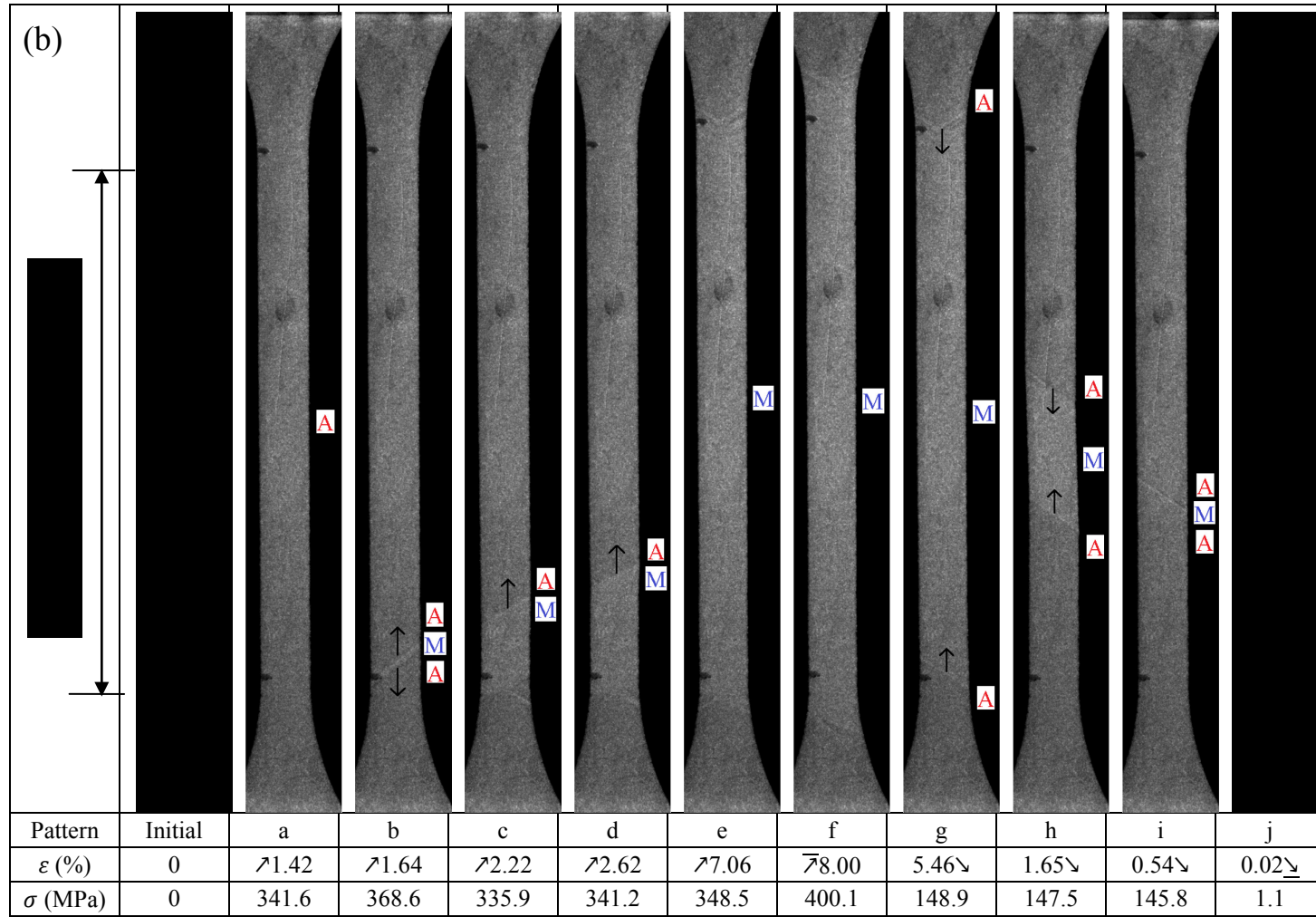


Fig. 2.2 (b) Optical observation on the Lüders-band patterns. Values of the applied nominal strain  $\epsilon$  are accompanied by the symbol  $\nearrow$  ( $\searrow$ ) denoting the loading (unloading) process.

All the 8 specimens used in the fatigue tests of this chapter are from the same batch of NiTi sheets and they have similar isothermal stress-strain responses as shown in Fig. 2.3, where the A→M (M→A) phase transformation plateau stress  $\sigma_0^{A \rightarrow M}$  ( $\sigma_0^{M \rightarrow A}$ ) is around 352.7 MPa (153.2 MPa), and the band-nucleation stress (the peak value before the stress drops to the upper plateau stress)  $\sigma_0^N$  varies from 368.6 MPa to 387.8 MPa. In the following stress-controlled fatigue tests (at frequency  $f = 1$  Hz), the maximum applied stress is 400 MPa, slightly higher than the values of  $\sigma_0^N$ . Due to the small variation of the mechanical properties in the individual specimens, the process of the band formation in the high-frequency fatigue test ( $f = 1$  Hz) varies among the specimens as reported in the following section.

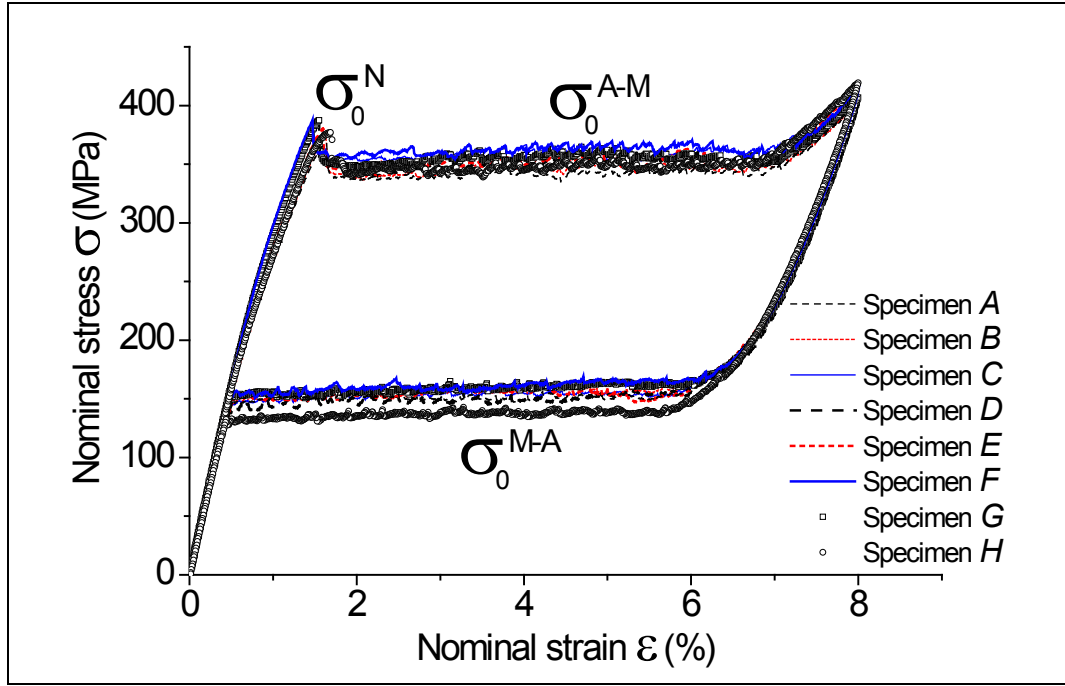


Fig. 2.3 All the 8 tested specimens have similar stress-strain curves of the isothermal strain-controlled test with strain rate  $\dot{\epsilon} = 8 \times 10^{-5} \text{ s}^{-1}$ .

### 2.3.2 Mechanical responses and band formation in stress-controlled fatigue tests

Figure 2.4 shows the results of the fatigue test on Specimen A. The stress-strain curves and the schematic of the typical patterns about the band formation are shown in Fig. 2.4(a) while the evolutions of the cycle features (change of the nominal strain in

one cycle  $\Delta\varepsilon$  and the mechanical energy-dissipation density  $D$  (stress-strain hysteresis-loop area)) are shown in Fig. 2.4(b). The optical observation on the macro-band formation is shown in Fig. 2.4(c). Due to the limitation of the testing machine at high frequencies, the maximum applied stress in the 1<sup>st</sup> cycle didn't reach the given stress level of 400 MPa until the 26<sup>th</sup> cycle. The 1<sup>st</sup> nucleation of a Lüders-like band was in the 20<sup>th</sup> cycle at the same location as in the isothermal case (see the pattern 'b' and the reference pattern in Fig. 2.4(c)), i.e., the specimen deformed homogeneously in the first 19 cycles where  $\Delta\varepsilon$  and  $D$  gradually increased with increasing the cycle number  $n$  as shown in Fig. 2.4(b). Subsequently, in the 49<sup>th</sup> cycle, a 2<sup>nd</sup> band nucleated at another location of the gauge section (see the pattern 'd'). For both the 1<sup>st</sup> and 2<sup>nd</sup> band formation, there was a jump in the cycle features ( $\Delta\varepsilon$  and  $D$ ). After about 60 cycles (transient stage which contains the cycles from the beginning of the fatigue test to the stabilization of cycle features), the "steady stage" (with "**steady-state**"<sup>1</sup> cycles) was reached with almost constant  $\Delta\varepsilon$  and  $D$ . In the 178<sup>th</sup> cycle, a crack was observed which led to the fracture failure: the dominant crack formed in the Lüders-like band as shown in the patterns 'e'~'g' and the associated magnified views in Fig. 2.4(c). The energy-dissipation density  $D$  increased a little in the last 5 cycles before failure as highlighted in Fig. 2.4(b).

---

<sup>1</sup> Properly speaking, steady-state cycles don't exist, because the material's microstructure changes all along the fatigue process and in some cases (reported in Chapter 4) even the nominal cycle-responses vary constantly till the fatigue failure, so the term of "steady-state" is always in the quotation marks in this thesis.

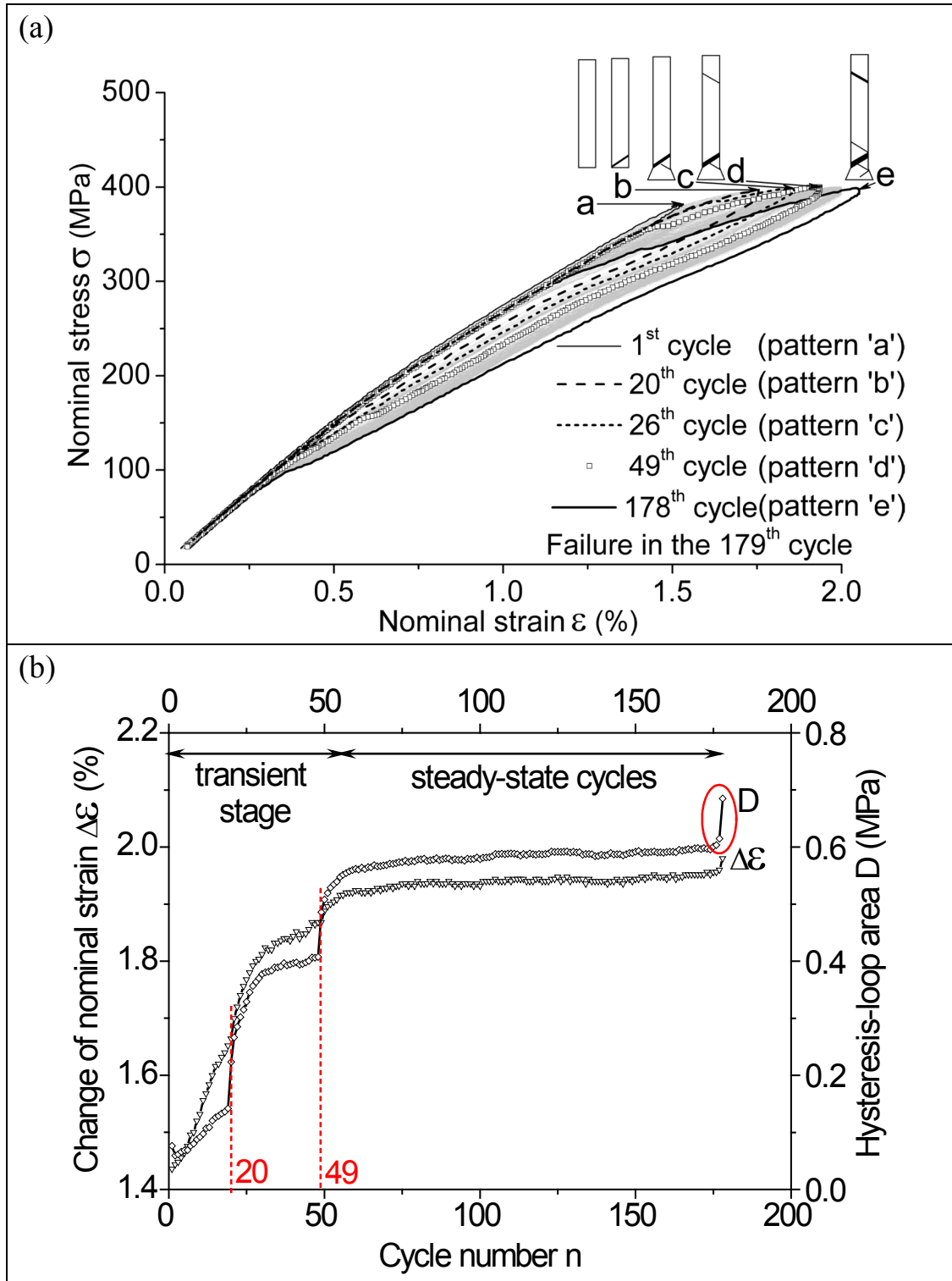


Fig. 2.4 The stress-controlled tensile fatigue test on Specimen *A* with the maximum stress  $\sigma_{max} = 400$  MPa and the frequency  $f = 1$  Hz (Lüders-like band appeared *before* the “steady-state” cycles): (a) stress-strain curve evolution and schematic patterns, (b) evolutions of the cycle features: strain change  $\Delta\epsilon$  and mechanical energy-dissipation density  $D$  in one cycle, and (c) optical observation on the Lüders-like band patterns (the leftmost image shows the band nucleation in the isothermal test for reference).

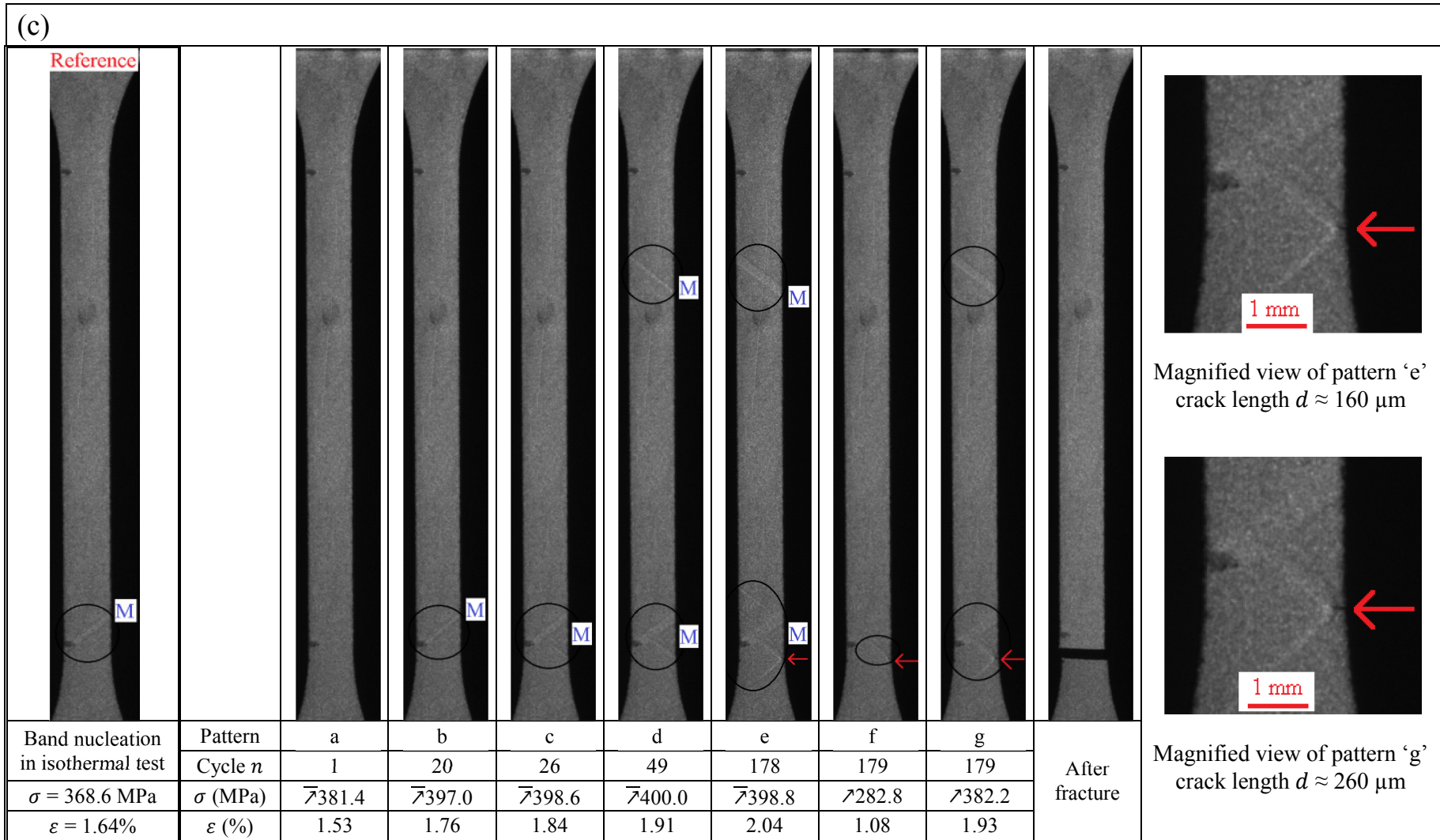


Fig. 2.4 *Continued*. (The arrows indicate the crack nucleation position.)

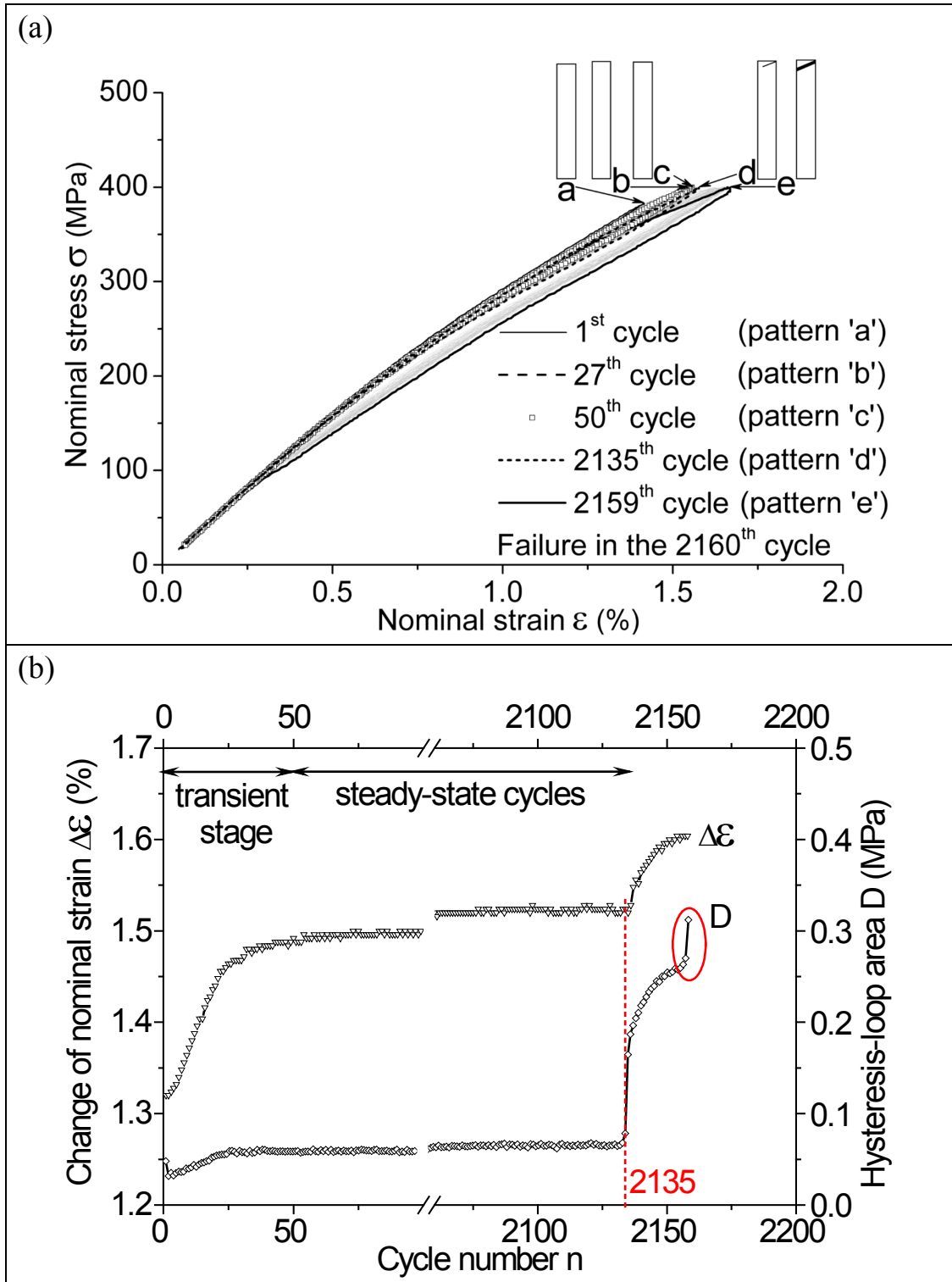


Fig. 2.5 The stress-controlled tensile fatigue test on Specimen  $D$  with  $\sigma_{max} = 400$  MPa and  $f = 1$  Hz (Lüders-like band appeared after the “steady-state” cycles): (a) stress-strain curve evolution and schematic patterns, (b) evolutions of the cycle features  $\Delta\epsilon$  and  $D$ , and (c) optical observation on the Lüders-like band pattern (the leftmost image shows the band nucleation in the isothermal test for reference).



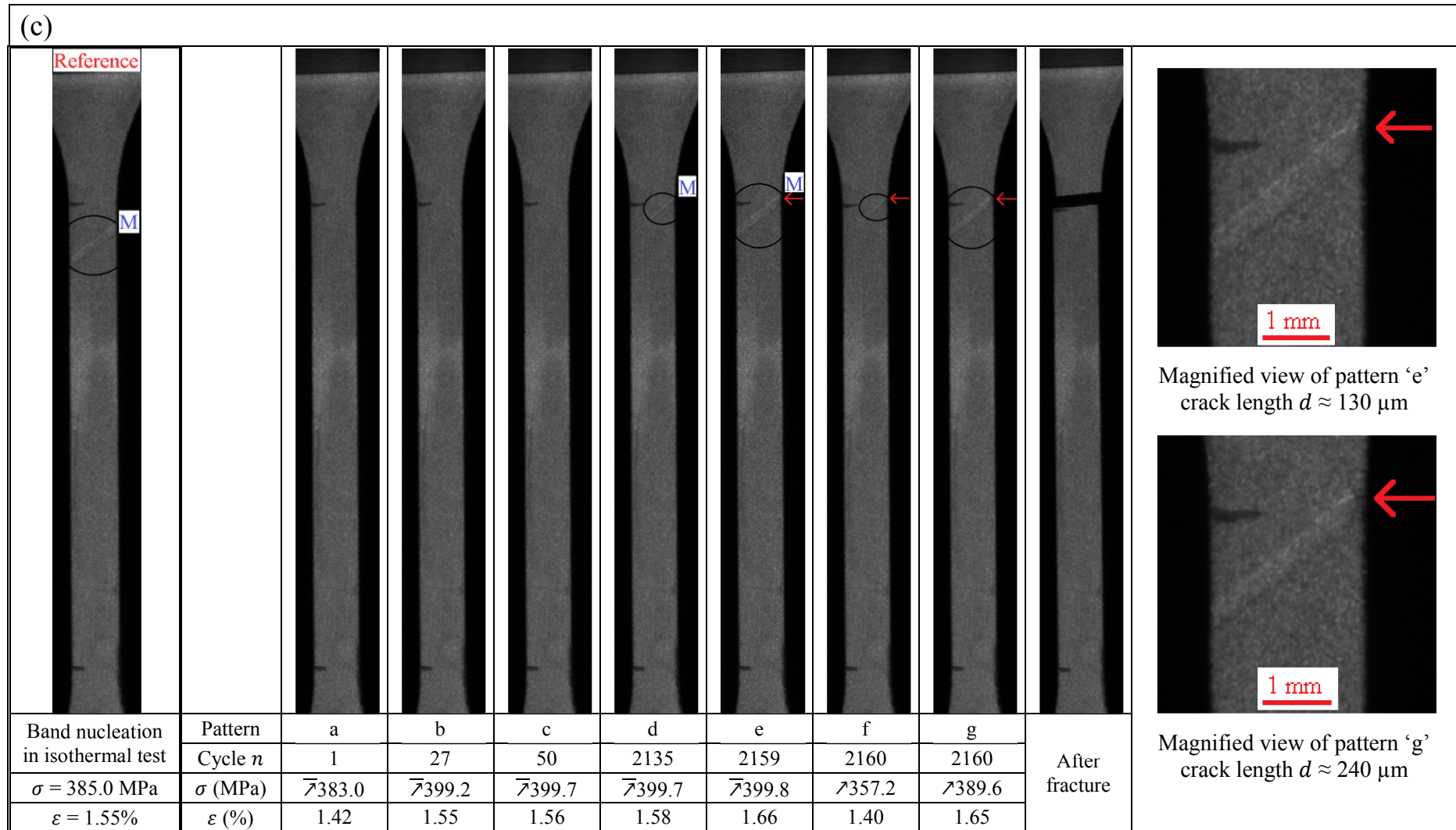


Fig. 2.5 Continued.

While Specimen *A* had cyclic band nucleation and growth during loading and band shrinkage and annihilation during unloading for the “steady-state” fatigue cycles, some of the 8 tested specimens had no bands in their “steady-state” fatigue cycles, such as Specimen *D* shown in Fig. 2.5. After the transient stage of 50-cycle homogeneous deformation (patterns ‘a’~‘c’ in Fig. 2.5(c)), the “steady-state” cycles were attained, in which ( $n = 50$ -2135) the cycle features  $\Delta\varepsilon$  and  $D$  changed little (see Fig. 2.5(b)) and the deformation was uniform without Lüders-like bands. One band first formed in the 2135<sup>th</sup> cycle (see the pattern ‘d’ in Fig. 2.5(c)); accompanying the band formation,  $\Delta\varepsilon$  and  $D$  had a jump (see Fig. 2.5(b)). With increasing the cycle number ( $n = 2135$ -2159), this Lüders-like band grew quickly (in comparing patterns ‘d’ and ‘e’ both at the loading end) and the values of  $\Delta\varepsilon$  and  $D$  largely increased. Finally a macro crack was observed in the band (as shown in the patterns ‘e’~‘g’ and the magnified views in Fig. 2.5(c)), leading to the fracture failure in the 2160<sup>th</sup> cycle.

It is noted that the fatigue life ( $N_f$ , defined as the cycles from the beginning of the fatigue test to the fracture failure) of Specimen *D* ( $N_f^D = 2160$ ) without bands in the “steady-state” cycles is much longer than that of Specimen *A* ( $N_f^A = 179$ ) with the cyclic band nucleation/annihilation. The detailed experimental results of the other 6 specimens are not presented here (see Appendix). The fatigue lives of all the 8 tested specimens are summarized in Fig. 2.6(a), which indicates that the fatigue life  $N_f$  of Specimens *A*~*C* with the cyclic band nucleation/annihilation in the “steady-state” cycles is much shorter than that of Specimens *D*~*H* without bands in the “steady-state” cycles. That means the Lüders-like band formation/evolution has significant effects on the material’s fatigue behaviors. Specifically for Specimen *G* and Specimen *H*, their fatigue lives are denoted as  $N_f^G > 4651$  and  $N_f^H > 4387$  as shown in the legend of Fig. 2.6, because the crack nucleated outside the gauge section, leading to failure in the



4651<sup>st</sup> cycle and the 4387<sup>th</sup> cycle, respectively. In other words, with only the homogeneous deformation in the gauge section, these two specimens should have longer fatigue lives. In Fig. 2.6(b), the remaining fatigue life after the 1<sup>st</sup> band formation  $N_{remaining} (= N_f - N_{band-nucleation})$  is plotted. In comparison between Figs. 2.6(a) and 2.6(b), it is indicated that, for Specimens *A*~*C* with Lüders-like band formation/evolution in the “steady-state” cycles, most of the fatigue life was spent with the inhomogeneous deformation, while for Specimens *D*~*H* without bands, the localized deformation only took place for a limited number of cycles ( $N_{remaining} \leq 25$  for Specimens *D*~*H*) before the fracture failure. It is interesting to note that, although the fatigue lives of Specimens *D*~*F* are quite different ( $N_f^D = 2160$ ,  $N_f^E = 768$ , and  $N_f^F = 1208$ ), their  $N_{remaining}$  are almost the same ( $N_{remaining}^D = 24$ ,  $N_{remaining}^E = 25$ , and  $N_{remaining}^F = 24$ ).

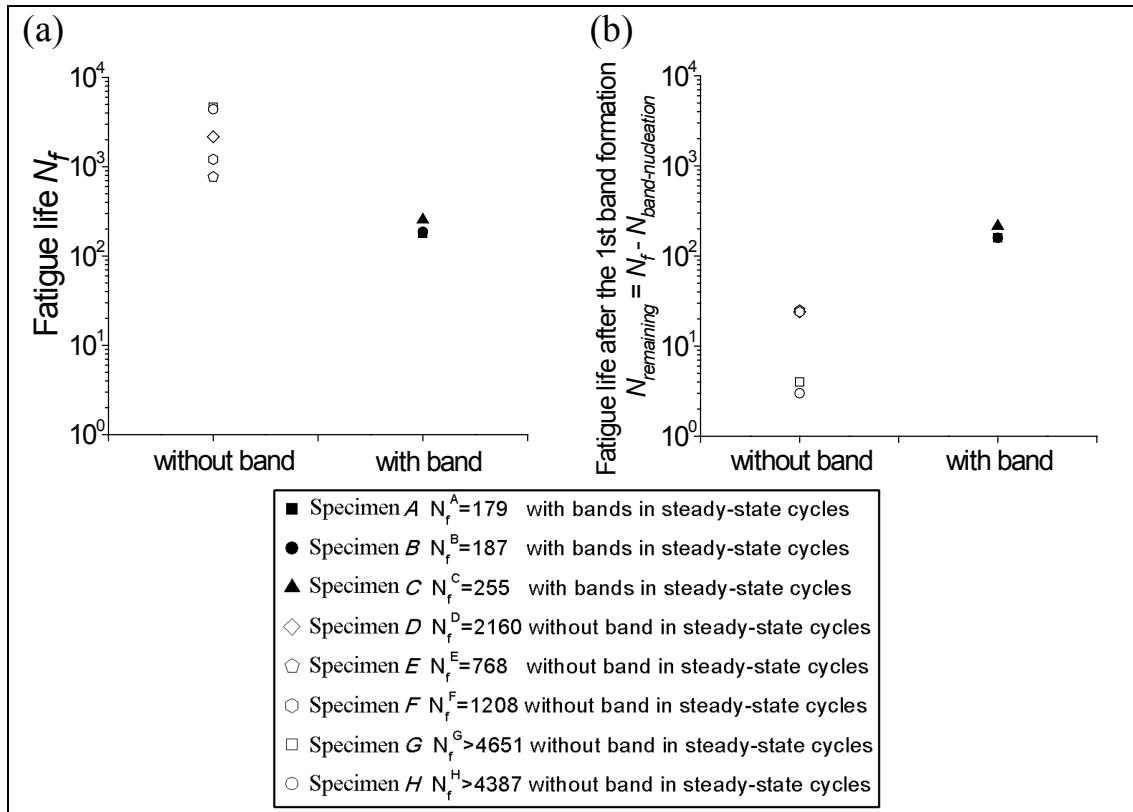


Fig. 2.6 Effects of the band formation (i.e., **with/without** the band nucleation/annihilation in “steady-state” cycles) on: (a) the fatigue life  $N_f$ , (b) the remaining fatigue life after the 1<sup>st</sup> band formation  $N_{remaining}$ .

The features of the “steady-state” cycles are normally used for understanding/prediction on the material’s fatigue behaviors/failure. Fig. 2.7(a) summarizes the stress-strain ( $\sigma - \varepsilon$ ) curves of the 1<sup>st</sup> “steady-state” cycle for all the specimens (it took around 50 cycles to reach the “steady stage” for all the specimens). Based on the “steady-state”  $\sigma - \varepsilon$  curves, the “steady-state” nominal strain change  $\Delta\varepsilon^s$  and the “steady-state” mechanical energy-dissipation density  $D^s$  are calculated and summarized in Figs. 2.7(b) and 2.7(c), which show the effects of the Lüders-like bands on the mechanical responses. It is indicated that, compared with the homogeneous deformation in Specimens *D~H*, the cyclic band nucleation/annihilation in the “steady-state” cycles of Specimens *A~C* leads to more energy dissipation and larger nominal strain change for most of the cases.

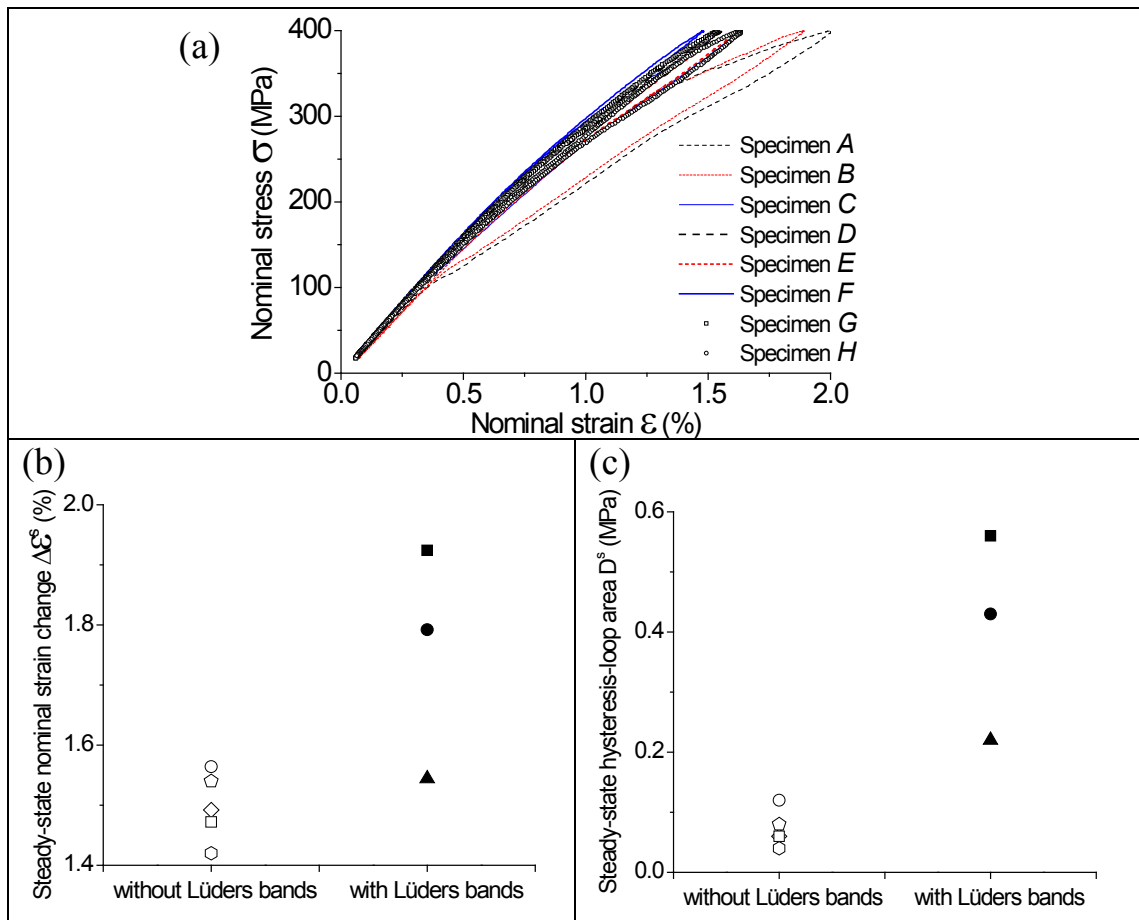


Fig. 2.7 Effects of the band formation on the mechanical responses of the “steady stage”: (a) stress-strain curve of the 1<sup>st</sup> “steady-state” cycle, (b) nominal strain change  $\Delta\varepsilon^s$ , and (c) mechanical energy-dissipation density  $D^s$ . (Legend of (b) and (c) is the same as in Fig. 2.6)

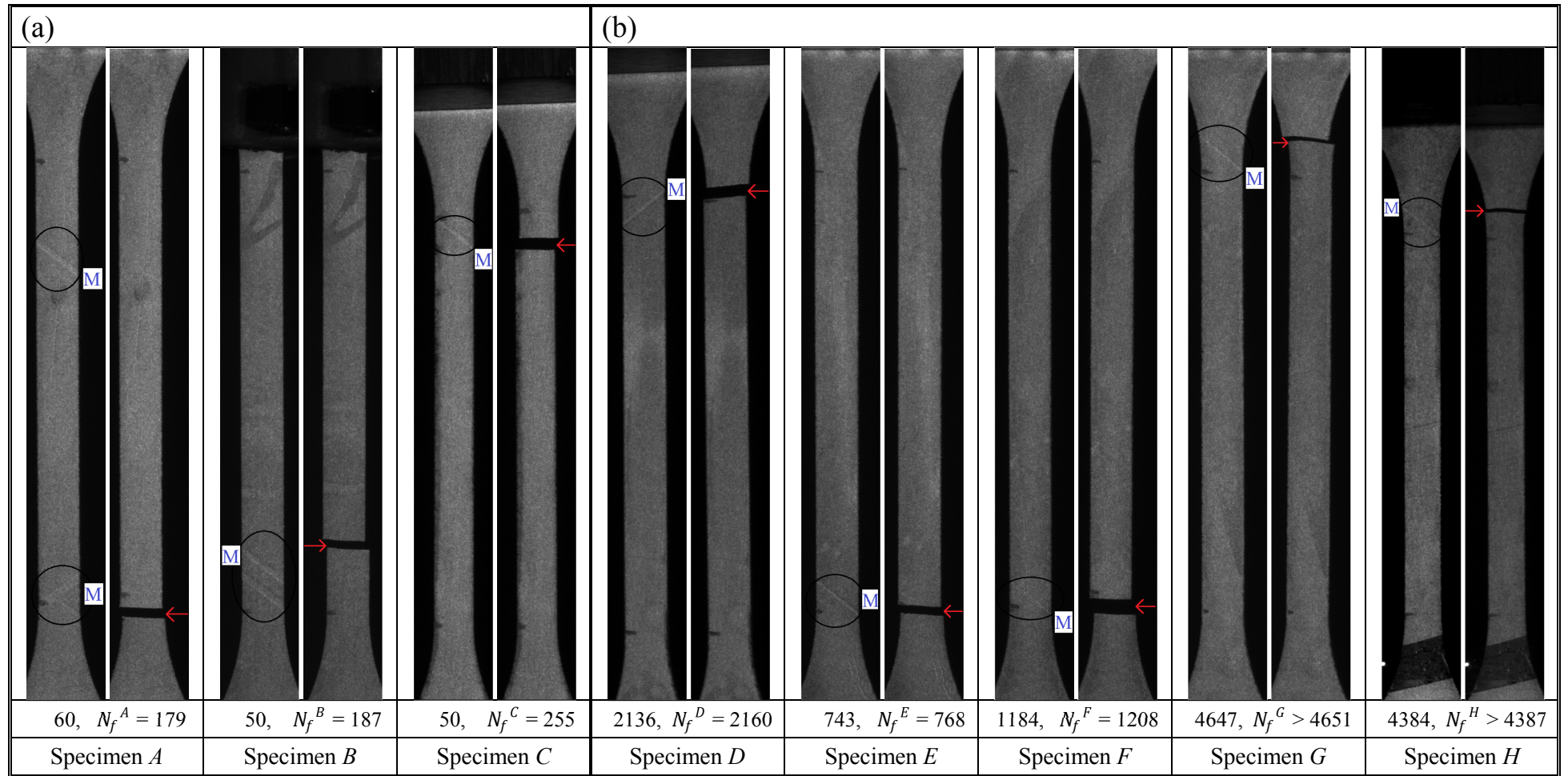


Fig. 2.8 (a) Comparisons between the band locations in the 1<sup>st</sup> “steady-state” cycles and the fatigue failure positions of Specimens A~C. (b) Comparisons between the locations of the 1<sup>st</sup> band nucleation and the fatigue failure positions of Specimens D~H.

The close relation between the Lüders-like band and the fatigue failure is demonstrated in Fig. 2.8, where the comparison between the band locations in the 1<sup>st</sup> “steady-state” cycles and the fatigue failure positions of Specimens *A~C* is given in Fig. 2.8(a), while Fig. 2.8(b) compares the locations of the 1<sup>st</sup> band nucleation and the fatigue failure positions of Specimens *D~H*. The arrows indicate the positions of the failure crack initiation, which are always within the Lüders-like bands (or at the band fronts).

## 2.4 Discussion

The close relation between the band formation and the fatigue failure shown in Fig. 2.8 can be explained as follows. In a uniform NiTi polycrystalline strip under uniaxial tension (where the maximum applied stress is close to the band-nucleation stress, capable to trigger the formation of Lüders-like bands), the bands would nucleate at some weak zones (with more micro-defects) of the strip. Continuous cyclic band nucleation/annihilation would generate and accumulate more defects/damage due to the strong interaction between the localized martensitic phase transformation and the plasticity/defects [51, 74, 75], so the weak zone forming the Lüders-like bands would become weaker and finally lead to the macro-crack initiation and growth. That's why the failure always occurred in the Lüders-like bands. In other words, the Lüders-like band formation is an indicator of the weak zone and the cyclic band nucleation/annihilation accelerates the material's microstructure degradation.

The fatigue failure process in NiTi polycrystals mainly includes three stages: transient stage (shakedown), “steady stage” (“steady-state” cycles) and fracture failure. The “steady stage” is the main part of the fatigue process as the cycle number of the “steady stage” ( $N_{steady-state}$ ) is larger than 70% of the fatigue life  $N_f$  for all the 8

tested specimens. It is noted that Specimens *A~C* with the cyclic band formation/evolution in the “steady stage” have much shorter fatigue lives than Specimens *D~H* without bands in the “steady stage”, which also confirms that cyclic band nucleation/annihilation (localized phase transformation) causes larger microstructure degradation/damage than the cyclic homogeneous deformation (phase transformation macroscopically uniformly distributed in the specimen).

Although the transient stage (shakedown) is not the main part of the fatigue process ( $N_{transient} < 30\% N_f$ ), it causes important/serious microstructure degradation and/or micro-defects rearrangement which not only influences the structural nominal/global responses (see the significant increases of  $\Delta\varepsilon$  and  $D$  in the transient stage in Fig. 2.4(b) and Fig. 2.5(b)), but also changes the positions of the weakest zone — changes the positions of the band formation as shown in the comparison between the reference patterns (the 1<sup>st</sup> band nucleation in the isothermal test) and the patterns ‘d’ in Fig. 2.4(c) and Fig. 2.5(c). Therefore, the fatigue failure does not always occur in the original weakest zones (the positions of the 1<sup>st</sup> band formation in the isothermal tests) as demonstrated in Fig. 2.9 which summarizes the failure positions and the original weakest zones of all the 8 tested specimens. It is indicated that, only in the tests of two specimens (Specimen *C* and Specimen *F*), the failure cracks initiated in the original weakest zones. That means, it is difficult to accurately predict the failure position at the beginning of fatigue tests.

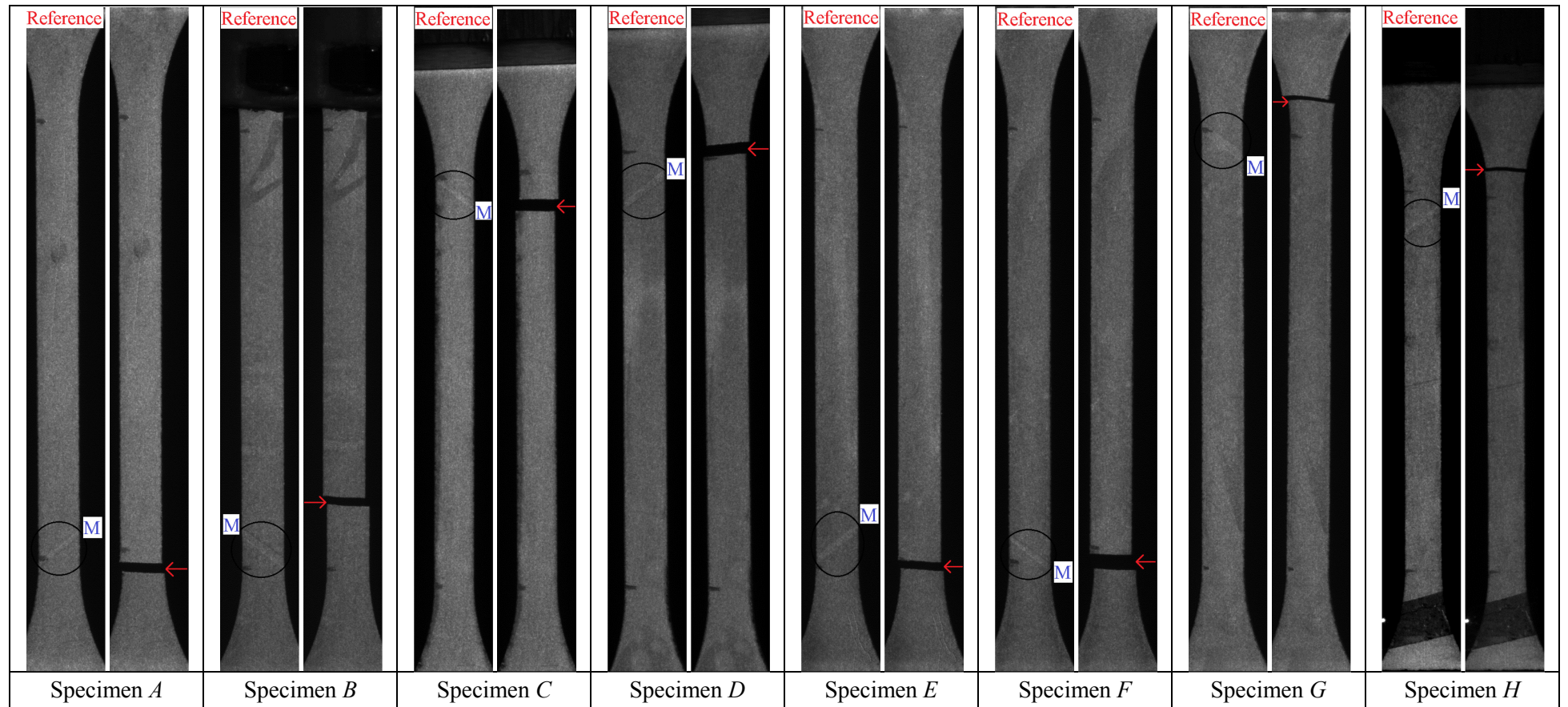


Fig. 2.9 Comparisons between the location of the band formation in the reference isothermal test (left) and the fatigue failure position (right).

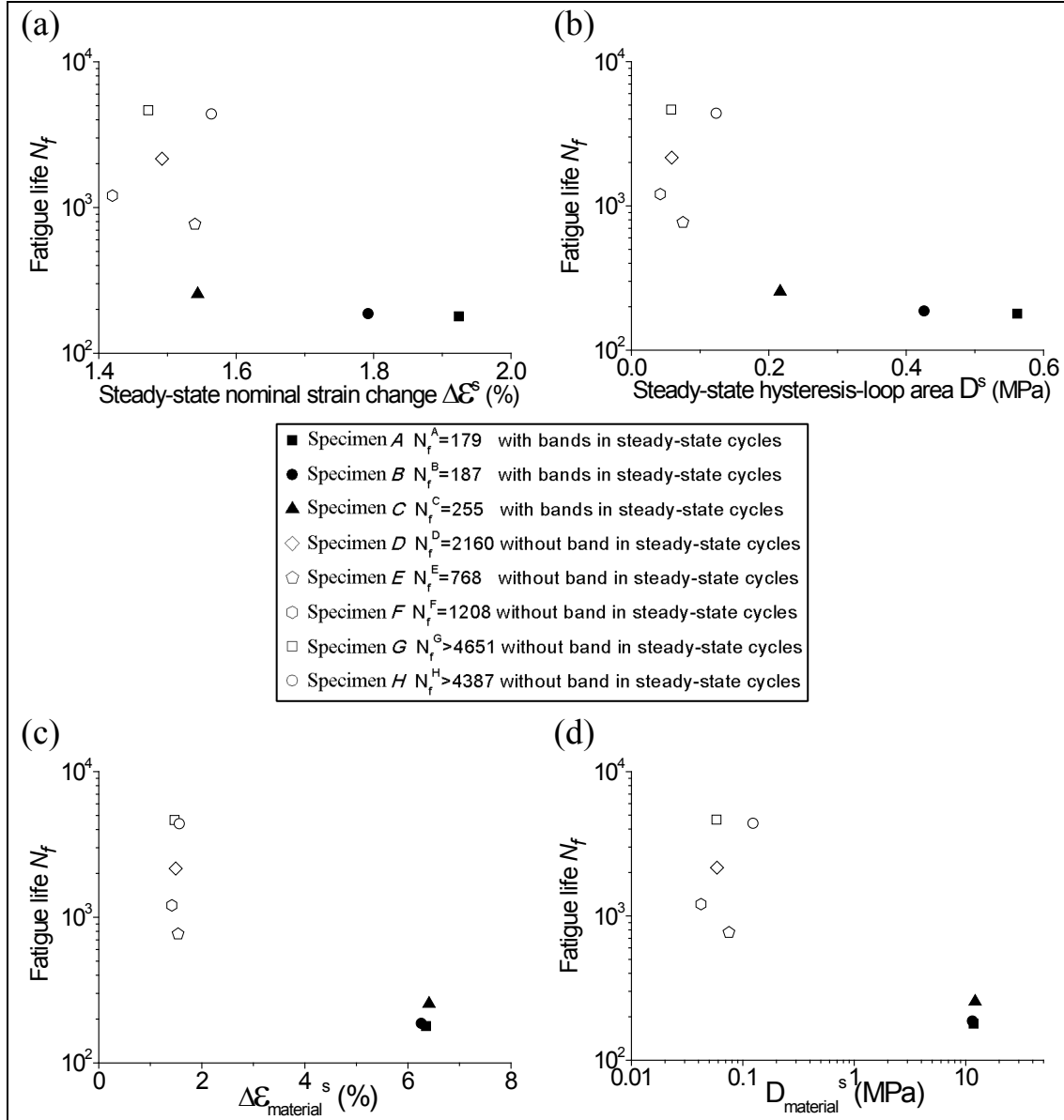


Fig. 2.10 Correlations between the fatigue life  $N_f$  and the **structure responses** in the “steady stage”: (a) change of structural nominal strain  $\Delta \epsilon^s$ , and (b) structural mechanical energy-dissipation density  $D^s$ . Correlations between the fatigue life  $N_f$  and the **material responses** in the “steady stage”: (c) material’s strain change  $\Delta \epsilon_{material}^s$ , and (d) material’s mechanical energy-dissipation density  $D_{material}^s$ .

Fatigue failure criterion is an essential issue in most of the studies on NiTi fatigue behaviors; however, none of the existing fatigue criteria takes into account the effects of the Lüders-like bands. The main fatigue criteria can be classified into three categories: stress-life approach, strain-life approach, and energy-based approach. The 8 specimens presented in this chapter were loaded by the same stress levels ( $\sigma_{min} = 20$  MPa and  $\sigma_{max} = 400$  MPa) but had significantly different fatigue lives ( $N_f = 179 \sim$



4651), depending on the behaviors of Lüders-like bands. So, a fatigue criterion with only stress terms (e.g., mean stress or/and stress amplitude) would not give a proper fatigue prediction, especially when the maximum applied stress is close to the band-nucleation stress. For the strain-life approach and energy-based approach, the usual method is to summarize the fatigue life  $N_f$  in plots like Figs. 2.10(a) and 2.10(b) which try to demonstrate the correlations between  $N_f$  and the strain change  $\Delta\epsilon^s$  and the mechanical energy-dissipation density  $D^s$  of the “steady-state” cycles. However, it should be noted that  $\Delta\epsilon^s$  and  $D^s$  in Figs. 2.10(a) and 2.10(b) are the structure responses, not the material responses especially when the Lüders-like bands exist in the specimens, i.e., the deformation and energy dissipation are not uniformly distributed in the structures (specimens). In order to build the material intrinsic fatigue criteria, the fatigue life  $N_f$  should be correlated with the real material responses. For example, for Specimen *A* with the cyclic band nucleation/annihilation in the “steady-state” cycles (the main stage of the fatigue life), the material inside Lüders-like band (Martensite domain) has a maximum strain  $\epsilon_M \approx 6.4\%$ , i.e., the strain change of the material is  $\Delta\epsilon_{material} = \epsilon_M - \epsilon_{min} \approx 6.4\%$ , which is not equal to the structural nominal strain change in the “steady-state” cycles ( $\Delta\epsilon^s \approx 1.9\%$ ). So, it's better to correlate  $N_f$  with the real material responses by modifying Figs. 2.10(a) and 2.10(b) to Figs. 2.10(c) and 2.10(d). It is noted that when there is Lüders-like band formation, the mechanical energy dissipation is mainly generated by the bands (Martensite domains) whose volume can be measured from the optical images; therefore, the material energy-dissipation density  $D_{material}$  can be roughly estimated as:

$$D_{material} = D \cdot \frac{\text{volume of the gauge section}}{\text{volume of the Martensite domains}} \quad (1)$$



It is noted that  $D_{material}$  is around 10 MPa (see Fig. 2.10(d)), which is much larger than the nominal mechanical energy-dissipation density  $D$  (0.2 MPa  $\sim$  0.6 MPa in Fig. 2.10(b)).

Due to the softening property, NiTi polycrystal is not able to stay in some strain range (e.g., 1.5%~6.5% in this case) except under some constraints [23]. Therefore, studying the material fatigue behaviors in a whole strain range (0~6.5%) needs further delicate experiments. The material intrinsic fatigue criteria are preferred to the structure (strip) fatigue criteria, because the material intrinsic ones can help understand the physical mechanisms of the fatigue process, and provide more reliable input for fatigue computations of various structures in the engineering designs.

### **3. Relation between Lüders-like Band-front Motion and Fatigue**

#### **3.1 Introduction**

Due to the importance of the fatigue behaviors of SMAs, many research efforts have been made to derive proper fatigue criteria to avoid catastrophic events during the applications. In the literature, there are studies on the fatigue life of some medical devices or their representative elements (such as wires [42, 54, 76-79], tubes [74, 80-82], and diamond-shaped elements of stents [83-86]) under different kinds of loadings (e.g., tension, rotary bending) of various strain/stress levels. However, the complex stress/strain states of the fatigue-failure material points in the different specimens (structures) were not clearly addressed; their fatigue data are just valid for particular structures and can't be extracted to form a unified material fatigue criterion. Moreover, most of the existing fatigue tests on NiTi SMAs [12, 37, 51, 57, 87-89] were focused on the structural global responses (nominal stress/strain), ignoring the Lüders-like bands which could form in a stretched NiTi strip due to the material's mechanical softening property [23]. Physically, the martensitic phase transformation (rather than plastic slip) is the key mechanism for the Lüders-like band formation. As seen in Chapter 2, the cyclic nucleation/annihilation of Lüders-like bands was found to have significant effects on the fatigue life of the stretched NiTi strips, but it is still unclear how the Lüders-like band-front motion interacts with the fatigue crack evolution.

So, in this chapter, in order to identify effects of the Lüders-like band-front motion on the fatigue life, strain-controlled tensile fatigue tests were performed, where the band-front position can be controlled by the applied mean strain and the extent of the front motion can be controlled by the strain amplitude (see the cyclic waveform under strain control in Fig. 3.1). Moreover, the specimen's temperature was kept

constant, for which a fan was used to generate air flow to increase the heat transfer between specimen and ambient and the tests were conducted with a low strain rate (around  $10^{-4} \text{ s}^{-1}$ ). It should be noted that although the NiTi polycrystalline sheets used in this chapter were from the same supplier (Johnson Matthey Inc. USA) as those used in Chapter 2, the material composition is a little different — 55.70wt.% Ni compared with 55.89wt.% Ni of the material in Chapter 2; moreover, the long axis of the dog-bone shaped specimens are perpendicular to the rolling direction. In order to establish a material fatigue criterion (not a structure/specimen fatigue criterion), the local strain evolution of the fatigue-failure material point was traced by the method of Digital Image Correlation (DIC) using the commercial software Vic-2D (Correlated Solutions Inc.). Here, the natural surface of the specimen is satisfactory for the DIC processing, so the speckle patterns that would detach from the surface during cyclic loadings were avoided. The optical images were processed in the software Vic-2D with a subset size of  $23 \times 23$  pixels; the local strain accuracy is estimated to be approximately 0.1%.

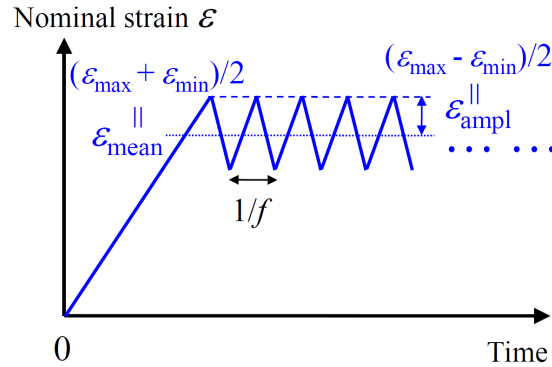


Fig. 3.1 Cyclic waveform under strain control

It is demonstrated that the Lüders-like band itself didn't affect the material's fatigue life, but the band-front motion — band front sweeping a zone (so-called “**active zone**” where the material takes large local strain oscillations with  $A \leftrightarrow M$  phase transformation) had significant effects on the fatigue life; the fatigue failure cracks nucleated in the “active zones” as shown in the Cases I~V of Fig. 3.3.

### 3.2 Results and discussion

First of all, the measurement of the local strain amplitude  $\varepsilon_{ampl}^{local}$  of two typical cases (with the nominal strain amplitude  $\varepsilon_{ampl} = 1\%$  and  $0.5\%$ ) by the method of DIC is illustrated in Fig. 3.2. A number of images are processed (by the Vic-2D software) to obtain the local strain evolution in one “steady-state” cycle, e.g., 200 (100) images for  $\varepsilon_{ampl} = 1\%$  ( $0.5\%$ ). The DIC strain map representing the local strain distribution is consistent with the optical pattern. Specially, the two DIC strain maps corresponding to the loading end (the maximum nominal strain  $\varepsilon_{max}$ ) and the unloading end of the cycle ( $\varepsilon_{min}$ ), respectively, are picked up and then the longitudinal strains ( $\varepsilon_{yy}$ ) along the centerline of the specimen’s gauge section for both the two strain maps are plotted. It is seen in Fig. 3.2(a) that when the nominal strain amplitude is large (with large “active zone” as shown by the optical pattern), the transition zones (Lüders-like band-front) of the two strain profiles are distinct so that the maximum local strain  $\varepsilon_{max}^{local}$  and the minimum local strain  $\varepsilon_{min}^{local}$  can be well determined (the local strain amplitude  $\varepsilon_{ampl}^{local} = \frac{\varepsilon_{max}^{local} - \varepsilon_{min}^{local}}{2}$ ). In other words, the “active zone” in this case is fully developed with a size larger than the band-front (transition-zone) thickness. On the other hand, in Fig. 3.2(b) when the nominal strain amplitude is small, the “active zone” is not fully developed whose size is comparable with the band-front thickness, so the local strain amplitude is defined as the half of the strain difference of the transition zone as shown in Fig. 3.2(b). In the following, all the values of the local strain amplitude are determined by this method based on the DIC strain maps, making it possible to derive a fatigue criterion based on the local strains near the fatigue-failure material points. Note that the centerline is not the exact fracture position, but it was carefully verified

that the target point on the centerline (whose local strain is used) is in the same “active zone” or at the same inclined band front of the real failure point.

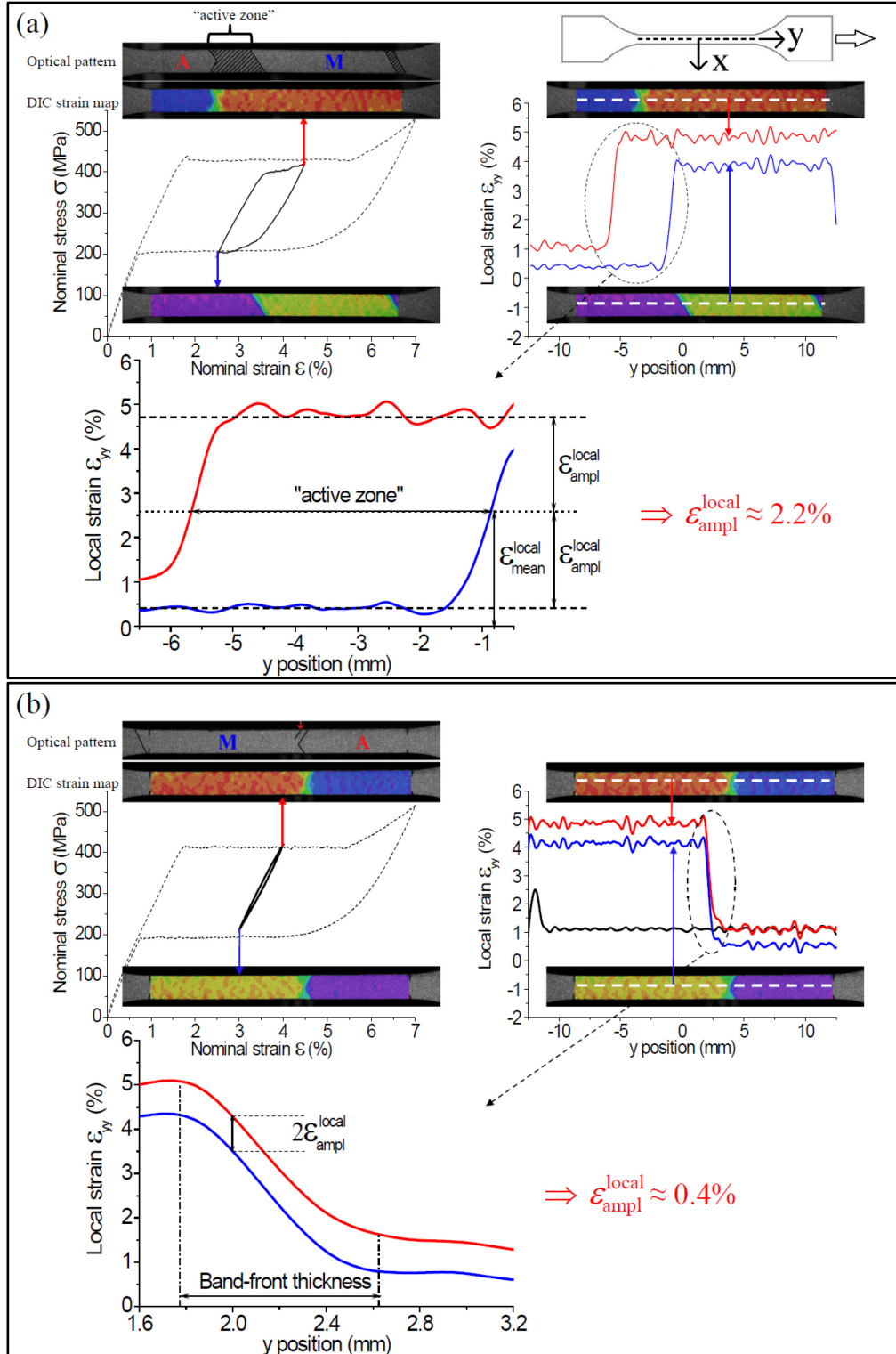


Fig. 3.2 DIC measurement of the local strains for two typical cases (nominal strain amplitude  $\epsilon_{ampl} = 1.0\%$  and  $0.5\%$ ): (a) fully-developed “active zone” and (b) partially-developed “active zone” whose size is comparable to the band-front thickness.

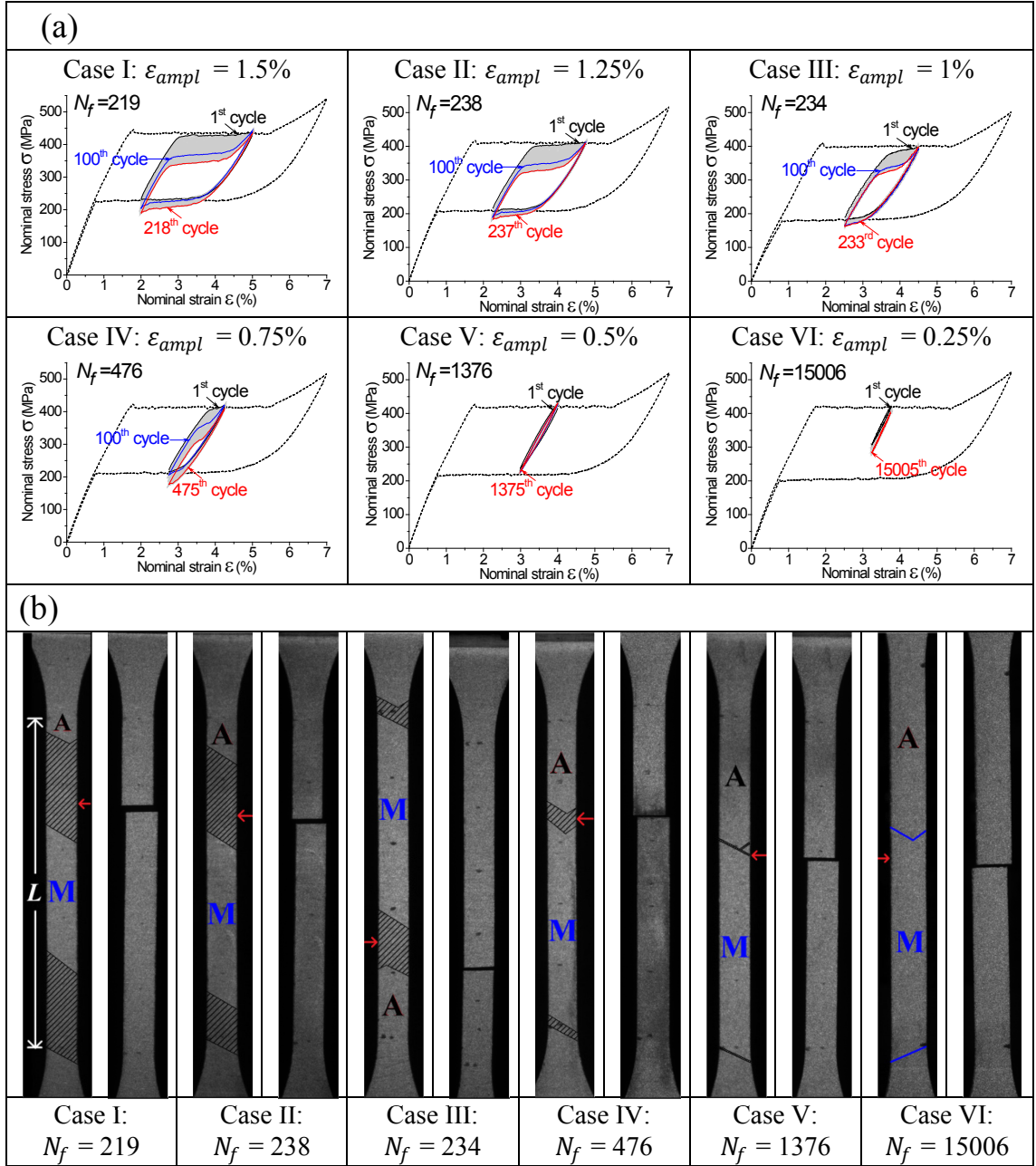


Fig. 3.3 (a) Nominal stress-strain curves of fatigue cycles (solid lines: the black, blue, red lines respectively represent the 1<sup>st</sup>, the 100<sup>th</sup>, and the final cycle before failure) of the specimens under a fixed nominal mean strain ( $\varepsilon_{mean} = 3.5\%$ ) with different nominal strain amplitudes ( $\varepsilon_{ampl} = 1.5\% \sim 0.25\%$ ) in comparison with their isothermal curves (dashed lines); (b) The corresponding Lüders-like band evolution (with “active zones” (shaded zones) in Cases I~V and without “active zones” in Case VI) and the final fractured specimens, where the red arrows indicate the fatigue-failure crack nucleation positions.

Figure 3.3 shows the evolution of the nominal stress-strain curves of the fatigue tests (under a fixed nominal mean strain  $\varepsilon_{mean} = 3.5\%$  with different nominal strain amplitudes as shown by the solid curves in Fig. 3.3(a)) and the corresponding patterns of the Lüders-like bands and the fracture failure positions (Fig. 3.3(b)). It is

seen that when the nominal strain amplitude is large ( $\varepsilon_{ampl} = 1.5\%$ ,  $1.25\%$ , and  $1.0\%$  in Cases I, II, and III), there are stress-plateaus in the stress-strain curves, and the band fronts move and sweep over large zones during the cyclic loadings (see the shaded zones of Cases I, II, and III in Fig. 3.3(b)). These “active zones” (cyclically swept by the moving fronts) contain grains taking cyclic Austenite (A)  $\leftrightarrow$  Martensite (M) phase transformation, leading to larger microstructure damage than the cyclic “elastic” deformation in the other zones — the unshaded zones including the Austenite domains (with a local strain  $\varepsilon_A^{local} \approx 1\%$  by DIC measurement) where most of grains remain Austenite phase, and the Martensite domains (with a local strain  $\varepsilon_M^{local} \approx 5\%$ ) where most of the grains have transformed to M phase [34]. As expected, the fatigue failure cracks nucleated within the “active zones” (see the fatigue-crack nucleation positions indicated by the red arrows in the patterns of Fig. 3.3(b)). The numbers of cycles to failure (fatigue lives  $N_f$ ) of Cases I, II, and III have almost the same value (around 200) because, from a material point of view, the material in the “active zone” of these three cases takes almost the same cyclic deformation (the amplitude of the local strain in the “active zone”  $\varepsilon_{ampl}^{local} = 2.15\%$  as shown in Fig. 3.3(a)). In other words, the fatigue life of the stretched strip is independent of the nominal strain amplitude (i.e., independent of the size of “active zones” in comparing Cases I, II, and III of Fig. 3.3(b)).

By contrast, when the applied nominal strain amplitude  $\varepsilon_{ampl}$  is lower than  $1\%$ , the fatigue life of the strip significantly depends on  $\varepsilon_{ampl}$  as shown in Cases IV, V, and VI, where  $N_f$  changes from  $\sim 4 \times 10^2$  to  $\sim 1.5 \times 10^4$ . It is seen in Fig. 3.3(b) that, although the “active zones” are small (whose length  $l$  along the loading axis is comparable to the specimen’s width or thickness) when  $\varepsilon_{ampl}$  are  $0.75\%$  (Case IV) and  $0.5\%$  (Case V), the fatigue failure cracks still nucleated within the “active zones”.

Interestingly, when the nominal strain amplitude reduces to 0.25% (Case VI), the band fronts (the blue lines in the pattern of Case VI in Fig. 3.3(b)) didn't move (no "active zone") and the fatigue failure crack obviously nucleated away from the immobile band fronts! Normally, the band fronts were thought to be positions with certain stress-concentrations, favorable for the fatigue crack nucleation; however, the results of Case VI (repeated by several specimens) imply that the immobile band front is not the weakest zone of the strip in the fatigue cycles.

It is also seen in Fig. 3.3 that, with the control of the nominal strain in the tests, the stress level changes with the cycle number due to material microstructure change (degradation), so-called "shakedown process". When the nominal strain amplitude  $\varepsilon_{ampl}$  is large (with a large "active zone") such as Cases I, II, and III, the upper-plateau stress  $\sigma_0^{A \rightarrow M}$  reduces with increasing the cycle number, especially in the first 100 cycles. The reduction of  $\sigma_0^{A \rightarrow M}$  from the 1<sup>st</sup> cycle to the final cycle (just before the failure cycle) for Case I ( $\varepsilon_{ampl} = 1.5\%$ ) is around 85 MPa. On the other hand, when the nominal strain amplitude is small (without "active zones") such as Cases VI ( $\varepsilon_{ampl} = 0.25\%$ ), the stress reduction from the 1<sup>st</sup> cycle to the final cycle is only around 20 MPa. It seems that a large stress reduction (implying large/fast microstructure degradation/damage) leads to a short fatigue life.



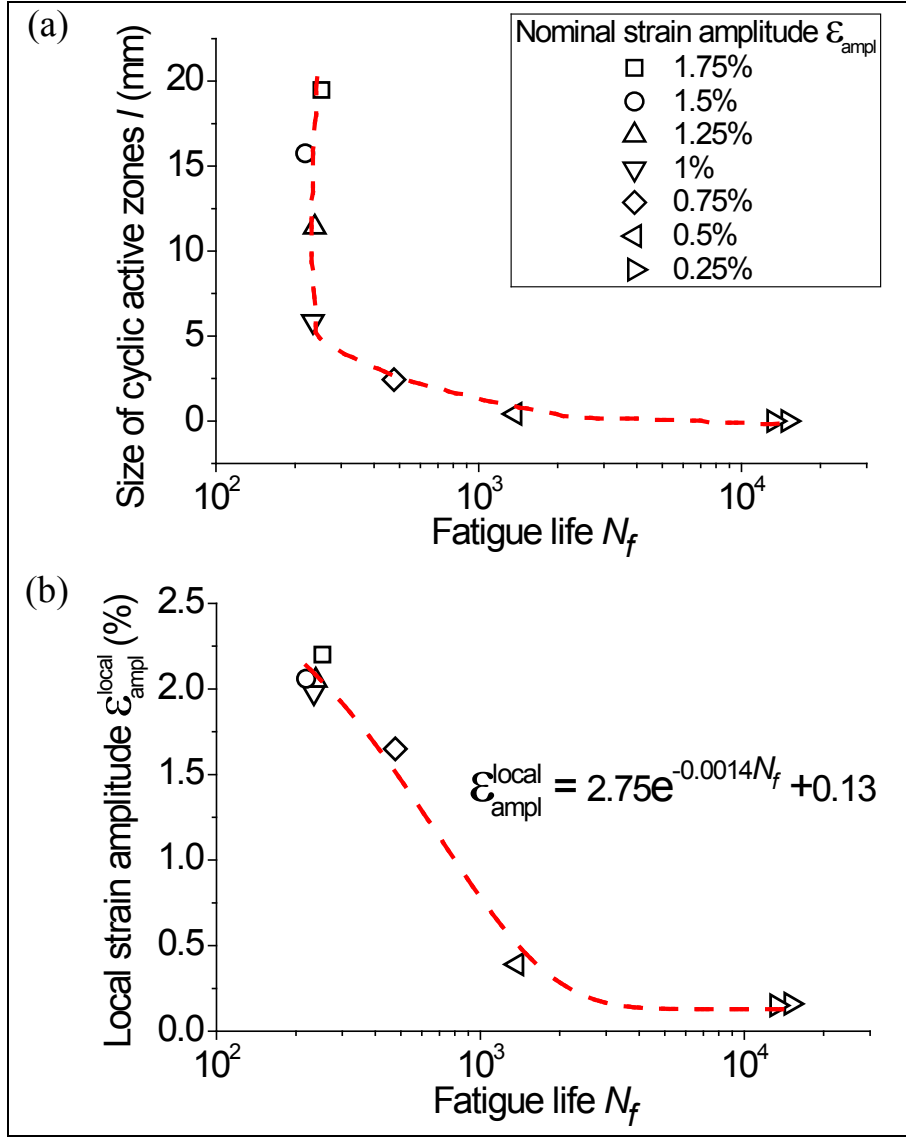


Fig. 3.4 Dependences of the fatigue life  $N_f$  on (a) the size of “active zones”  $l$  and (b) the local strain amplitude  $\epsilon_{ampl}^{local}$  of the fatigue-failure material points.

Figures 3.4(a) and 3.4(b) summarize the fatigue lives  $N_f$  of the above tensile tests in terms of the size of “active zones” ( $l$ , the total length of the “active zones” along the loading axis) and the local strain amplitude  $\epsilon_{ampl}^{local}$ , respectively. In fact, when the “active zones” are large,  $l$  can be roughly estimated by a simple formula [25, 68]:  $l = \frac{L \cdot 2\epsilon_{ampl}}{\epsilon_M - \epsilon_A}$ ; but here in Fig. 3.4(a), the values of  $l$  are obtained from the optical measurement. It is seen that the  $l$ -dependence of the fatigue life can be divided into three regions: (1) when  $l$  is large (with  $\epsilon_{ampl} \geq 1\%$ ), the “active zones” are fully

developed,  $N_f$  is small (around 200) and independent of  $l$  (i.e., independent of  $\varepsilon_{ampl}$ ); (2) when  $l$  reduces to a level comparable to the specimen's width (2.5 mm) or thickness (0.2 mm) ( $\varepsilon_{ampl} = 0.75\%$  and  $0.5\%$ ),  $N_f$  increases significantly; (3)  $l$  is zero when  $\varepsilon_{ampl} \leq 0.25\%$ , the fatigue life is long (larger than  $10^4$ ) and the fatigue failure occurs in the Martensite domain as shown in the pattern of Case VI of Fig. 3.3(b) — that means the cyclic “elastic” deformation of the M phase has a fatigue life longer than  $10^4$ , which is higher (by two orders of magnitude) than  $N_f$  of the material taking cyclic A $\leftrightarrow$ M phase transformation (around 200). By comparing Figs. 3.4(a) and 3.4(b), it is seen that while the fatigue life  $N_f$  significantly depends on the local strain amplitude,  $N_f$  is independent of the nominal strain amplitude when  $\varepsilon_{ampl} \geq 1\%$  because the local strain amplitude is almost the same ( $\varepsilon_{ampl}^{local} \approx 2.1\%$ ) in the fully-developed “active zones”. Fig. 3.4(b) in fact provides a simple material fatigue criterion: with the decrease of the local strain amplitude (i.e., decrease of the degree of cyclic phase transformation in the grains of the “active zones”), the damage/degradation per cycle would become less, which leads to longer fatigue life.

It is also implied in Case VI of Fig. 3.3(b) that the fatigue life of Martensite phase is shorter than that of Austenite phase, because the fatigue failure occurred in the M domain while the coexisting A and M domains were subjected to the same cyclic tensile loadings. For a comparison of the fatigue life between the “elastic” deformations of A and M domains, another loading scheme was adopted in the following fatigue tests — a fixed nominal strain amplitude  $\varepsilon_{ampl} = 0.25\%$  (no “active zones”) with different mean strains as shown in Fig. 3.5. When the nominal mean strain was small ( $\varepsilon_{mean} = 1.45\%$  in Case I of Fig. 3.5), there was no Lüders-like band and the specimen didn't fail after  $3 \times 10^4$  cycles; that means with only cyclic “elastic” deformation, the Austenite phase has a fatigue life larger than  $3 \times 10^4$  cycles. By

contrast, Cases II, III, and IV with high nominal mean strains (3.25% ~5.25%) have similar fatigue lives (around  $1.5 \times 10^4$  cycles) and the fatigue failure cracks nucleated in the M domains (see Fig. 3.5). Interestingly, when  $\varepsilon_{mean}$  increases to 6.25% (Case V, achieved by first increasing the stress to be higher than the isothermal upper-plateau stress  $\sigma_0^{A \rightarrow M}$  and then unloading close to  $\sigma_0^{A \rightarrow M}$ ), the fatigue life of this M phase (so-called “**unloading Martensite**” phase) is around  $2.1 \times 10^4$  cycles which is slightly longer than that ( $N_f \approx 1.5 \times 10^4$ ) of the previous M phase (so-called “**loading Martensite**” phase). That might be due to the different microstructures in these two M phases — the “loading M” phase (with the local mean strain  $\varepsilon_{mean}^{local}$  around 4.8%) could take at most 70% martensitic phase transformation [34] while the “unloading M” phase having experienced higher stress (with  $\varepsilon_{mean}^{local}$  around 5.2%) would have more phase transformation and/or martensitic reorientation [90-92].

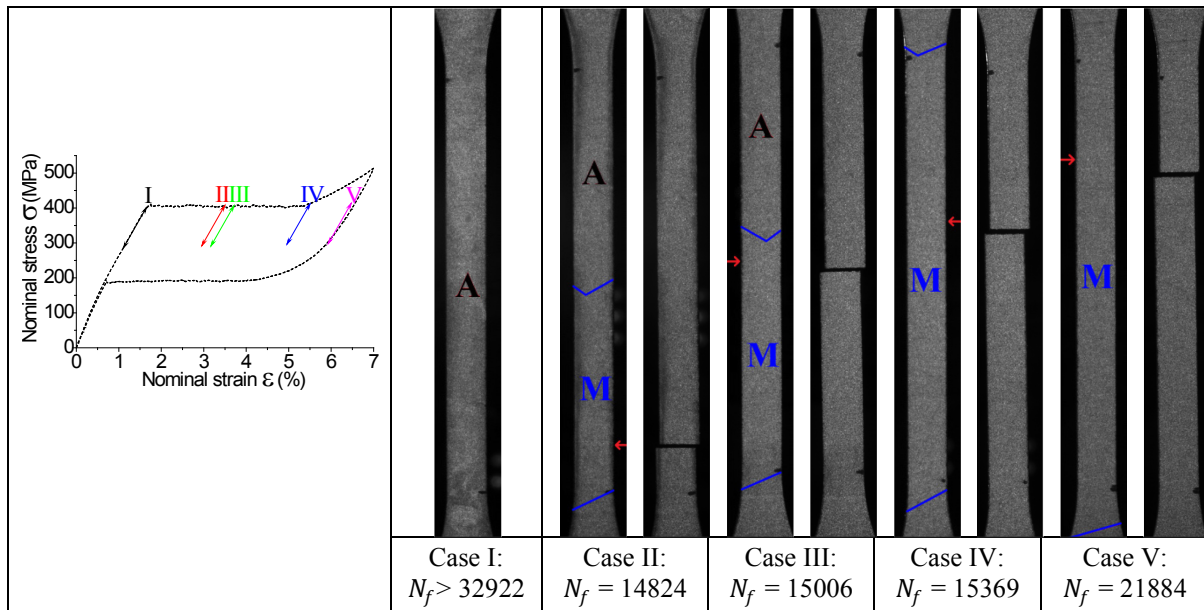


Fig. 3.5 The deformation domains and the final fractured specimens in the fatigue tests with fixed nominal strain amplitude  $\varepsilon_{ampl} = 0.25\%$  (no “active zones”) and different nominal mean strains  $\varepsilon_{mean}$  (note: the specimen didn’t fail after 32922 cycles in Case I);

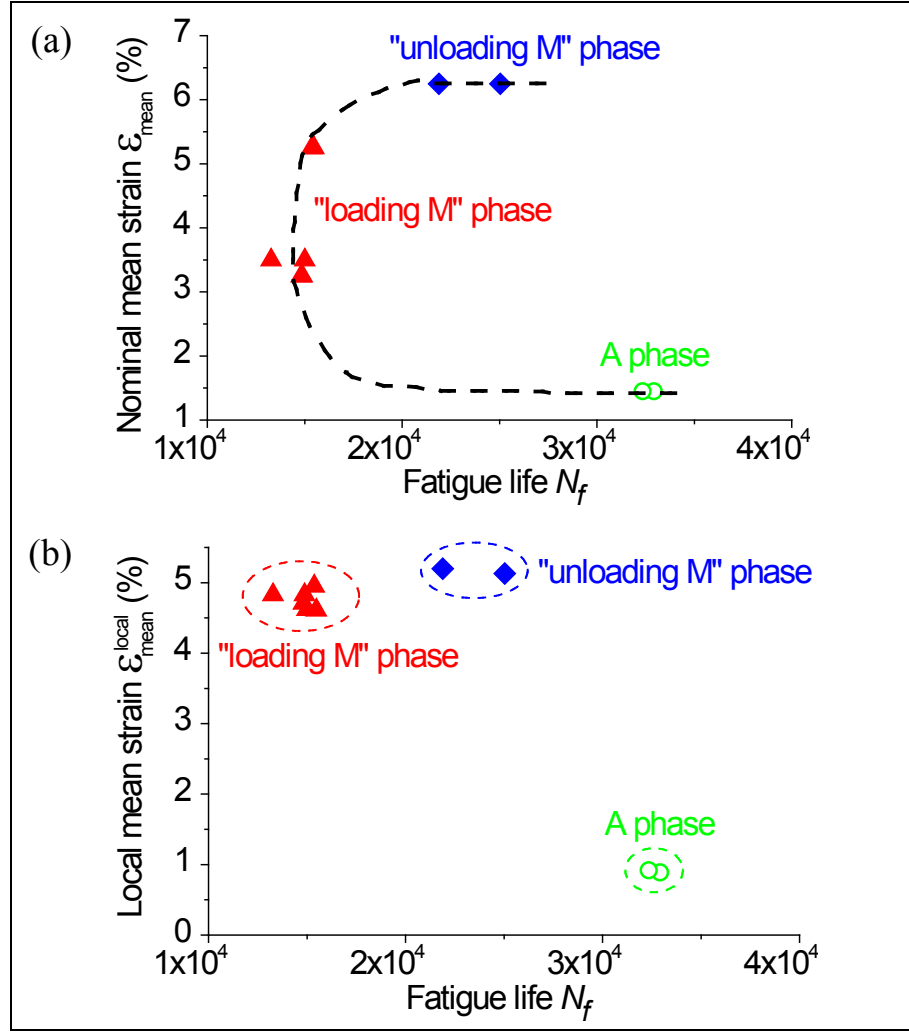


Fig. 3.6 (a) The dependence of the fatigue life  $N_f$  on  $\epsilon_{mean}$ ; (b) The dependence of  $N_f$  on the local mean strain  $\epsilon_{mean}^{local}$  (solid/open symbols represent the tests with/without fracture failure).

Figures 3.6(a) and 3.6(b) summarize the fatigue lives  $N_f$  of the “elastic” deformation in terms of the nominal mean strain  $\epsilon_{mean}$  and the local mean strain  $\epsilon_{mean}^{local}$ , respectively. It is seen in Fig. 3.6(a) that  $N_f$  depends non-monotonically on the nominal mean strain  $\epsilon_{mean}$ : when  $\epsilon_{mean}$  is in the medium range (between around 1.5% and 6.0% with coexistence of the Austenite and Martensite domains), the fatigue life  $N_f$  is independent of  $\epsilon_{mean}$ ; however, when  $\epsilon_{mean}$  is small (less than around 1.5% with only A domains) or large (higher than 6.0% with only M macro-domains),  $N_f$  is dependent on the  $\epsilon_{mean}$  because the fatigue lives of the “elastic” deformation of M and A domains are normally different to each other. While the nominal mean strain

$\varepsilon_{mean}$  can vary continuously from  $\sim 1.5\%$  to  $\sim 6.0\%$  by externally controlling the specimen's displacement, the local mean strain  $\varepsilon_{mean}^{local}$  in the material can't change continuously as shown in Fig. 3.6(b):  $\varepsilon_{mean}^{local}$  can only take some discrete values corresponding to the A phase (with local strain around 1%) and M phases (with local strain around 5%) due to the material softening property. Of course, in the above fatigue tests of “elastic” deformation, there could be material points at the band front (diffusive interface zone) having local strains in between these two typical values (1% and 5%), but the fatigue failure didn't occur at the immobile band front; as a result, no fatigue-life data of the material at the immobile band front under only “elastic” deformation has been obtained.

The results of Figs. 3.3-3.6 demonstrate that the fatigue-failure material points in the NiTi polycrystalline strips under tensile fatigue tests can take one of the four states: A $\leftrightarrow$ M phase transformation (with “active zones” cyclically swept by the moving band fronts), “elastic” deformation of A phase, “loading M” phase, or “unloading M” phase. Comparing with the description of fatigue behaviors in terms of the structural global responses (nominal strain amplitude and nominal mean strain), tracing the behaviors of the fatigue-failure material point under different states (in terms of the local strain variation by DIC measurements) provide more information for understanding and prediction on the material fatigue behaviors.

In Chapter 2, it is seen that in the stress-controlled tests with in-situ optical observation by a fast camera, the fatigue cracks (of a size larger than 100  $\mu\text{m}$ ) are only visible in the last several cycles and then quickly lead to the fracture failure of the specimens. But, here in a strain-controlled test with a digital microscope, the development of a crack from a size of  $\sim 50 \mu\text{m}$  to  $\sim 90 \mu\text{m}$  at a Lüders-like band-front was captured in the last 100 fatigue cycles with the nominal strain amplitude of 0.5%

(see Fig. 3.7). Interestingly, it was not this crack (with a final size of  $\sim 90\ \mu\text{m}$  which is invisible through optical cameras) that caused the fatigue failure — the fracture of this specimen occurred at the other band front out of the gauge section. This means that multiple cracks nucleated in the specimen but one of them grew faster than others (such as the observed one) and led to the final fracture. The local observation by microscope and together with other experimental methods (e.g., X-ray Diffraction, Electron Backscatter Diffraction, etc.) could help to reveal the crack initiation and propagation in SMAs, but more cautious efforts have to be taken on these experiments which could be the future work.

### **3.3 Summary**

The fatigue experiments with in-situ optical observation demonstrate that the Lüders-like band-front motion triggering localized cyclic phase transformation leads to a short fatigue life; by contrast, the material under cyclic “elastic” deformation (without the band-front motion) has a longer fatigue life whose level depends on the material state (Austenite, “loading Martensite”, or “unloading Martensite” phase), and the fatigue failure crack doesn’t nucleate at the immobile band front. The optical observation on the band evolution and the DIC measurement of the local strains help explain the non-trivial dependence of the fatigue life of a NiTi SMA structure (strip) on the nominal strain variation and provide hints for developing a material fatigue criterion in terms of the local strain variation of the fatigue-failure material points.

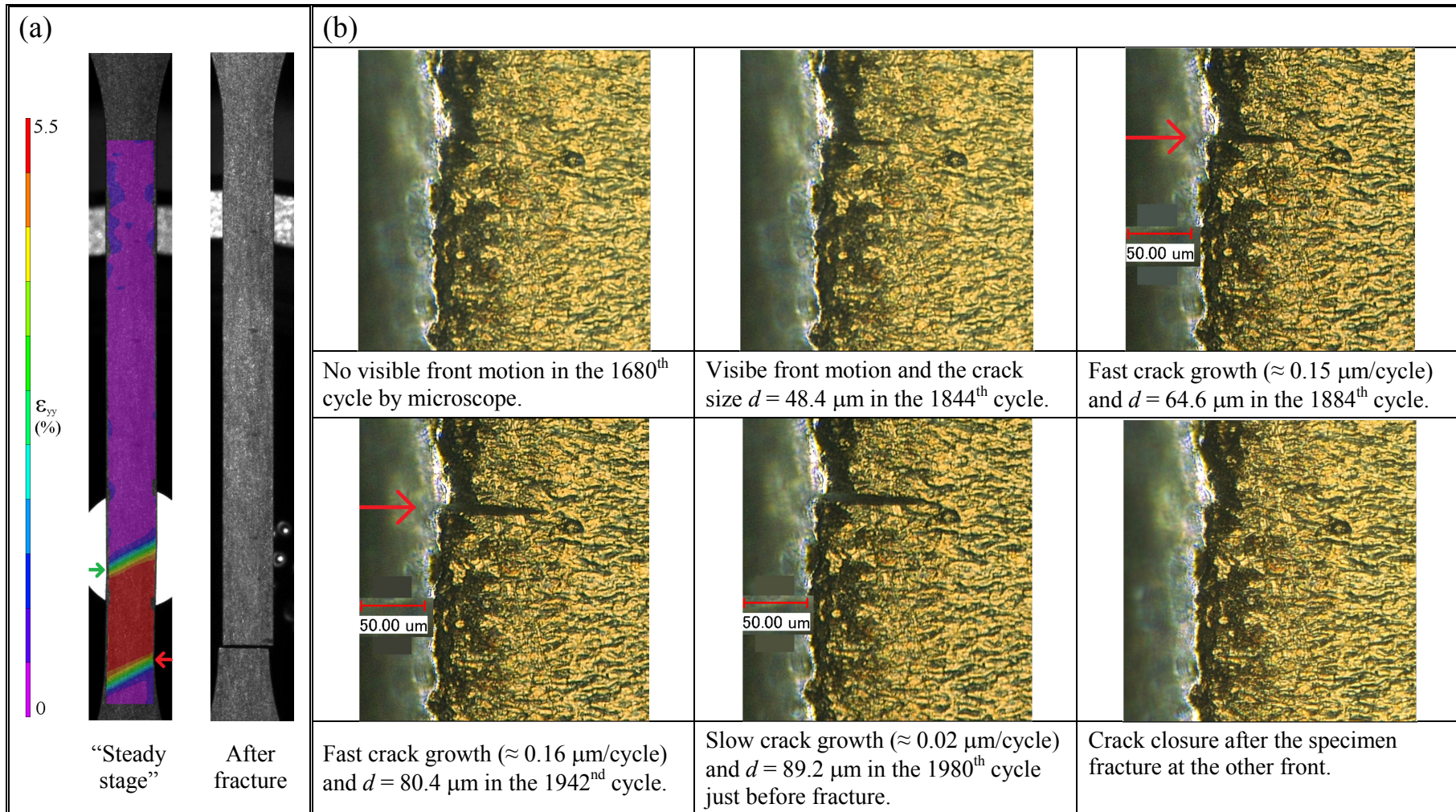


Fig. 3.7 (a) Global observation by optical camera on a specimen with small cyclic “active zones” (shaded zones) under the nominal strain amplitude of 0.5% and (b) Local observation by microscope on the evolution of a macro crack at the left end of the upper band front in (a).



## 4. Band-Pattern Evolutions and Material Fatigue Criterion

### 4.1 Introduction

It is seen in Chapters 2 and 3 that the Lüders-like band formation and evolution (band-front motion) have significant effects on the fatigue behaviors of pseudoelastic NiTi polycrystalline strips under uniaxial tension — the cyclic band nucleation/annihilation triggering the localized martensitic phase transformation leads to more microstructure degradation and shorter fatigue lives than the cyclic homogeneous deformation. Moreover, a fatigue criterion should adopt the local material responses rather than the structural global/nominal responses in order to accurately predict the fatigue life; in particular, it is found that the local strain amplitude is a good indicator on the fatigue life (see Fig. 3.4(b)) when the specimens are loaded with a similar maximum stress level and without large temperature variations. However, in the real applications of SMAs, there are a number of factors that need to be considered, such as the material's microstructure effects [4, 42, 46, 49, 93, 94], experiment temperatures [4, 5, 95, 96], levels/amplitude of the applied stress/strain [4, 8, 12, 37, 42, 46, 50, 57, 81, 95, 96], and loading rate (frequency) [4, 9, 22, 51, 89, 96, 97], etc..

Many previous studies [26, 60, 62, 68, 98-100, and among many others] have shown that the Lüders-like band formation in NiTi polycrystals depends on the loading stress and frequency, which are expected to influence the material's fatigue behaviors. In this chapter, systematic stress-controlled tensile fatigue tests, similar to those described in Chapter 2 (on the specimens cut from the same batch of NiTi sheets with a composition of 55.89wt.% Ni and under the same cyclic waveform (see Fig. 2.1)), were conducted on the NiTi polycrystalline strips with in-situ optical observation on the Lüders-like band formation/evolution and the DIC method to trace the deformation



history (local strain variations) of the fatigue-failure material points in the specimens, demonstrating the stress- and frequency-dependent inhomogeneous deformations of the NiTi strips and the associated fatigue behaviors. It was further identified that the apparent/nominal residual strain (determined from the minimum output strain of the nominal stress-strain curve) was caused by the irrecoverable microstructure degradation/damage and the recoverable “**thermo-stabilized Martensite**” (residual Martensite bands observed at the end of the cyclic unloading), depending on the applied stress and frequency. And the average accumulation rate of the local residual strain near the fatigue-failure material points is a good indicator on the material’s fatigue life.

## 4.2 Experimental results

In the following, results of a 50-cycle stress-controlled tensile test on Specimen *T* were first reported in Section 4.2.1 to illustrate the Lüders-like band pattern evolution and the appearance of the “thermo-stabilized Martensite” bands that disappeared when the cyclic test was stopped. Results of the stress-controlled fatigue tests are divided into three sections (Sections 4.2.2 to 4.2.4) according to the applied stress level  $\sigma_{max} = 500$  MPa (much higher than the band-nucleation stress  $\sigma_0^N$ ),  $\sigma_{max} = 400$  MPa (close to  $\sigma_0^N$ ), and  $\sigma_{max} = 300$  MPa (much lower than  $\sigma_0^N$ ), where three loading frequencies  $f$  of 0.01 Hz, 0.1 Hz, and 1 Hz were employed. For each loading scheme, 3-4 specimens were tested to check the results’ reliability. To indicate the loading condition of each specimen, a special designation is applied by using the letters “*A*”, “*B*”, “*C*”, or “*D*” with the value of  $\sigma_{max}$  as subscript and the value of  $f$  as superscript, such as  $A_{500}^{0.01}$ , indicating the Specimen *A* tested under  $\sigma_{max} = 500$  MPa and  $f = 0.01$  Hz. All the tested specimens were extracted from the same batch of NiTi

sheets, showing similar isothermal mechanical properties: in Fig. 4.1, the Austenite (A)  $\rightarrow$  Martensite (M) (M $\rightarrow$ A) plateau stress at room temperature ( $T_0 \approx 21^\circ\text{C}$ )  $\sigma_0^{A \rightarrow M}$  ( $\sigma_0^{M \rightarrow A}$ ) is around 353.1 MPa (150.6 MPa) and the band-nucleation stress (the peak value before the stress drop to the upper plateau stress)  $\sigma_0^N$  varies from 366.4 MPa to 393.8 MPa.

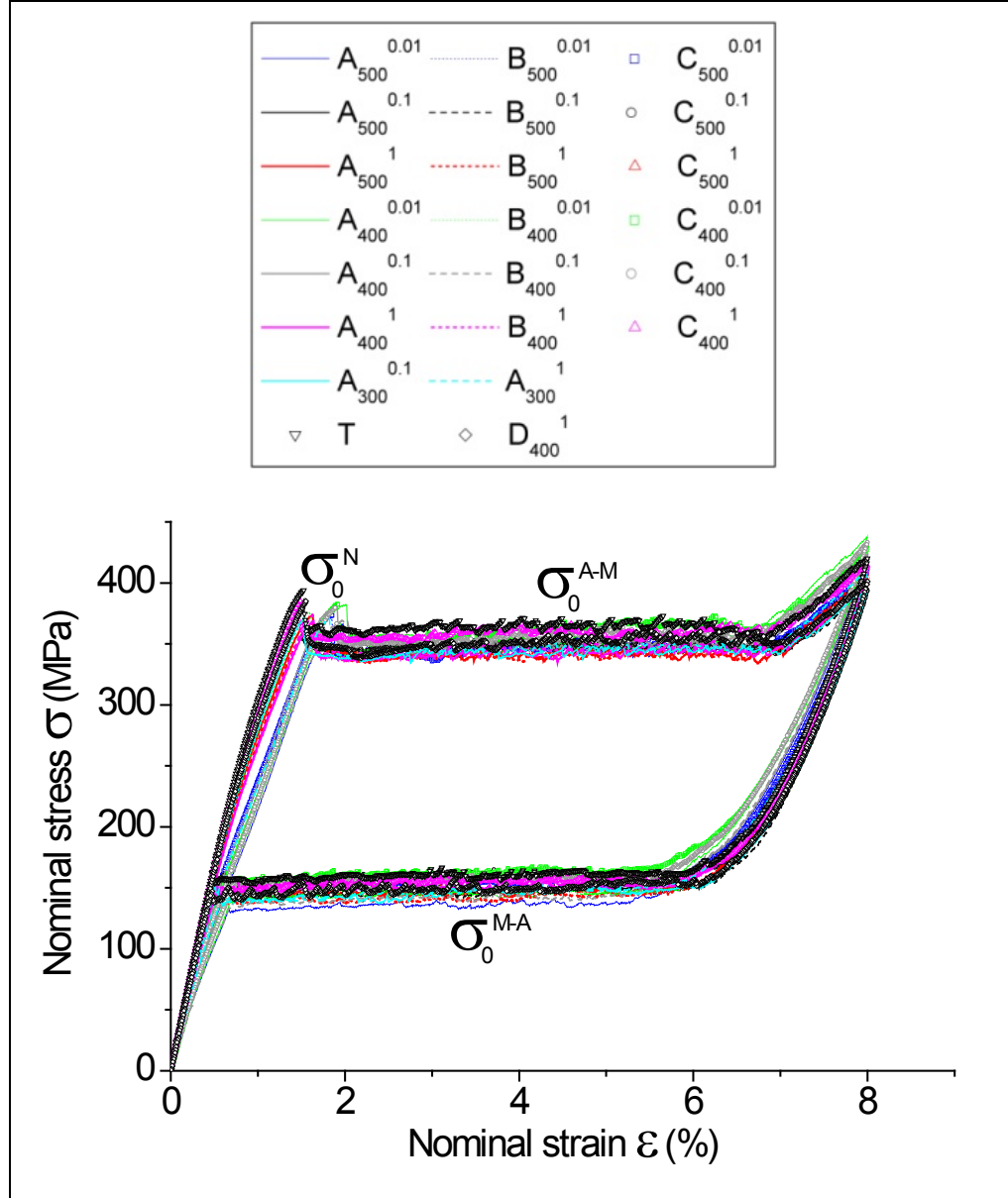


Fig. 4.1 All the tested specimens have similar stress-strain curves in the isothermal strain-controlled tensile tests with global strain rate of  $8 \times 10^{-5} \text{ s}^{-1}$ .  $\sigma_0^{A \rightarrow M}$  ( $\sigma_0^{M \rightarrow A}$ ) denotes the transformation stress during the Austenite (A)  $\rightarrow$  Martensite (M) (M $\rightarrow$ A) phase transformation and  $\sigma_0^N$  denotes the band-nucleation stress at room temperature  $T_0 \approx 21^\circ\text{C}$ .

4.2.1 Lüders-like band pattern evolution and appearance of “thermo-stabilized Martensite” during a stress-controlled cyclic test

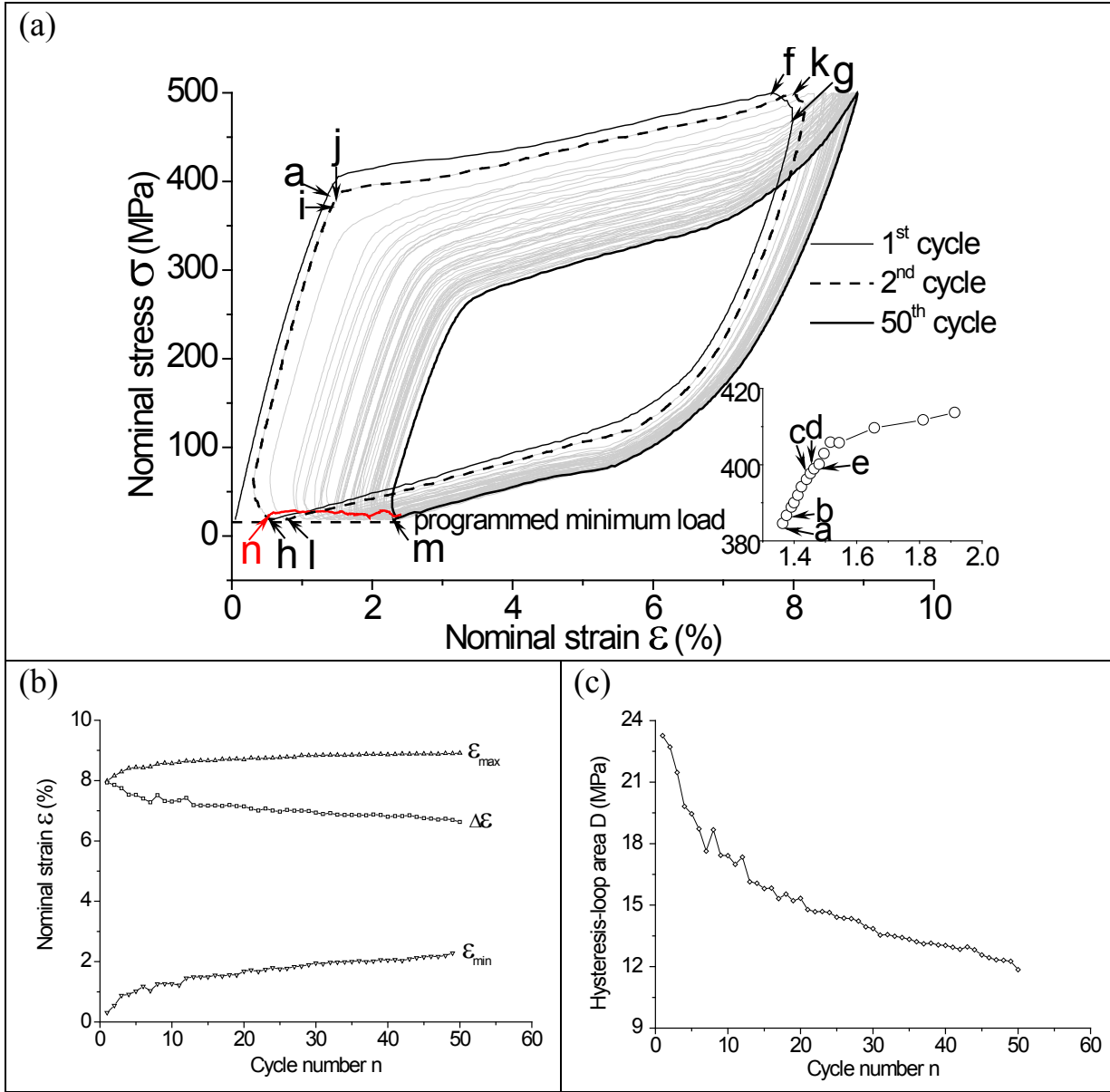


Fig. 4.2 The stress-controlled cyclic tensile test on **Specimen T** with the maximum stress  $\sigma_{max} = 500$  MPa and the loading frequency  $f = 0.01$  Hz for 50 cycles: (a) the evolution of the stress-strain  $\sigma - \epsilon$  curve, (b) evolutions of cycle-minimum nominal strain  $\epsilon_{min}$ , cycle-maximum nominal strain  $\epsilon_{max}$ , and nominal strain change  $\Delta\epsilon = \epsilon_{max} - \epsilon_{min}$ , (c) the evolution of the mechanical energy-dissipation density  $D$ .

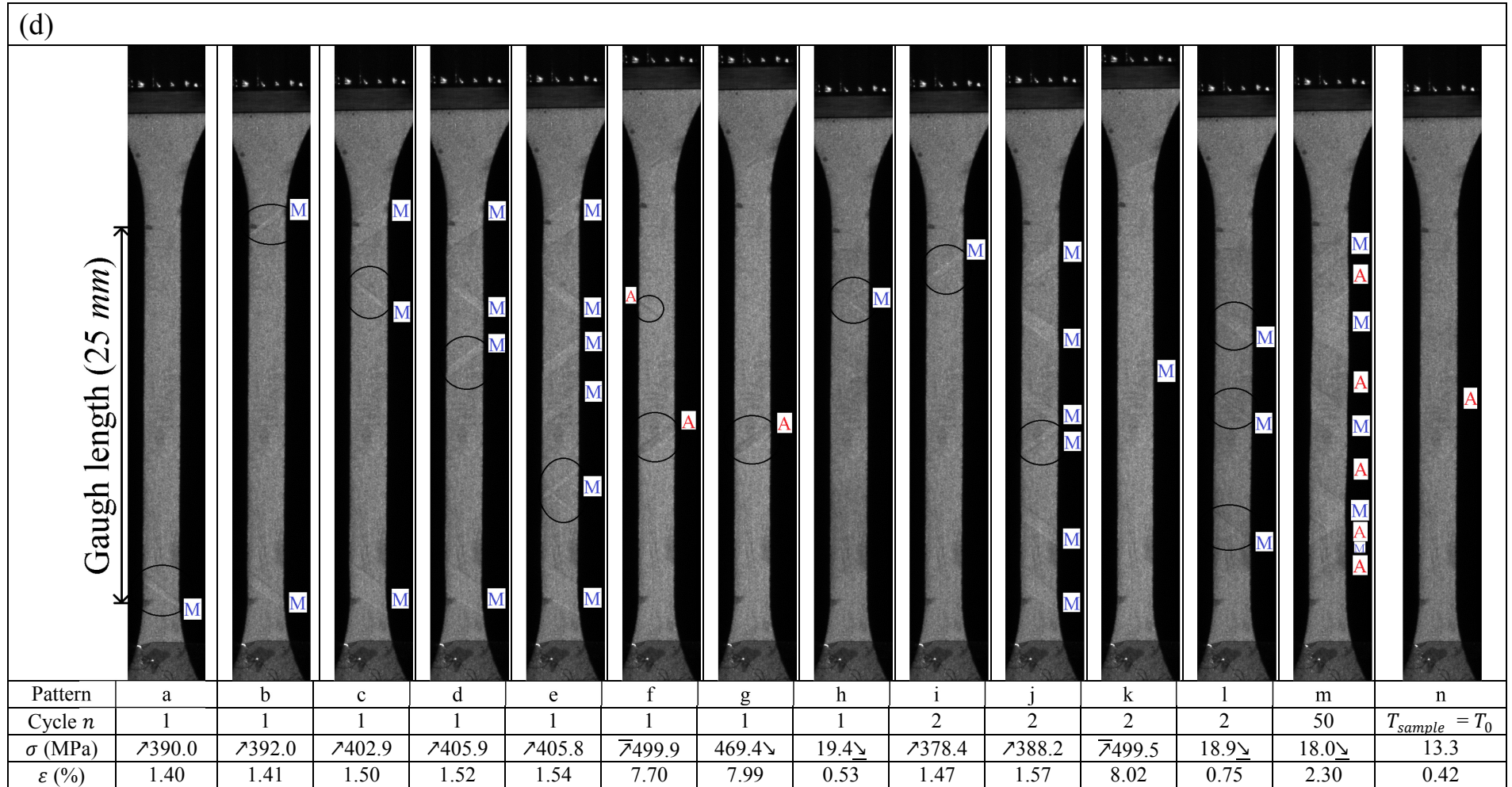


Fig. 4.2(d) The optical observation on the Lüders-like band patterns of **Specimen T**. The values of the applied stress are accompanied by the symbol  $\nearrow$  ( $\searrow$ ) denoting the loading (unloading) process, zones highlighted by the black circles are the newly nucleated **M bands during loading** (patterns 'a'~'e' and 'i'~'j'), the **residual A bands at the end of loading** (pattern 'f'), or the **residual M bands at the end of unloading** (patterns 'h' and 'l').

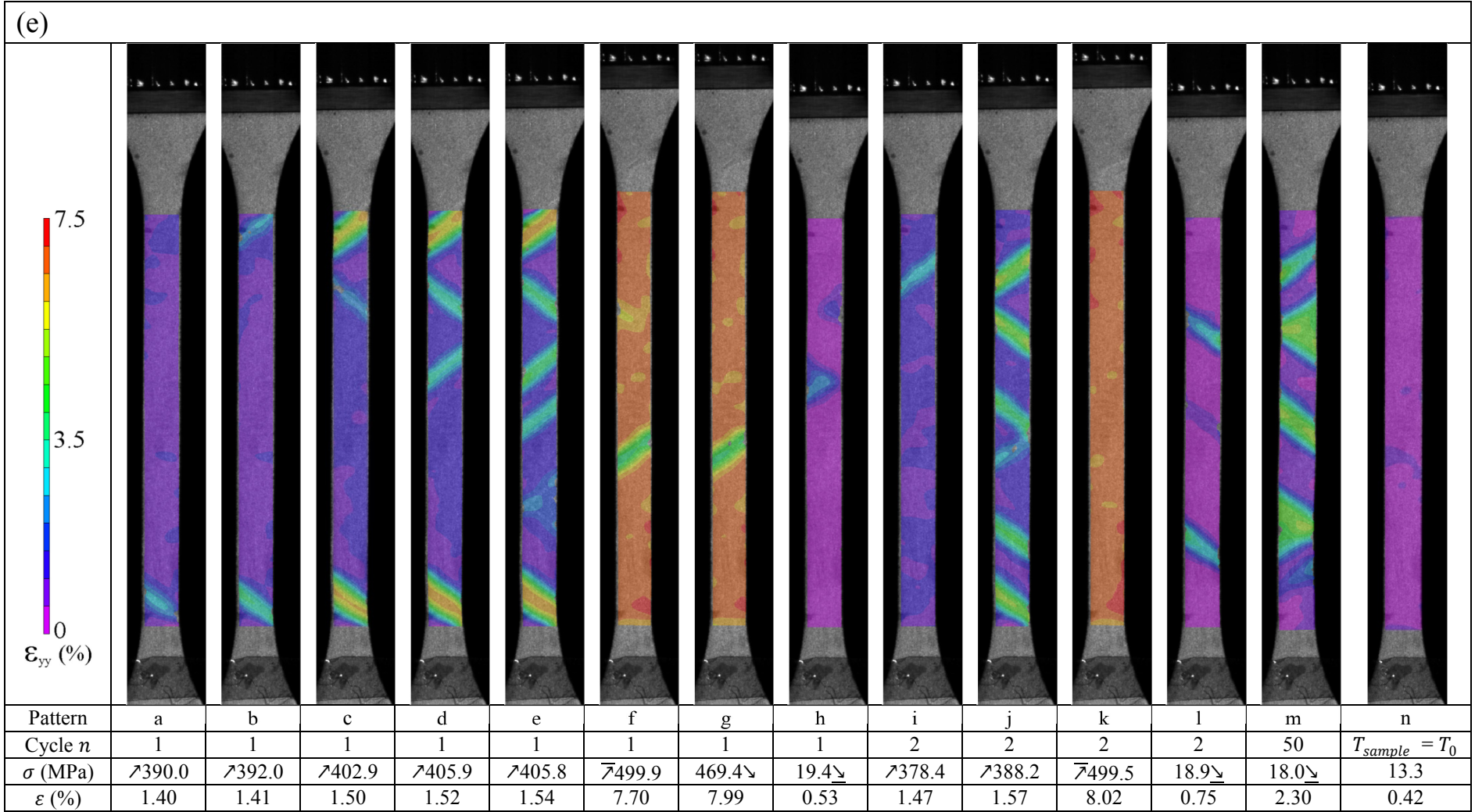


Fig. 4.2(e) The DIC full-field strain maps corresponding to the optical patterns in Fig. 4.2(d).

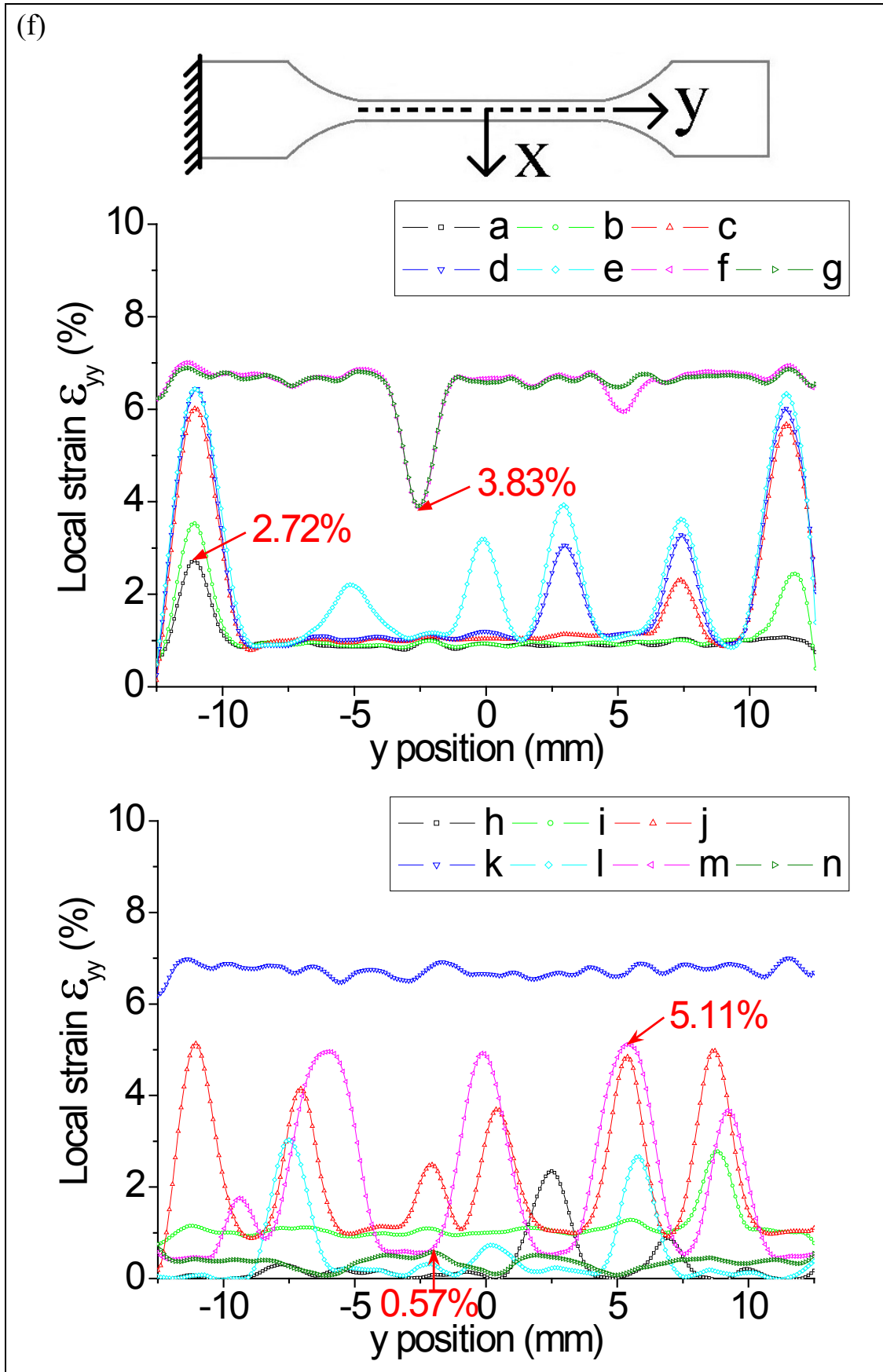


Fig. 4.2(f) The local strain profiles derived from the DIC strain maps in Fig. 4.2(e) show the strain distribution along the centerline of the specimen's gauge section.



As shown in Fig. 4.2(a), Specimen *T* had an evident mechanical shakedown during the 50 stress-controlled tensile cycles under  $\sigma_{max} = 500$  MPa and  $f = 0.01$  Hz. The evolutions of the cycle features (cycle-minimum nominal strain  $\varepsilon_{min}$ , cycle-maximum nominal strain  $\varepsilon_{max}$ , nominal strain change  $\Delta\varepsilon = \varepsilon_{max} - \varepsilon_{min}$ , and mechanical energy-dissipation density  $D$  (stress-strain hysteresis-loop area)) are shown in Figs. 4.2(b) and 4.2(c). Typical patterns of the Lüders-like band observation are displayed in Fig. 4.2(d), with the corresponding testing conditions (cycle number  $n$ , applied nominal stress  $\sigma$ , and nominal strain  $\varepsilon$ ) indicated below each image. Moreover, the DIC full-field strain maps corresponding to the optical observed patterns are shown in Fig. 4.2(e), and the local strain profiles along the centerline of the specimen's gauge section are plotted in Fig. 4.2(f) which quantifies the strain distribution and evolution during the stress-controlled cyclic test. In the 1<sup>st</sup> cycle, 7 Martensite (M) macro bands (Lüders-like bands containing grains mostly transformed to the stress-induced Martensite) nucleated subsequently (see patterns 'a'~'e' in Figs. 4.2(d)-(f)) during the forward A→M phase transformation. At the end of the loading (i.e., when the applied stress increased to  $\sigma_{max} = 500$  MPa), there were two Austenite (A) bands remaining untransformed (pattern 'f'). One of these two bands disappeared at the beginning of the unloading as shown in the pattern 'g' due to the crosshead's inertia, so the strain  $\varepsilon$  slightly increased. During the unloading process, the reverse M→A phase transformation progressed with the shrinkage of M bands and the nucleation of A bands. Two thin crossed M bands were left at the end of the unloading (pattern 'h') and disappeared at the beginning of the 2<sup>nd</sup> cycle. It is seen that the band evolution of the 2<sup>nd</sup> cycle was different from that of the 1<sup>st</sup> cycle: the location of the 1<sup>st</sup> band changed (comparing patterns 'a' and 'i') and the total band number decreased from 7 to 6 (comparing patterns 'e' and 'j'). Moreover, the A→M phase

transformation of the specimen's gauge section was fully finished at the loading end of the 2<sup>nd</sup> cycle leading to a larger  $\varepsilon_{max}$  (comparing patterns 'f' and 'k') and more residual M bands were observed at the unloading end of the 2<sup>nd</sup> cycle (comparing patterns 'h' and 'l').

The variations of the nominal strains, namely, the increases of  $\varepsilon_{min}$  and  $\varepsilon_{max}$  and the decrease of  $\Delta\varepsilon (= \varepsilon_{max} - \varepsilon_{min})$  are more noticeable in the first 15 cycles (see Fig. 4.2(b)). The mechanical energy-dissipation density  $D$ , with some small fluctuations, rapidly decreased in the first 15 cycles and slowly decreased in the subsequent cycles. At the unloading end of the 50<sup>th</sup> cycle, the residual M bands accumulated to a considerable amount (pattern 'm' in Figs. 4.2(d)-(f)) so that  $\varepsilon_{min}$  (apparent residual strain) increased to 2.30% (see the mark 'm' in Fig. 4.2(a)); however, when the specimen's temperature returned to the room temperature after stopping the cyclic test, all the residual M bands disappeared (pattern 'n' in Figs. 4.2(d) and 4.2(e)) and  $\varepsilon_{min}$  decreased to 0.42% (see the highlighted mark 'n' in Fig. 4.2(a)). So, among the large apparent residual strain during this stress-controlled cyclic test, only minor part (0.42%) is the permanent/irrecoverable strain caused by dislocations and/or the "locked-in" residual Martensite, while the major part (1.88% = 2.30% – 0.42%) is due to the "thermo-stabilized Martensite" and recoverable. That means the apparent residual strain ( $\varepsilon_{min}$ ) measured from the cyclic stress-strain response curves should not be simply taken as the result of the fatigue damage.

The DIC strain maps in Fig. 4.2(e) not only show the band-pattern evolution, but also quantify the strain distribution (such as Fig. 4.2(f)) which is consistent with the previous studies by other research groups [34, 58, 101]: the local strain inside the Lüders-like bands (i.e., Martensite domain) didn't saturate when they nucleated — the high-strain domain of profile 'a' in Fig. 4.2(f) only has a value of 2.72%; similarly, the



local strain in the “Austenite” band (low-strain domain) can be as large as 3.83% (see profile ‘f’) when the size of the A band is small (i.e., when its evolution is close to annihilation/nucleation). It is also verified by the DIC results in Fig. 4.2(f) that there is a large amount of “thermo-stabilized M” residual bands during the cyclic loading which recovers when the test is stopped (comparing the profile ‘m’ with local strain peaks of 5.11% and the profile ‘n’ with the local maximum residual/irrecoverable strain of 0.57%).

#### 4.2.2 Fatigue tests with a high stress level ( $\sigma_{max} = 500$ MPa)

##### 4.2.2.1 Low frequency ( $f = 0.01$ Hz)

The loading conditions of Specimen  $A_{500}^{0.01}$  (Fig. 4.3) are the same as those of Specimen  $T$  (Fig. 4.2), except that the cyclic loading on Specimen  $A_{500}^{0.01}$  continued until the specimen’s fatigue failure. In Fig. 4.3(b), with increasing the cycle number  $n$ ,  $\varepsilon_{max}$  rapidly reached stabilization while  $\varepsilon_{min}$  and  $\Delta\varepsilon$  largely varied in the first 50 cycles (so-called “transient stage” which contains the cycles from the beginning of the fatigue test to the stabilization of the cycle features) and slightly changed in the subsequent cycles (so-called “steady-state” cycles); the fatigue life  $N_f$  is defined as the total number of cycles up to the fatigue failure. The mechanical energy-dissipation density  $D$  shown in Fig. 4.3(c) had a similar evolution trend as  $\Delta\varepsilon$  in Fig. 4.3(b). In the “transient stage”,  $\varepsilon_{min}$  increased to a large value (see the mark ‘d’ in Fig. 4.3(a)) mainly due to the accumulated residual M bands (comparing patterns ‘c’ and ‘d’ in Fig. 4.3(d)). But the band pattern slightly changed in the “steady-state” cycles (comparing pattern ‘d’ of the 50<sup>th</sup> cycle and pattern ‘f’ of the 216<sup>th</sup> cycle). The crack was slightly visible in the last complete cycle ( $n = 216$ ) but evidently observed in the failure cycle (comparing patterns ‘e’ and ‘h’ and also their magnified views in Fig.

4.3(d)); the fracture failure occurred when the applied stress increased to 461.8 MPa (pattern ‘h’). By tracing back to the previous cycles, it is found that the crack nucleation position was close to one of the macro-band fronts of the “steady-state” cycles ( $n \geq 50$ ) (see patterns ‘d’ and ‘f’).

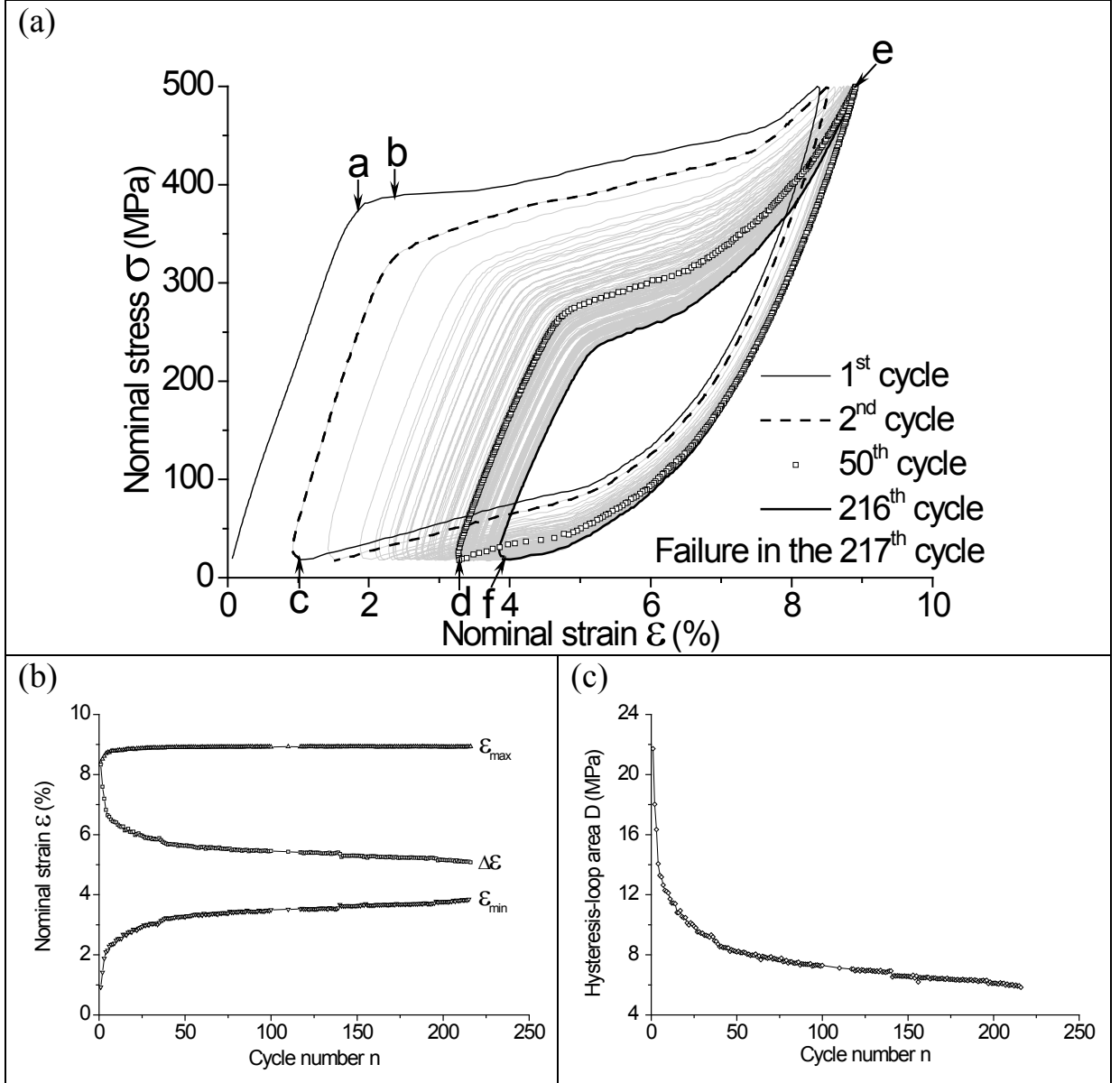


Fig. 4.3 The stress-controlled tensile fatigue test on **Specimen  $A_{500}^{0.01}$**  with  $\sigma_{max} = 500$  MPa and  $f = 0.01$  Hz: (a) the evolution of  $\sigma - \epsilon$  curve, (b) evolutions of  $\epsilon_{min}$ ,  $\epsilon_{max}$ , and  $\Delta\epsilon = \epsilon_{max} - \epsilon_{min}$ , (c) the evolution of  $D$ , and (d) the optical observation on the Lüders-like band patterns.

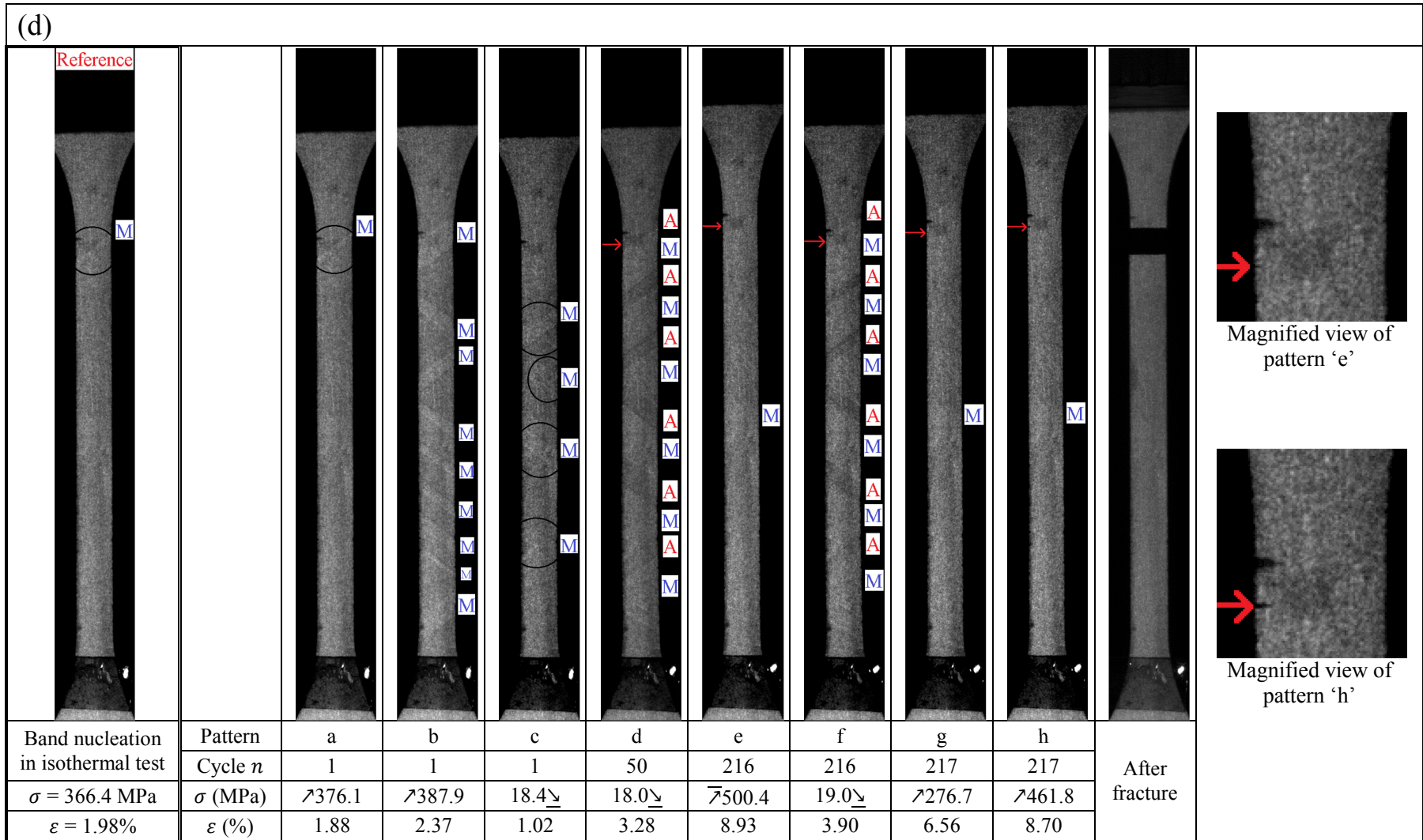


Fig. 4.3 *Continued*. (The leftmost image shows the band nucleation in the reference isothermal test; the arrows indicate the crack nucleation position.)

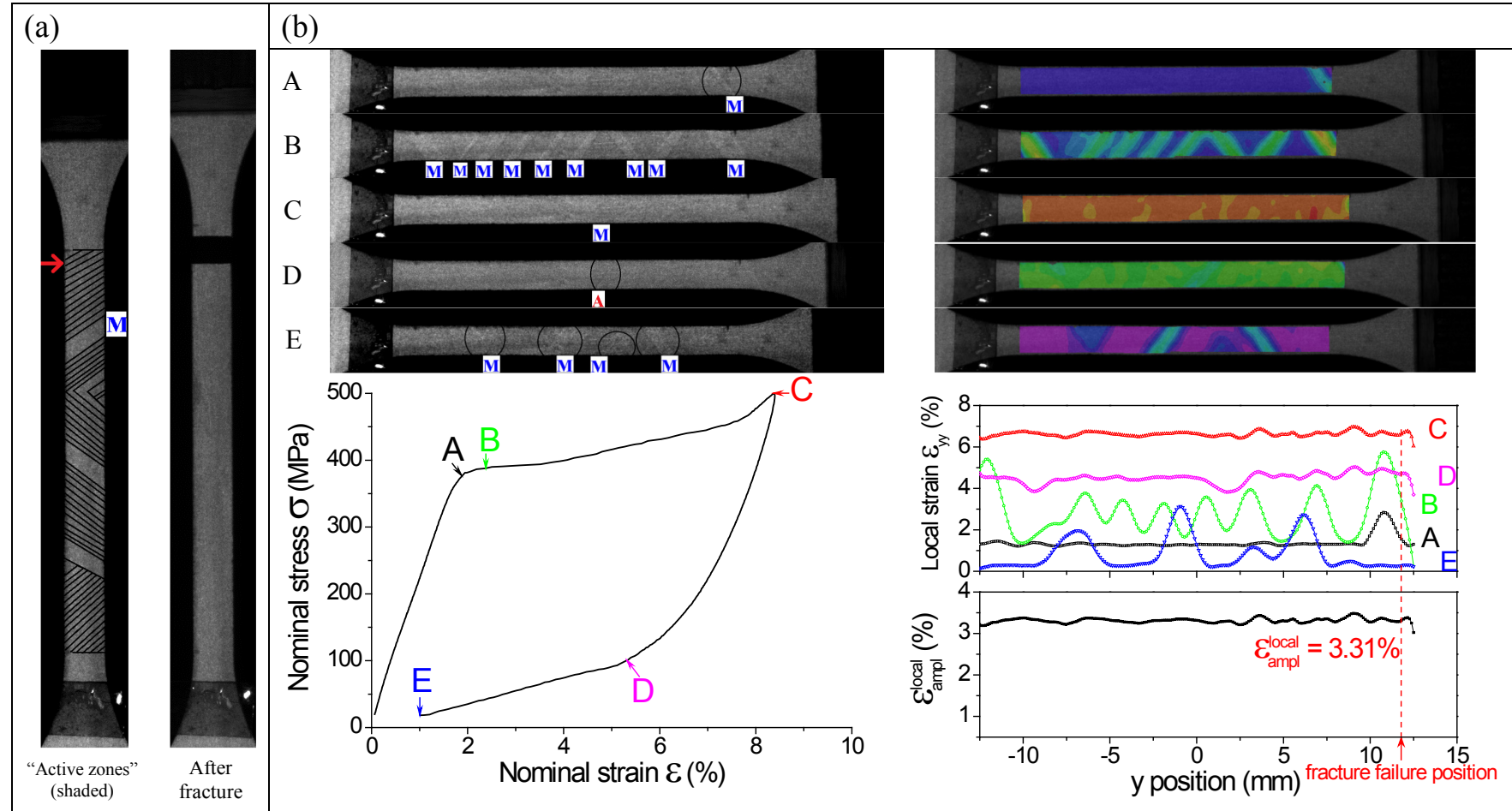


Fig. 4.4 (a) Illustration of the shaded “active zones” with  $A \leftrightarrow M$  phase transformation and the unshaded “non-active zones” with “elastic” deformation of residual **M** bands in the 1<sup>st</sup> fatigue cycle of Specimen  $A_{500}^{0.01}$  compared with an image of the specimen after fracture failure; (b) The nominal stress-strain curve, 5 optical and DIC patterns, the associated strain profiles along the centerline of specimen’s gauge section and the calculated local strain amplitude  $\epsilon_{ampl}^{local}$  in the 1<sup>st</sup> cycle.

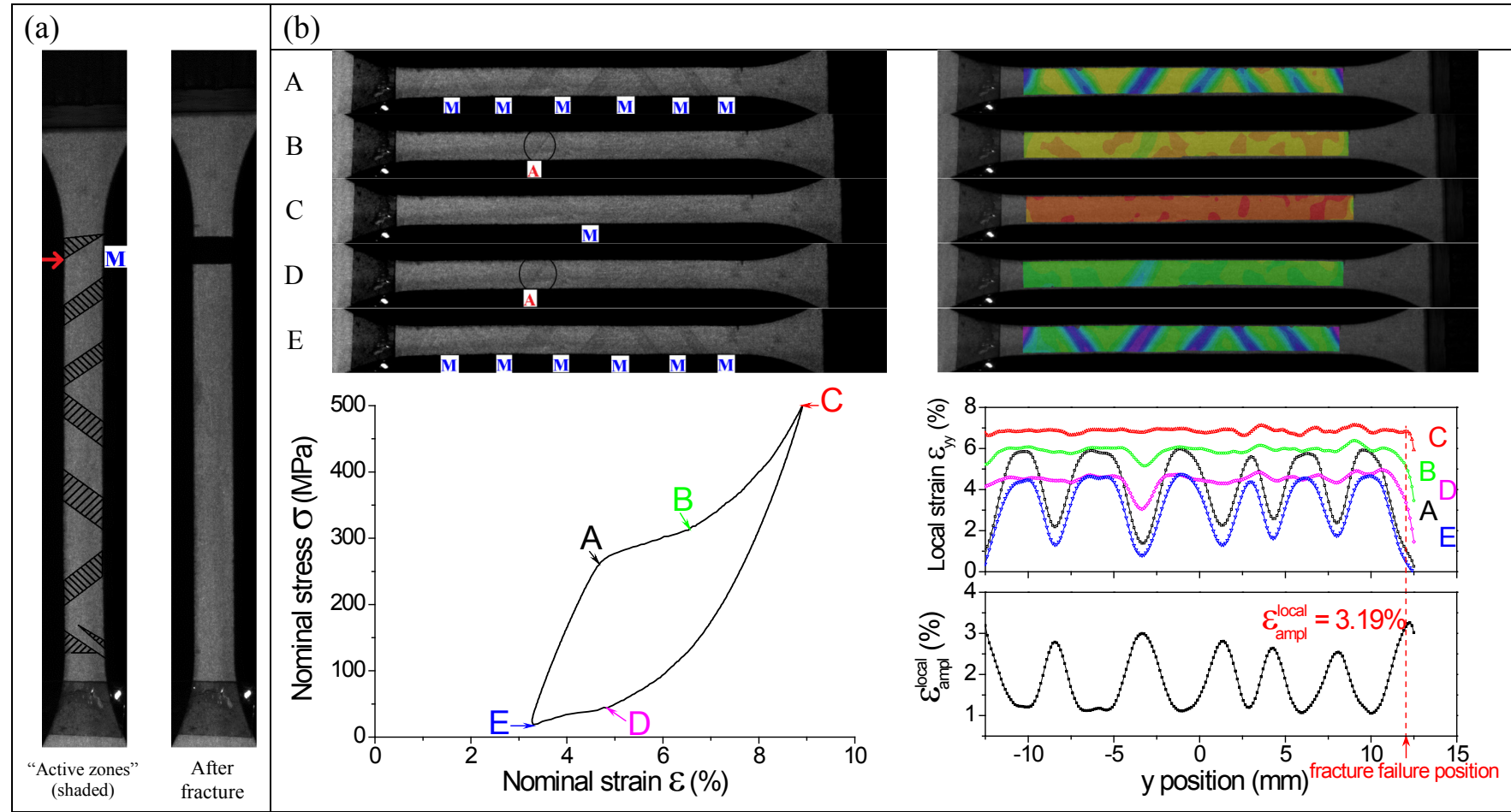


Fig. 4.5 (a) Illustration of the shaded “active zones” with  $A \leftrightarrow M$  phase transformation and the unshaded “non-active zones” with “elastic” deformation of residual M bands in the 50<sup>th</sup> fatigue cycle of Specimen  $A_{500}^{0.01}$  compared with an image of the specimen after fracture failure; (b) The nominal stress-strain curve, 5 optical and DIC patterns, the associated strain profiles along the centerline of specimen’s gauge section and the calculated local strain amplitude  $\epsilon_{ampl}^{local}$  in the 50<sup>th</sup> cycle.

It is noted in the above observation that the material points inside the residual M bands deformed “elastically” during the cyclic loading thus contributing only a little to the output strain while the material points outside the residual M bands could be swept by the moving band fronts and take the cyclic  $A \leftrightarrow M$  phase transformations with large strain changes. To illustrate the dependence of the  $A \leftrightarrow M$  transformation zones on the cycle number  $n$ , their distributions in the 1<sup>st</sup> and the 50<sup>th</sup> fatigue cycles are respectively displayed in Figs. 4.4(a) and 4.5(a) where the crack nucleation position is indicated by an arrow. The  $A \leftrightarrow M$  transformation zones are determined based on the pattern evolution in one cycle (as shown in Figs. 4.4(b) and 4.5(b)) and depicted as the shaded “**active zones**” while the unshaded “**non-active zones**” of the specimen’s gauge section are the residual M bands. In comparing Figs. 4.4(a) and 4.5(a), it is seen that the “non-active zones” (the residual M bands) largely increased with increasing  $n$  from 1 to 50 while the “active zones” of cyclic  $A \leftrightarrow M$  transformation consequently reduced. The crack nucleation position was in one of the “active zones” of the 1<sup>st</sup> cycle and also the “steady-state” cycles (the 50<sup>th</sup> cycle can be taken as the beginning of the “steady-state” cycles).

With the DIC strain measurement, the cyclic variation of local strains can be quantified as shown in Fig. 4.4(b) and Fig. 4.5(b) for the 1<sup>st</sup> and the 50<sup>th</sup> cycles, respectively. In the 1<sup>st</sup> cycle, all the material points in the specimen have zero strain at the beginning (i.e., cycle-minimal strain is zero), while they have maximum strains at the end of the loading (fully transformed to M phase as shown in the local strain profile “C” in Fig. 4.4(b)); then the local strain oscillation amplitude ( $\varepsilon_{ampl}^{local} = \frac{\varepsilon_{max}^{local} - \varepsilon_{min}^{local}}{2}$ ) of the 1<sup>st</sup> cycle can be determined, which is almost the same for all the material points in the specimen ( $\varepsilon_{ampl}^{local}$  is around 3.31%). However, in the 50<sup>th</sup> cycle

(taken as a “steady-state” cycle), the local strain amplitudes significantly depend on the position due to the specimen’s inhomogeneous deformation (with Lüders-like band evolution);  $\varepsilon_{ampl}^{local}$  at the fatigue failure position is 3.19% which is a strain peak (a local maximum as shown in Fig. 4.5(b)) — i.e., the failure occurs at the “active zone” with high strain variation (due to the cyclic phase transformation).

#### 4.2.2.2 Medium frequency ( $f = 0.1$ Hz)

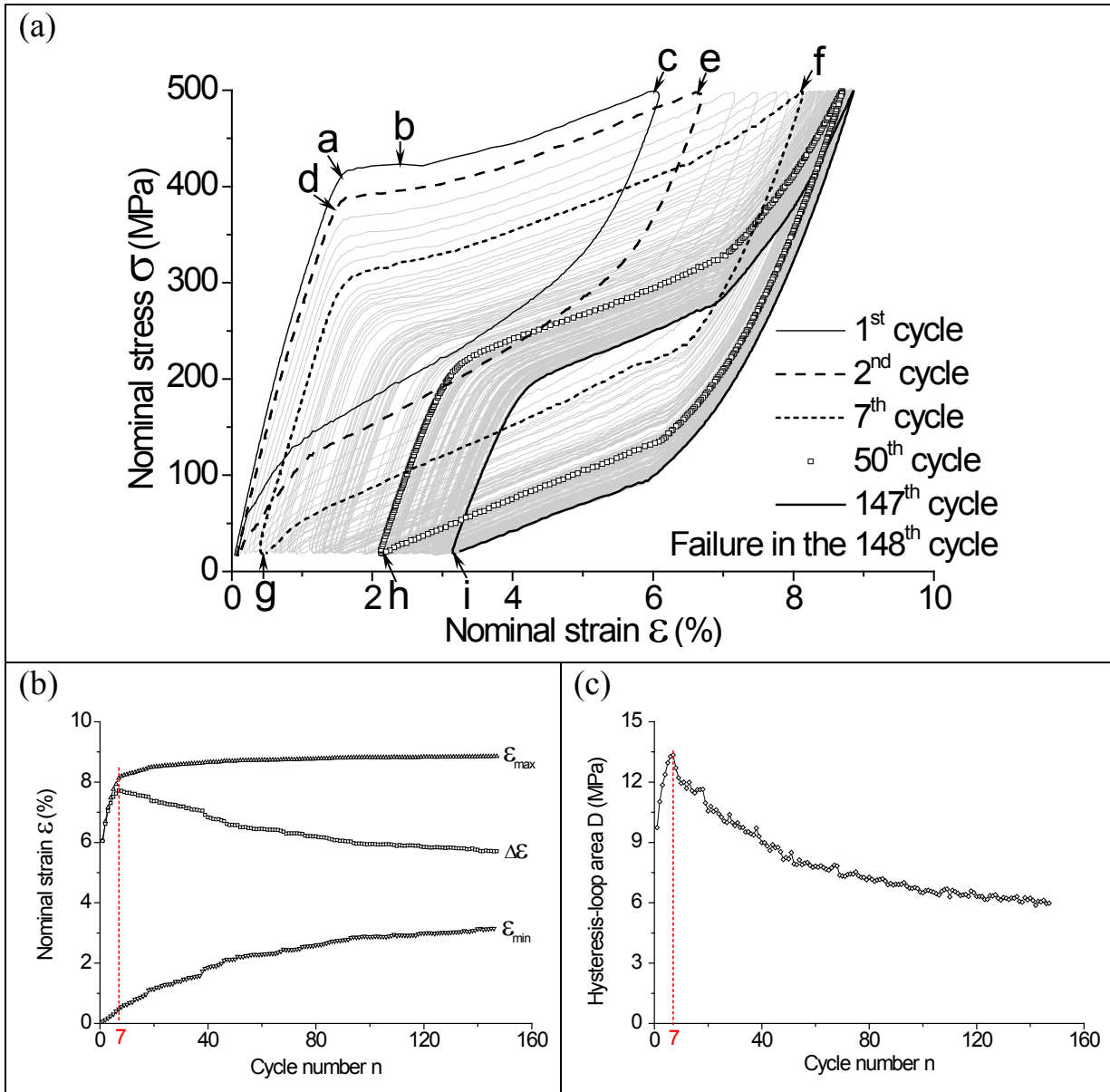


Fig. 4.6 The stress-controlled tensile fatigue test on **Specimen  $A_{500}^{0.1}$**  with  $\sigma_{max} = 500$  MPa and  $f = 0.1$  Hz: (a) the evolution of  $\sigma - \varepsilon$  curve, (b) evolutions of  $\varepsilon_{min}$ ,  $\varepsilon_{max}$ , and  $\Delta\varepsilon = \varepsilon_{max} - \varepsilon_{min}$ , (c) the evolution of  $D$ , and (d) the optical observation on the Lüders-like band patterns.



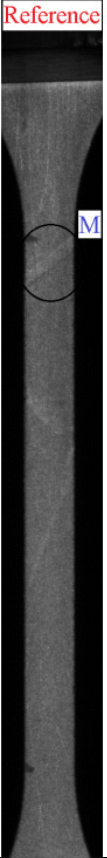
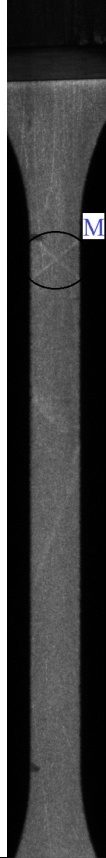
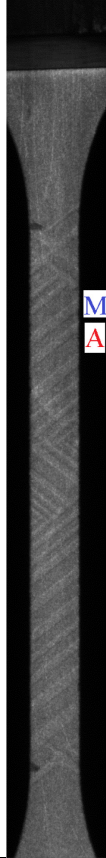
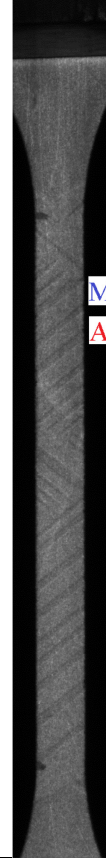
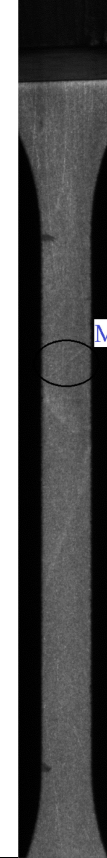
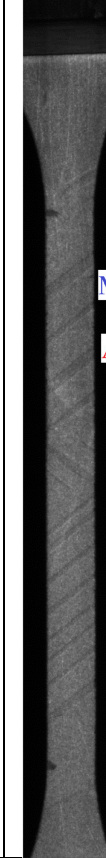
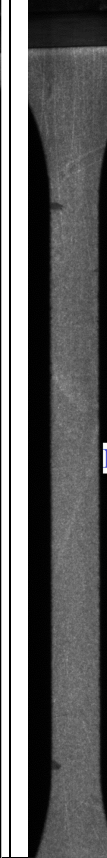
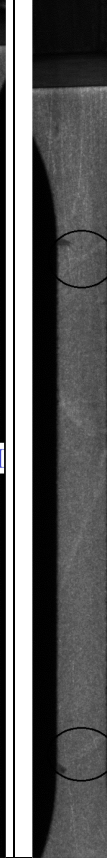
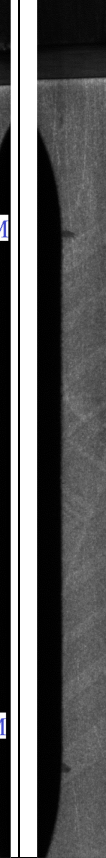
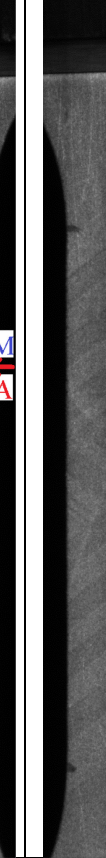
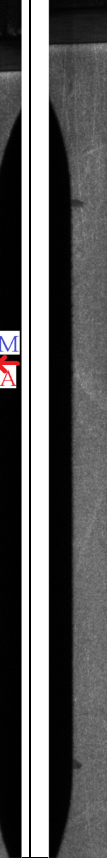
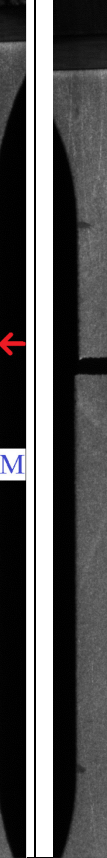
(d)												
	Reference											
												
Band nucleation in isothermal test	Pattern	a	b	c	d	e	f	g	h	i	j	After fracture
	Cycle $n$	1	1	1	2	2	7	7	50	147	148	
$\sigma = 386.2 \text{ MPa}$	$\sigma \text{ (MPa)}$	409.3	423.3	499.1	379.1	497.8	500.0	19.0	20.5	19.7	498.0	
$\varepsilon = 1.53\%$	$\varepsilon \text{ (%)}$	1.56	2.40	6.02	1.51	6.64	8.11	0.49	2.13	3.16	8.87	

Fig. 4.6 *Continued*. (The leftmost image shows the band nucleation in the reference isothermal test; the arrows indicate the crack nucleation position.)



In the 1<sup>st</sup> cycle, two crossed M bands (see pattern ‘a’ in Fig. 4.6(d)) first nucleated near the upper end of the gauge section and more bands nucleated subsequently, finally resulting in about 30 macro bands coexisting (pattern ‘b’). The total band number (30) is much larger than that at low frequency of  $f = 0.01$  Hz (9 M bands, pattern ‘b’ in Fig. 4.3(d)), which is consistent with the previous observation by [60, 68]. Afterwards, the band fronts propagated and the M bands grew; but the A→M phase transformation of the gauge section was only partially finished as there remained many A bands in the gauge section at the loading end (pattern ‘c’). During the unloading process, all the M bands transformed back to the parent phase (A phase) at the unloading end. In the 2<sup>nd</sup> cycle, the 1<sup>st</sup> M band nucleated in a different location at a smaller stress value (comparing patterns ‘a’ and ‘d’). Due to this decrease of the band-nucleation stress, the stress-induced M bands at the loading end increased (comparing patterns ‘c’ and ‘e’). With the increase of  $n$ , the  $\sigma - \varepsilon$  curve largely shifted downwards and rightwards (see Fig. 4.6(a)); in the 7<sup>th</sup> cycle, the A→M phase transformation of the gauge section was completely finished at the loading end (pattern ‘f’) and two residual M bands were observed at the unloading end (pattern ‘g’). All the cycle features ( $\varepsilon_{min}$ ,  $\varepsilon_{max}$ ,  $\Delta\varepsilon$ , and  $D$  in Figs. 4.6(b) and 4.6(c)) increased with increasing  $n$  from 1 to 7. Afterwards,  $\varepsilon_{max}$  tended to saturate since the complete A→M phase transformation of the gauge section was attained while  $\varepsilon_{min}$  continued to increase, consistent with the enlarging residual M bands (comparing patterns ‘h’ and ‘i’ at the unloading end of the 50<sup>th</sup> cycle and the 147<sup>th</sup> cycle); both  $\Delta\varepsilon$  and  $D$  decreased with increasing  $n$  (when  $n > 7$ ). The fatigue failure crack wasn’t visible until the final cycle ( $N_f = 148$ ) and this crack quickly grew then led to the fracture failure when the gauge section was completely transformed to Martensite (pattern ‘j’).

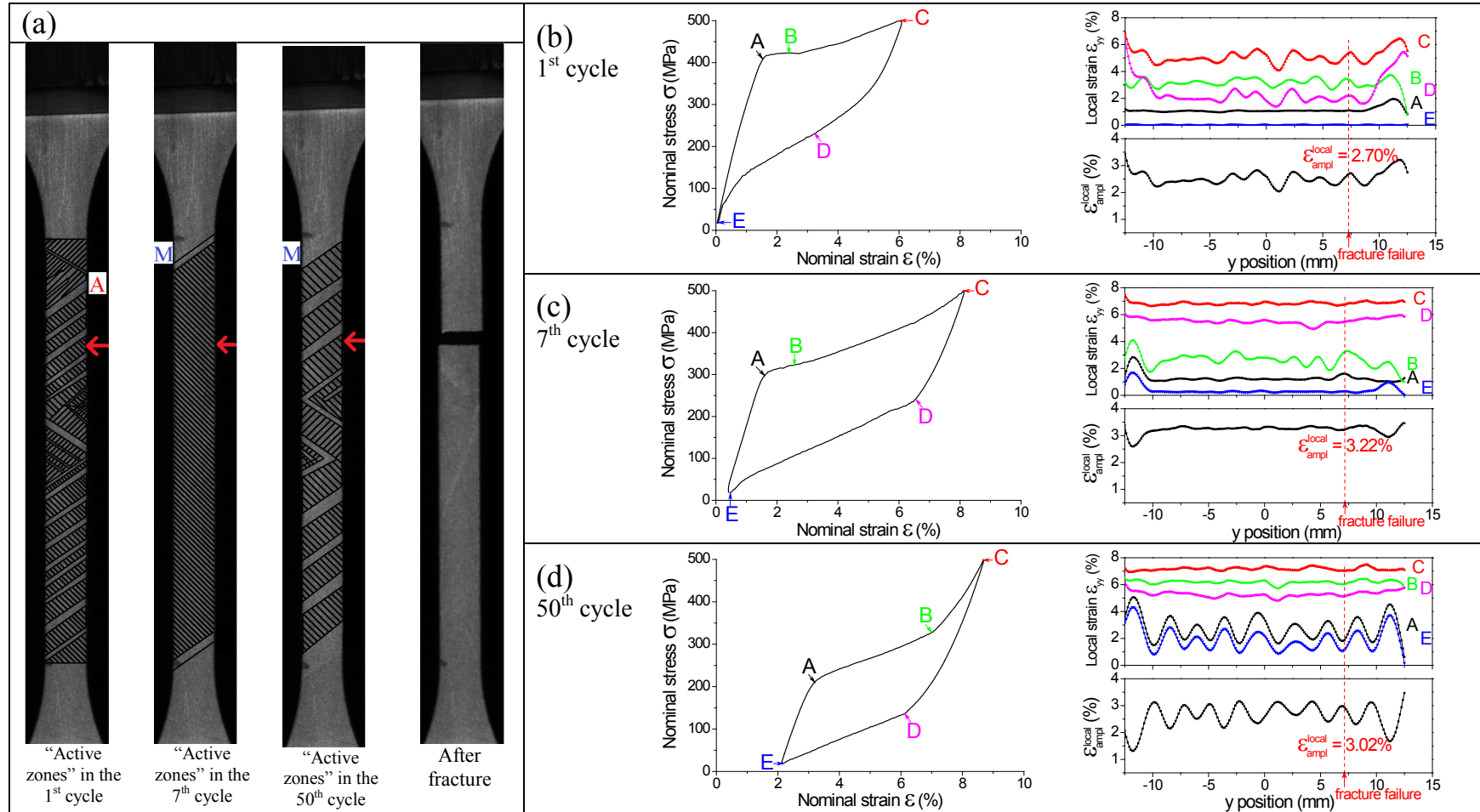


Fig. 4.7 (a) Comparison of the “active zones” (shaded zones) and the “non-active zones” (residual A or residual M bands) in the 1<sup>st</sup> cycle, the 7<sup>th</sup> cycle, and the 50<sup>th</sup> fatigue cycle of Specimen  $A_{500}^{0.1}$ ; The nominal  $\sigma - \epsilon$  curves, the typical strain profiles and the calculated local strain amplitudes  $\epsilon_{ampl}^{local}$  in the 1<sup>st</sup> cycle (b), in the 7<sup>th</sup> cycle (c) and in the 50<sup>th</sup> cycle (d).

In order to understand the non-monotonic trends of the cycle features  $\Delta\varepsilon$  and  $D$  (reaching the peak values in the 7<sup>th</sup> fatigue cycle as shown in Figs. 4.6(b) and 4.6(c)), the “active zones” (cyclic A $\leftrightarrow$ M transformation zones) of the 7<sup>th</sup> cycle are compared with those of the 1<sup>st</sup> cycle and the 50<sup>th</sup> cycle in Fig. 4.7(a). It is seen that, when the cycle number  $n$  increases from 1 to 7, the shaded “active zones” enlarge and the unshaded “non-active zones” change from the residual A to residual M; from the 7<sup>th</sup> cycle to the “steady-state” cycles ( $n \geq 50$ ), the “active zones” reduce while the “non-active zones” of the residual M bands increase. So, in the specimen under the cyclic loading, there always exist some “non-active zones” only taking the “elastic” deformation of the A phase or/and the M phase; moreover, the evolution of the “active zones” is consistent with that of the nominal strain change  $\Delta\varepsilon$  (see Fig. 4.6(b)) — the volume of “active zones” reaches the maximum value in the 7<sup>th</sup> cycle where  $\Delta\varepsilon$  also reaches the peak value. And the nucleation position of the fatigue failure crack was always in one of the “active zones” as indicated by the arrow in Fig. 4.7(a). Corresponding to the non-monotonic changes in the “active-zone” volume and the nominal strain change  $\Delta\varepsilon$  for the 1<sup>st</sup>, 7<sup>th</sup>, and 50<sup>th</sup> cycles, the local strain amplitude ( $\varepsilon_{ampl}^{local}$ ) at the failure position changes non-monotonically as shown in Figs. 4.7(b)-(d) where  $\varepsilon_{ampl}^{local}$  increases from 2.70% to 3.22%, then decreases to 3.02% at the “steady-state” cycle (the 50<sup>th</sup> cycle). Similar to the low-frequency case ( $f = 0.01$  Hz), the fatigue failure occurs at one of the  $\varepsilon_{ampl}^{local}$  peaks of the “steady-state” cycle — i.e., the failure occurs at the “active zone” with the cyclic phase transformation. But the strain-amplitude difference between the “active zones” and the “non-active zones” (or the strain difference between the high-strain domains and the low-strain domains) in current test ( $f = 0.1$  Hz) is smaller than that in the low-frequency case ( $f = 0.01$  Hz) because more bands formed in current test, leading to narrower/slimmer bands which

didn't fully develop into high-strain domains (M-phase domains). In other words, the specimen's deformation at the medium frequency is more homogeneous than that at the low frequency, which agrees with the recent study [101].

#### 4.2.2.3 High frequency ( $f = 1$ Hz)

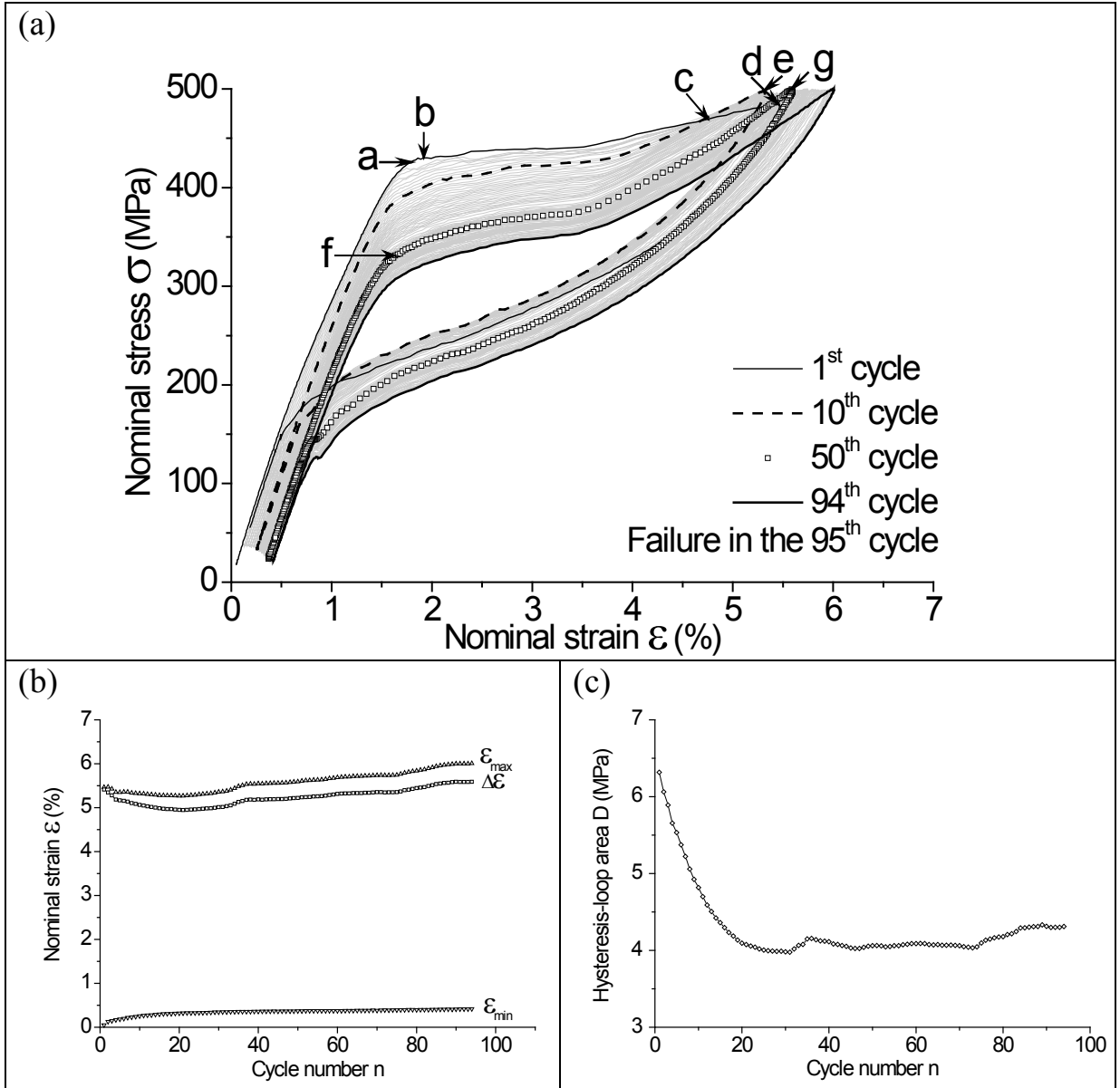


Fig. 4.8 The stress-controlled tensile fatigue test on Specimen  $A_{500}^1$  with  $\sigma_{max} = 500$  MPa and  $f = 1$  Hz: (a) the evolution of  $\sigma - \epsilon$  curve, (b) evolutions of  $\epsilon_{min}$ ,  $\epsilon_{max}$ , and  $\Delta\epsilon = \epsilon_{max} - \epsilon_{min}$ , (c) the evolution of  $D$ , and (d) the optical observation on the Lüders-like band patterns. Note: due to the limitation of the testing machine the applied maximum stress wasn't attained until the 10th cycle.

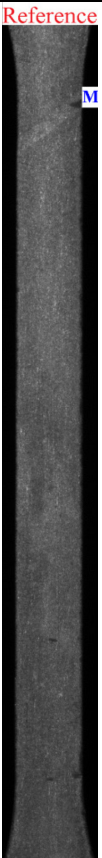
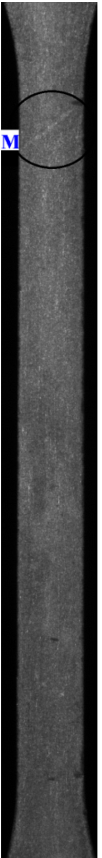
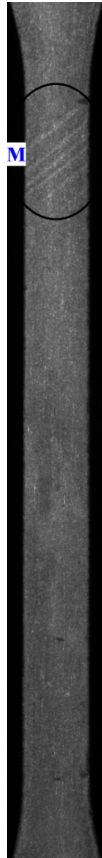
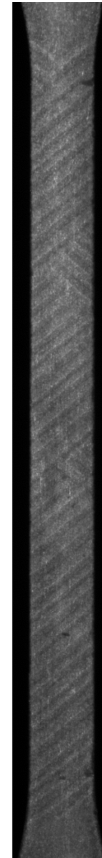
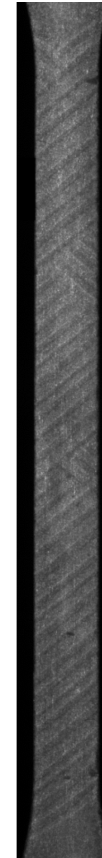
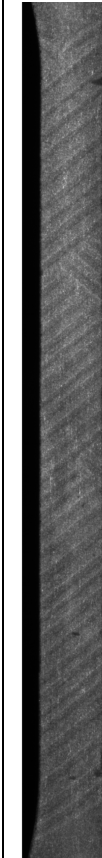
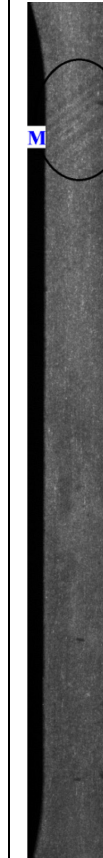
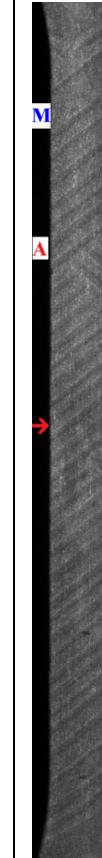
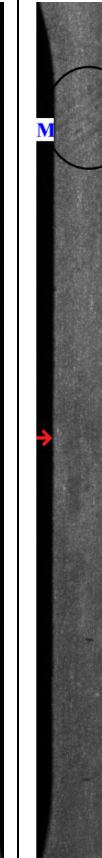
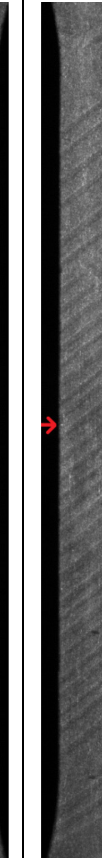
(d)											
Reference											
Band nucleation in isothermal test	Pattern	a	b	c	d	e	f	g	h	i	After fracture
	Cycle $n$	1	1	1	1	10	50	50	95	95	
$\sigma = 385.5 \text{ MPa}$	$\sigma \text{ (MPa)}$	425.8	430.1	449.2	484.5	498.1	330.9	499.5	302.3	498.9	
$\varepsilon = 1.61\%$	$\varepsilon \text{ (%)}$	1.79	1.92	4.75	5.45	5.30	1.64	5.59	1.59	6.01	

Fig. 4.8 *Continued.* (The leftmost image shows the band nucleation in the reference isothermal test; the arrows indicate the crack nucleation position.)

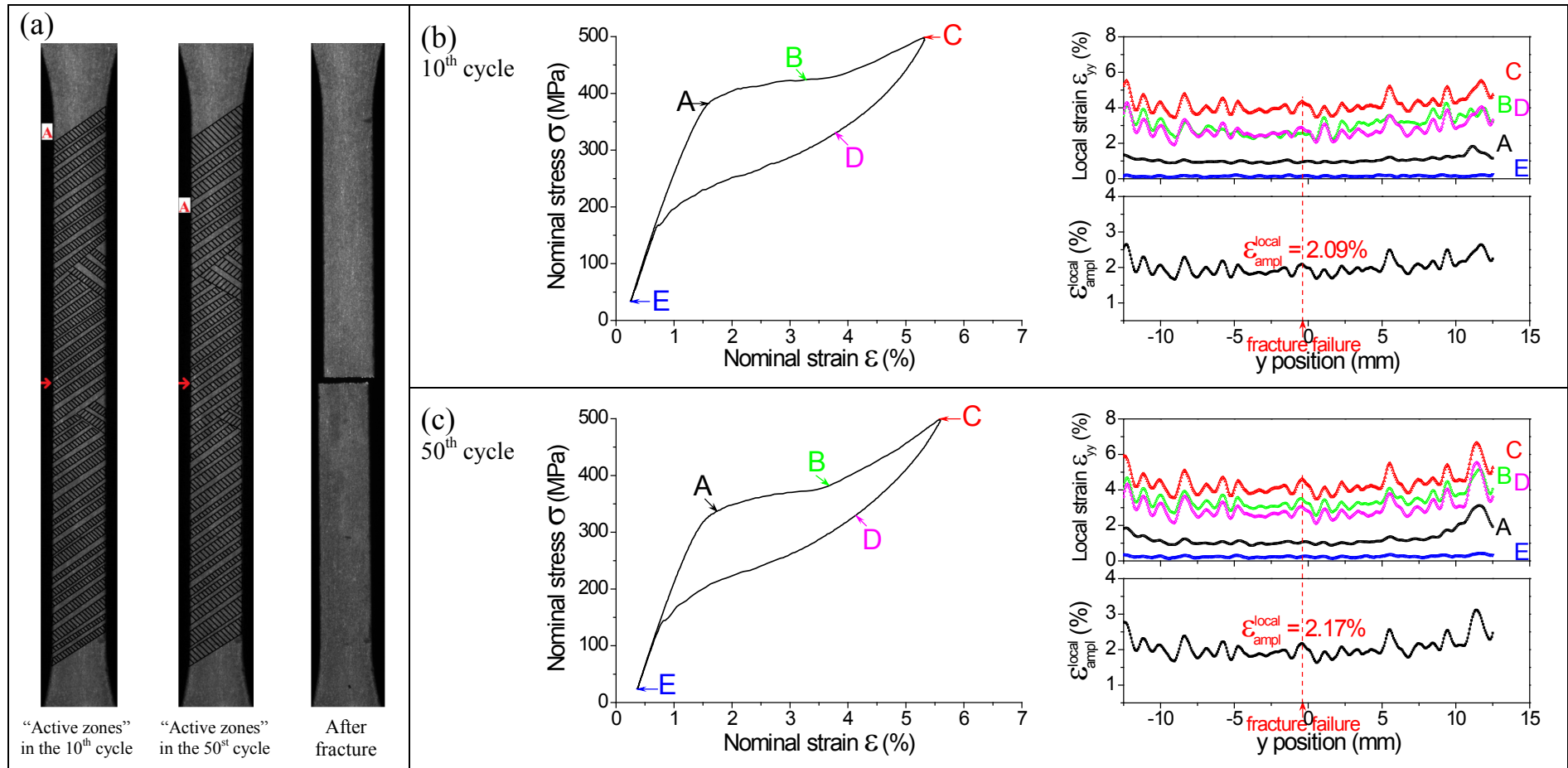


Fig. 4.9 (a) Comparison of the “active zones” (shaded zones) and the “non-active zones” (**residual A bands**) in the 10<sup>th</sup> cycle and the 50<sup>th</sup> fatigue cycle of **Specimen A<sub>500</sub><sup>1</sup>**; The nominal  $\sigma - \epsilon$  curves, the typical strain profiles and the calculated local strain amplitudes  $\epsilon_{ampl}^{local}$  in the 10<sup>th</sup> cycle (b) and in the 50<sup>th</sup> cycle (c).

Due to the limitation of the testing machine at the high frequency (1 Hz), the maximum applied stress reached the given stress level (500 MPa) after 10 cycles as shown by the stress-strain curves in Fig. 4.8(a). It is seen in Figs. 4.8(b) and 4.8(c) that in the final complete cycle ( $n = 94$ ), the output maximum strain  $\varepsilon_{max}$  is around 6.1%, the output minimum strain (accumulated nominal/apparent residual strain)  $\varepsilon_{min}$  is around 0.5%, and the hysteresis-loop area (mechanical energy dissipation)  $D$  is around 4.3 MPa, which are much smaller than those of the low- and medium-frequency cases. The band-pattern observation in Fig. 4.8(d) shows that, in the 1<sup>st</sup> cycle, one M band first nucleated at the same location as in the reference isothermal test (comparing the reference pattern and pattern ‘a’ in Fig. 4.8(d)) and shortly several M bands simultaneously nucleated near the first M band (pattern ‘b’); subsequently, many slim bands emerged (pattern ‘c’) and the A→M phase transformation was partially finished at the loading end (pattern ‘d’). The specimen was fully transformed back to Austenite during the unloading process. The cyclic loading-unloading scenario of the Lüders-like band patterns kept the same in the subsequent cycles till fatigue failure and the “active zones” with cyclic A↔M phase transformation enlarged a little especially at the two ends of the specimen (comparing patterns ‘e’ and ‘g’ in Fig. 4.8(d) and comparing the shaded “active zones” in the 10<sup>th</sup> cycle and the 50<sup>th</sup> cycle in Fig. 4.9(a)).

The typical DIC strain profiles and the calculated local strain amplitude ( $\varepsilon_{ampl}^{local}$ ) of the 10<sup>th</sup> and the 50<sup>th</sup> cycles are shown in Fig. 4.9(b). With the small domain spacing (i.e., many slim bands), the high-strain domains (Martensite domains) didn’t fully developed so that the specimen’s deformation is quite homogeneous with only small fluctuations as shown in the profiles ‘B’, ‘C’, and ‘D’. With the strain profiles, the local strain oscillation amplitude  $\varepsilon_{ampl}^{local}$  is determined and shows that the failure occurred in one of the  $\varepsilon_{ampl}^{local}$  peaks. It is noted that  $\varepsilon_{ampl}^{local} = 2.17\%$  at the failure

position is not the maximum one among these peaks; for example, the  $\varepsilon_{ampl}^{local}$  peaks (or the “active zones”) close to the specimen’s ends have larger values (larger strain amplitude) due to less domain-interaction (no band outside the gauge section) or lower temperature (easier for heat transfer to the clamps of the loading machine). It has been demonstrated that the specimen’s temperature under the cyclic high-frequency loading would have significant variations, which is also the reason for the formation of numerous slim bands. [13, 68, 99, 101] It is implied that, besides the local strain amplitude  $\varepsilon_{ampl}^{local}$ , the frequency (or temperature) has important effect on the material fatigue.

#### 4.2.3 Fatigue tests with a medium stress level ( $\sigma_{max} = 400$ MPa)

##### 4.2.3.1 Low frequency ( $f = 0.01$ Hz)

When a medium level stress ( $\sigma_{max} = 400$  MPa) was applied (which is slightly higher than the isothermal plateau stress for the forward phase transformation in Fig. 4.10) at  $f = 0.01$  Hz, there were only two M bands in the 1<sup>st</sup> cycle (pattern ‘b’ in Fig. 4.10(d)) and the output nominal strain was small ( $\varepsilon_{max} = 2.58\%$  of the 1<sup>st</sup> cycle in Figs. 4.10(a) and 4.10(b)). With the increase of  $n$ , the phase transformation of the gauge section progressed: 5 M bands nucleated in the 5<sup>th</sup> cycle (pattern ‘d’ in Fig. 4.10(d)) and  $\varepsilon_{max}$  increased to 3.73%; in the subsequent cycles, the number of M bands didn’t change (5 bands) but the volume of M bands increased and  $\varepsilon_{max}$  increased to 5.63% (see the mark “h” in Fig. 4.10(a)). It is seen in Figs. 4.10(b) and 4.10(c) that the cycle features  $\varepsilon_{max}$ ,  $\Delta\varepsilon$ , and  $D$  largely increased with  $n$  especially in the first 40 cycles, but  $\varepsilon_{min}$  only slightly increased before stabilization in about the 50<sup>th</sup> cycle. However, there was no exact “steady state”, because  $\varepsilon_{max}$ ,  $\Delta\varepsilon$ , and  $D$  continued to increase after 50 cycles. This feature can be also verified by the band-



pattern evolution: in the 200<sup>th</sup> cycle, the 1<sup>st</sup> band nucleated at a position different from those in the previous cycles (comparing patterns ‘a’, ‘c’, ‘e’, and ‘g’). From the 234<sup>th</sup> cycle on, the 1<sup>st</sup> band nucleated at the position where the final crack occurred (see patterns ‘i’ and ‘j’), which means that the damage in this zone reached a certain level thus making it be the specimen’s weakest zone. The crack was only visible in the failure cycle ( $N_f = 244$ , patterns ‘j’ and ‘k’).

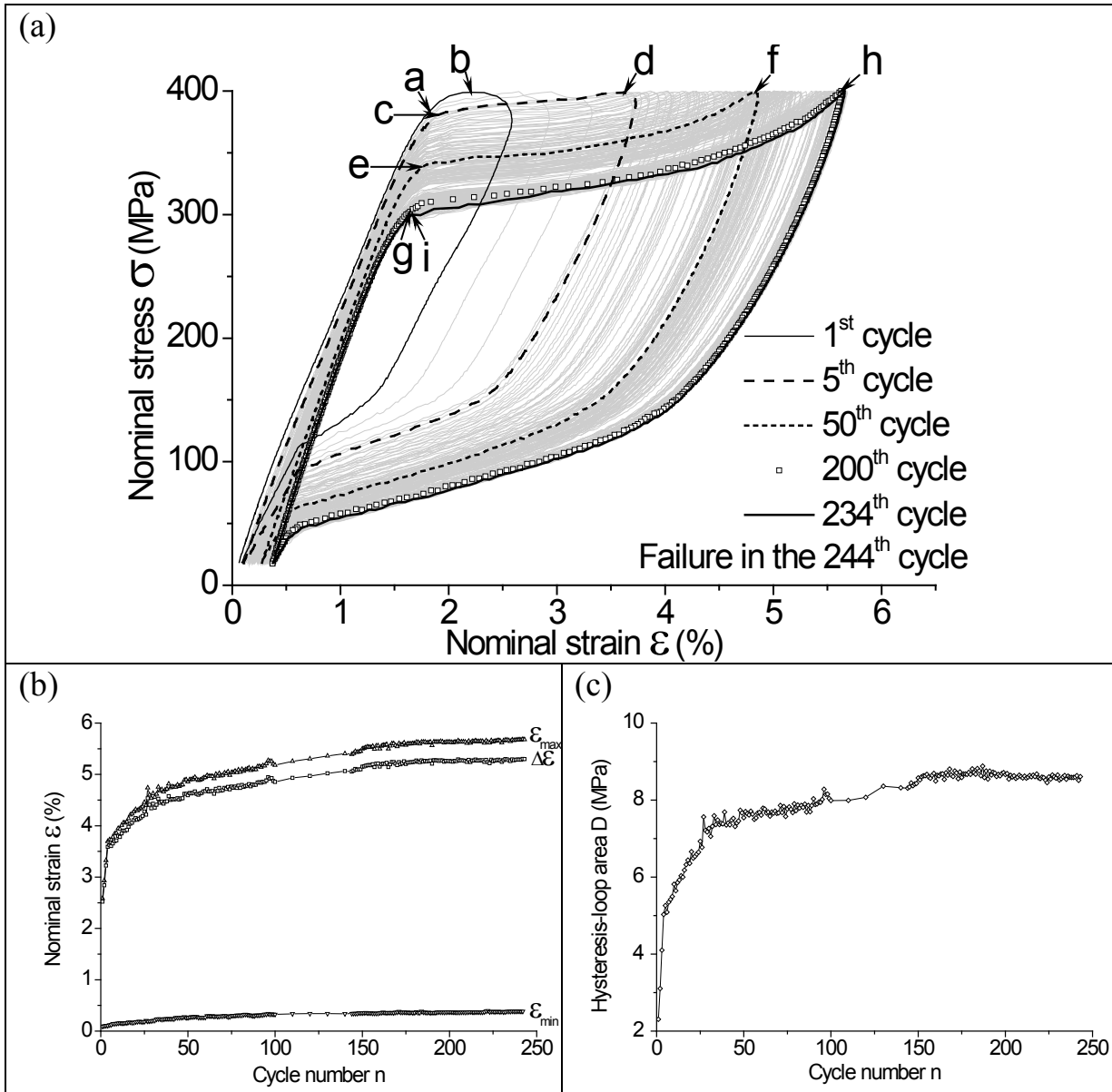


Fig. 4.10 The stress-controlled tensile fatigue test on **Specimen  $A_{400}^{0.01}$**  with  $\sigma_{max} = 400$  MPa and  $f = 0.01$  Hz; (a) the evolution of  $\sigma - \epsilon$  curve, (b) evolutions of  $\epsilon_{min}$ ,  $\epsilon_{max}$ , and  $\Delta\epsilon = \epsilon_{max} - \epsilon_{min}$ , (c) the evolution of  $D$ , and (d) the DIC strain maps demonstrating the Lüders-like band patterns.

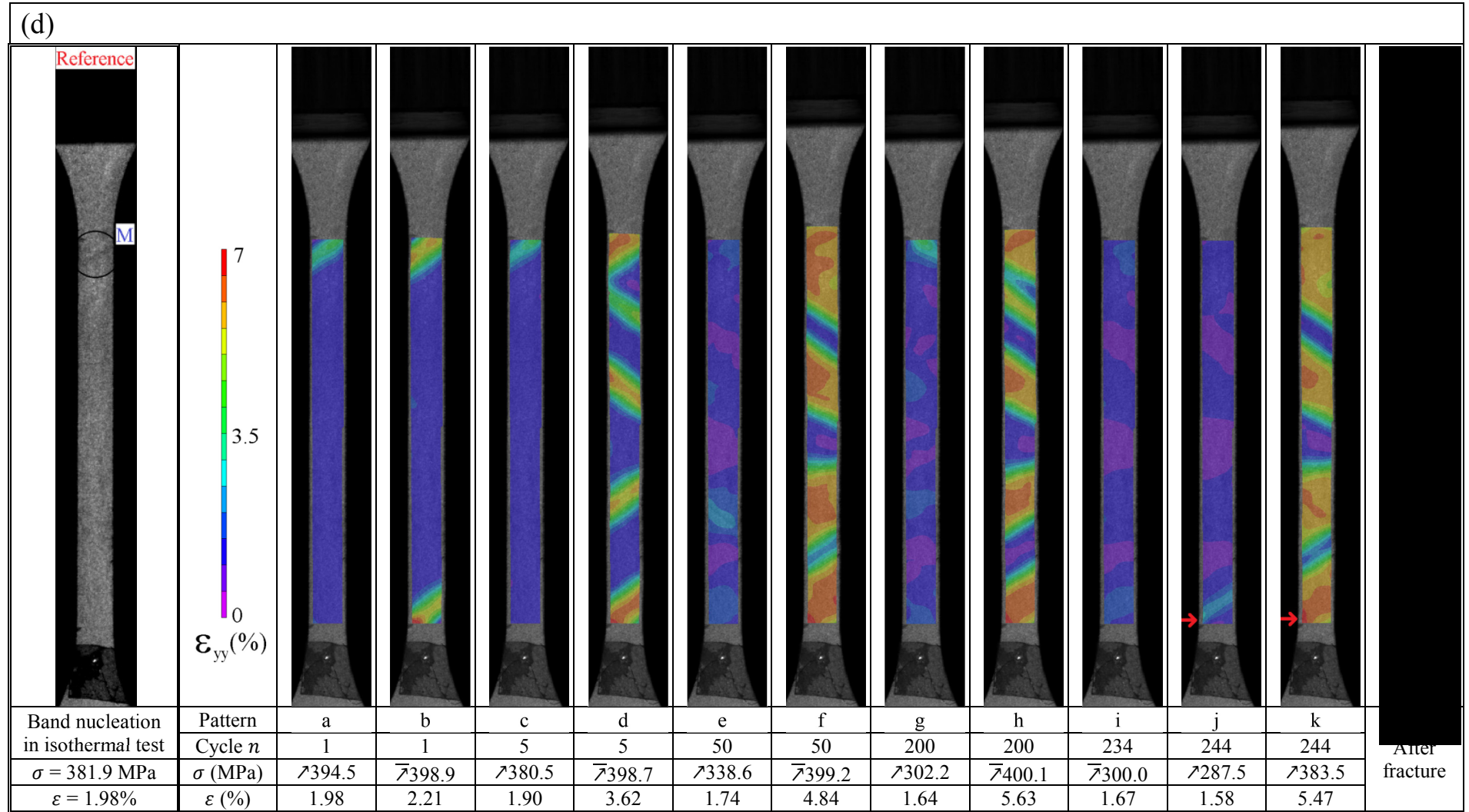


Fig. 4.10 *Continued.* (The leftmost image shows the band nucleation in the reference isothermal test; the arrows indicate the crack nucleation position.)

#### 4.2.3.2 Medium frequency ( $f = 0.1$ Hz)

When the frequency of the fatigue test increases to 0.1 Hz (e.g., Specimen  $A_{400}^{0.1}$ ), there was no band formation until the 35<sup>th</sup> cycle (see patterns ‘a’ and ‘b’ in Fig. 4.11(d)). After the 1<sup>st</sup> band nucleation, the phase transformation progressed through the front propagation and more band nucleation: the 2<sup>nd</sup> band nucleated in the 51<sup>st</sup> cycle (pattern ‘d’) and till the 200<sup>th</sup> cycle a total number of 6 M bands nucleated (pattern ‘g’). Since the 1<sup>st</sup> band nucleation in the 35<sup>th</sup> cycle, the cycle features  $\varepsilon_{max}$ ,  $\Delta\varepsilon$ , and  $D$  largely increased with  $n$  till the fatigue failure (see Figs. 4.11(b) and 4.11(c)) — no exact “steady state”. The fatigue crack nucleated in one of the “active zones” with cyclic  $A \leftrightarrow M$  transformation, leading to the fracture failure in the 260<sup>th</sup> cycle when stress increased to 395.8 MPa (patterns ‘i’ and ‘j’ in Fig. 4.11(d)).

The reason for the homogeneous deformation (without band formation) of Specimen  $A_{400}^{0.1}$  in the first 35 cycles might be the thermal effect. It was found by [34, 58, 62] that when a polycrystalline NiTi specimen takes a macroscopically uniform “elastic” deformation around 1.2% (without macro-band formation), there is already martensitic phase transformation in some grains releasing latent heat to increase the specimen’s temperature homogeneously; if the loading frequency is high enough (i.e., the released heat cannot quickly transfer to the ambient), the specimen’s temperature rise would be significant and the characteristic phase transformation stress would increase (Clausius-Clapeyron relation). That’s why an applied stress only slightly higher than the isothermal band-nucleation stress cannot always trigger the band formation (i.e., trigger a large amount of phase transformations) like the case of the first 35 cycles of Specimen  $A_{400}^{0.1}$  here. After the 35-cycles fatigue (microstructure degradation), the macroscopic phase transformation stress decreased so that the applied stress was able to trigger the band formation in the cycles of  $n > 35$ .

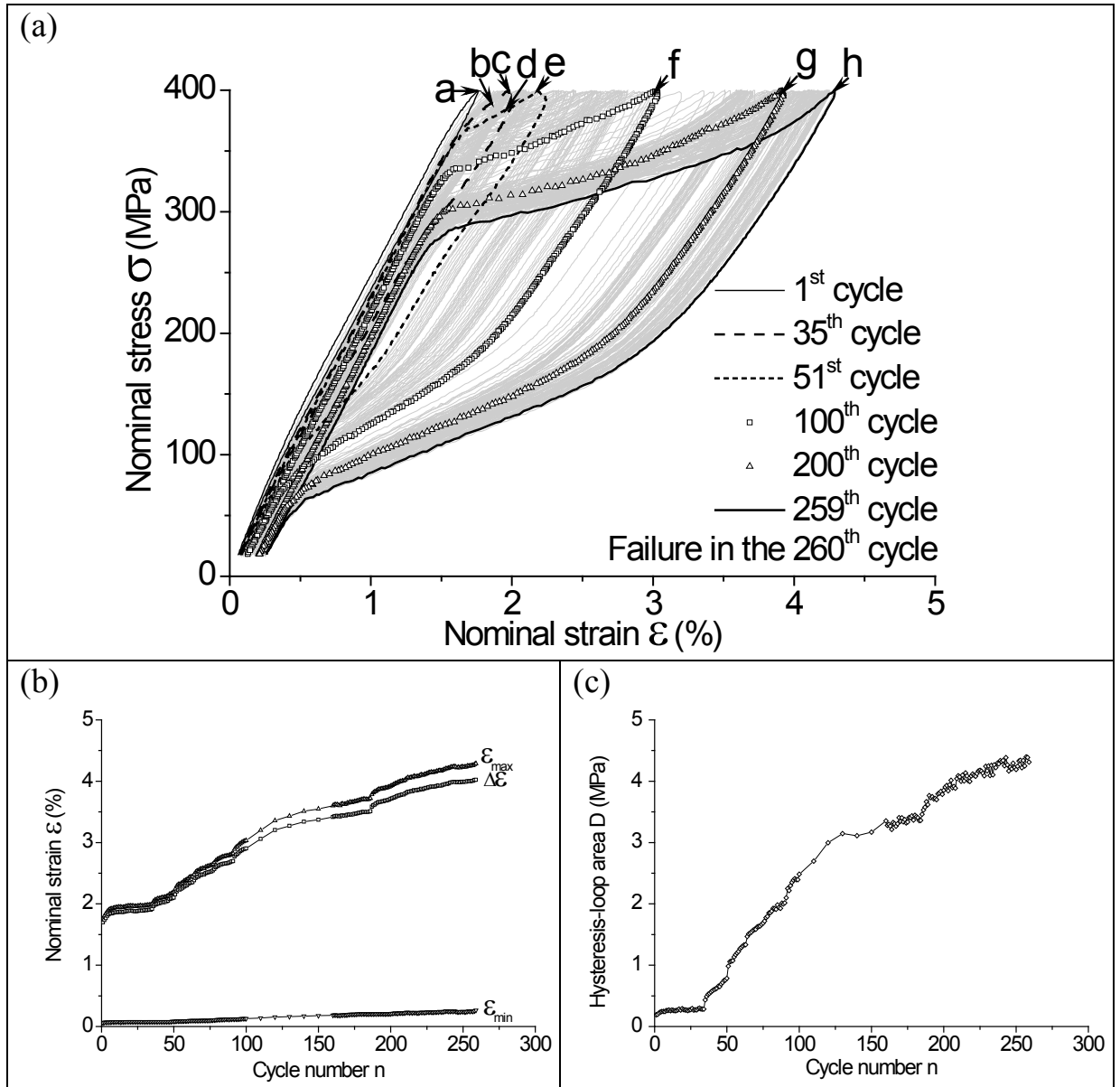


Fig. 4.11 The stress-controlled tensile fatigue test on **Specimen  $A_{400}^{0.1}$**  with  $\sigma_{max} = 400$  MPa and  $f = 0.1$  Hz: (a) the evolution of  $\sigma - \varepsilon$  curve, (b) evolutions of  $\varepsilon_{min}$ ,  $\varepsilon_{max}$ , and  $\Delta\varepsilon = \varepsilon_{max} - \varepsilon_{min}$ , (c) the evolution of  $D$ , and (d) the DIC strain maps demonstrating the Lüders-like band patterns.

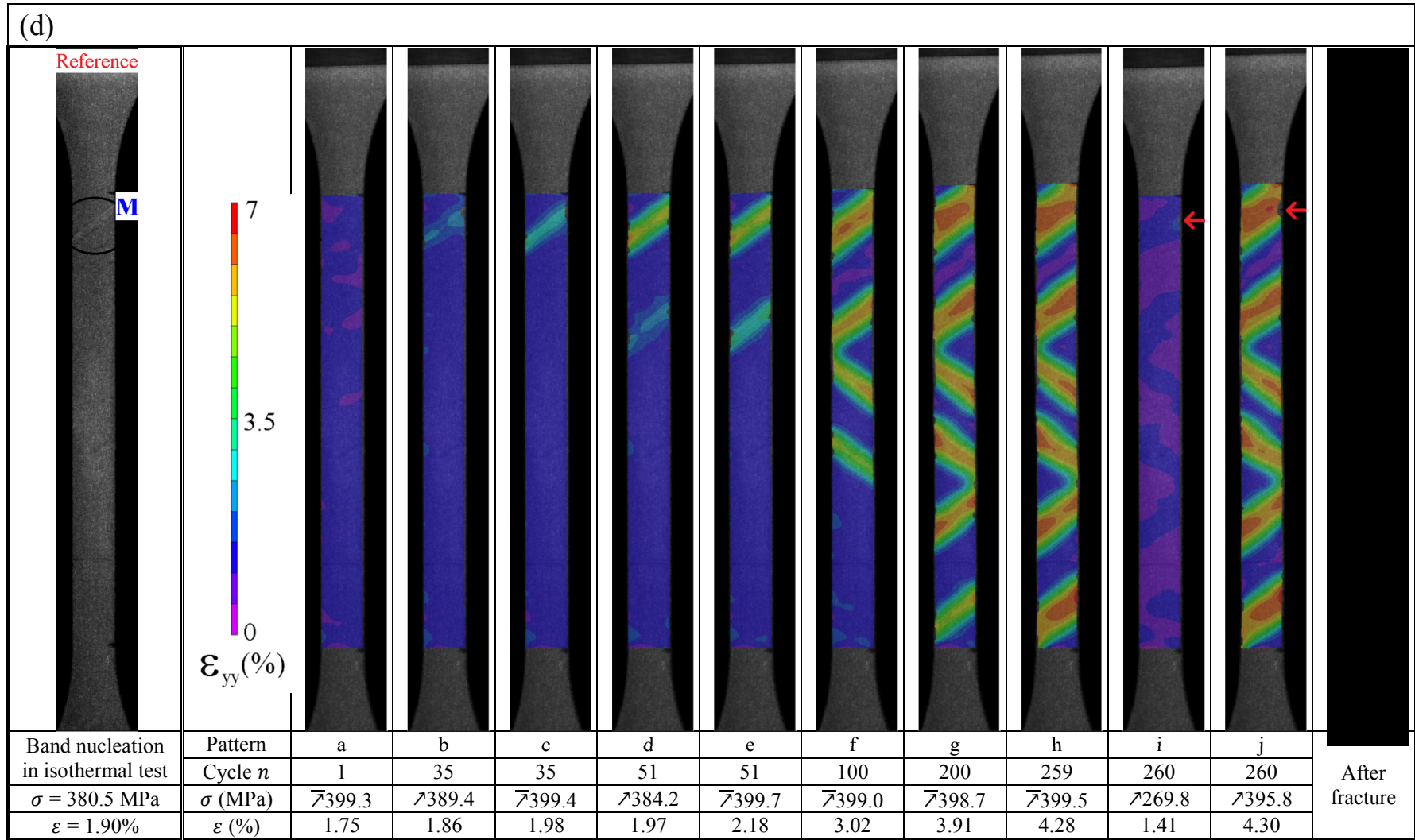


Fig. 4.11 *Continued.* (The leftmost image shows the band nucleation in the reference isothermal test; the arrows indicate the crack nucleation position.)

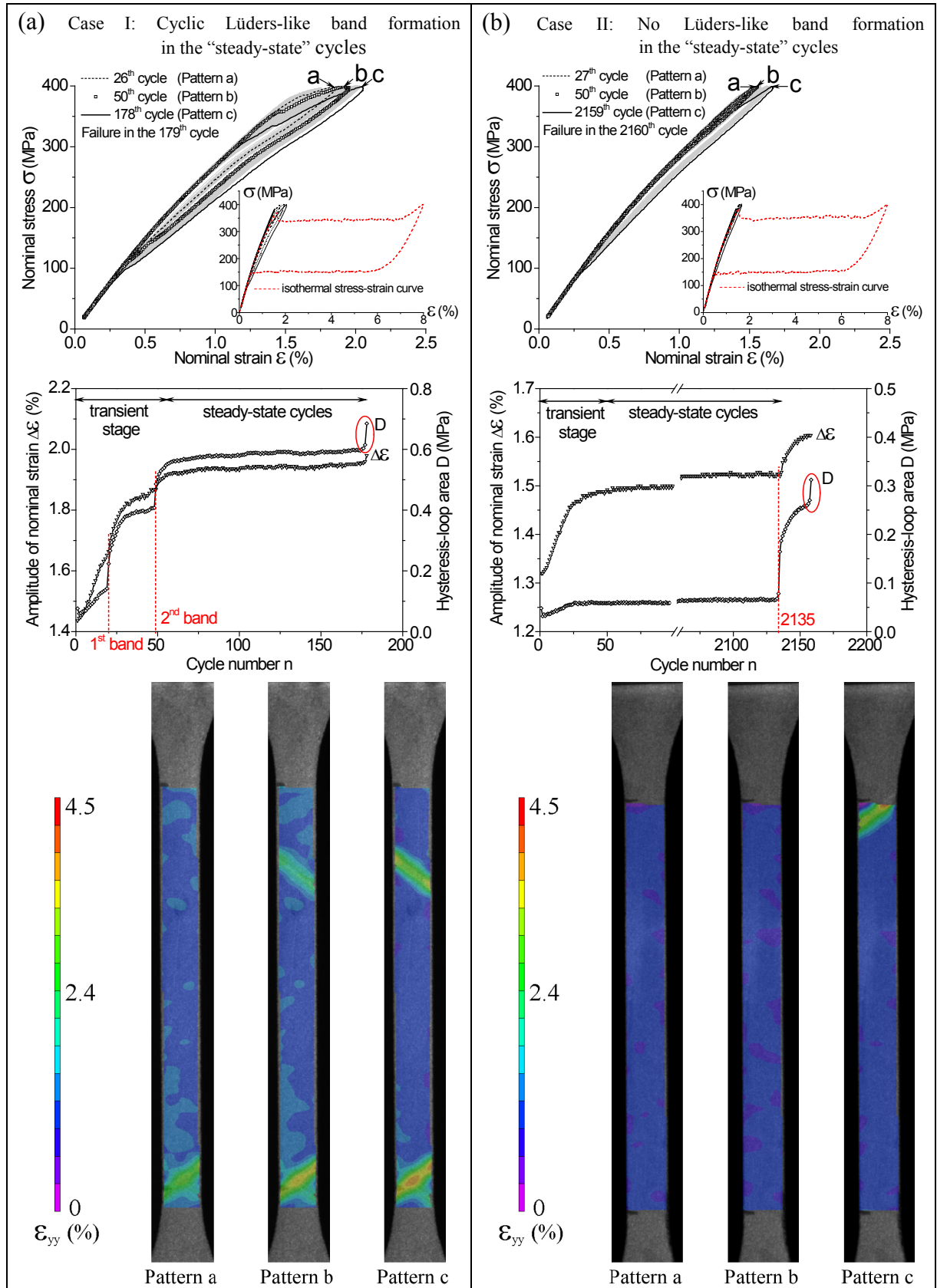


Fig. 4.12 Significant effects of the Lüders-like band formation in the “steady-state” cycles on the specimen’s mechanical responses and the associated fatigue life: (a) **Specimen  $A_{400}^1$  with Lüders-like bands** in the “steady-state” cycles and (b) **Specimen  $D_{400}^1$  without Lüders-like bands** in the “steady-state” cycles.

#### 4.2.3.3 High frequency ( $f = 1$ Hz)

When the applied frequency further increased to 1 Hz, the formation of Lüders-like bands was more difficult as shown in Fig. 4.12: there were only two small bands nucleating in the “steady-state” cycles ( $n > 50$ ) in Case I, while a band nucleated just before the fracture failure in Case II. That is to say, when the applied stress  $\sigma_{max}$  is slightly higher than the isothermal A→M transformation stress  $\sigma_0^{A \rightarrow M}$ , the high frequency (1 Hz) leading to a temperature rise, makes  $\sigma_0^{A \rightarrow M}$  (according to Clausius–Clapeyron relation) increase to be close to (or higher than)  $\sigma_{max}$  so that the massive transformation (with Lüders-like bands) can’t always be triggered, depending on the initial defects of the individual specimens. That’s why the two Specimens  $A_{400}^1$  and  $D_{400}^1$  under the same loading scheme ( $\sigma_{max} = 400$  MPa and  $f = 1$  Hz) could have significantly different behaviors. It is also noted that the fatigue life of Case II ( $N_f = 2160$ ) is much longer than that of Case I ( $N_f = 179$ ). That means the active zones with the cyclic Lüders-like band nucleation and annihilation in the “steady-state” cycles (like Case I) would accelerate the material damage, leading to a shorter fatigue life.

The strain profiles of typical Lüders-like band patterns at different loading frequencies are compared in Fig. 4.13, where the high-strain domains of the low frequency (0.01 Hz) can reach saturated transformation strain (larger than 6%), while the high-strain domains of the high frequency (1 Hz) can’t fully develop (with a strain smaller than 4%). Based on the evolving strain profiles, the local strain amplitudes  $\varepsilon_{ampl}^{local}$  at the failure points (in the “active zones”) are determined. It is interesting and unexpected that, although  $\varepsilon_{ampl}^{local} = 1.82\%$  at the high frequency (1 Hz) is much smaller than that at the low frequency ( $\varepsilon_{ampl}^{local} = 2.99\%$  for 0.01 Hz), the fatigue life at the high frequency ( $N_f = 179$  for 1 Hz) is **NOT** longer than that at the low frequency ( $N_f = 244$

for 0.01 Hz). In other words, besides the material local strain variation, the varying frequency (or the material local temperature) should have effects on the material fatigue damage.

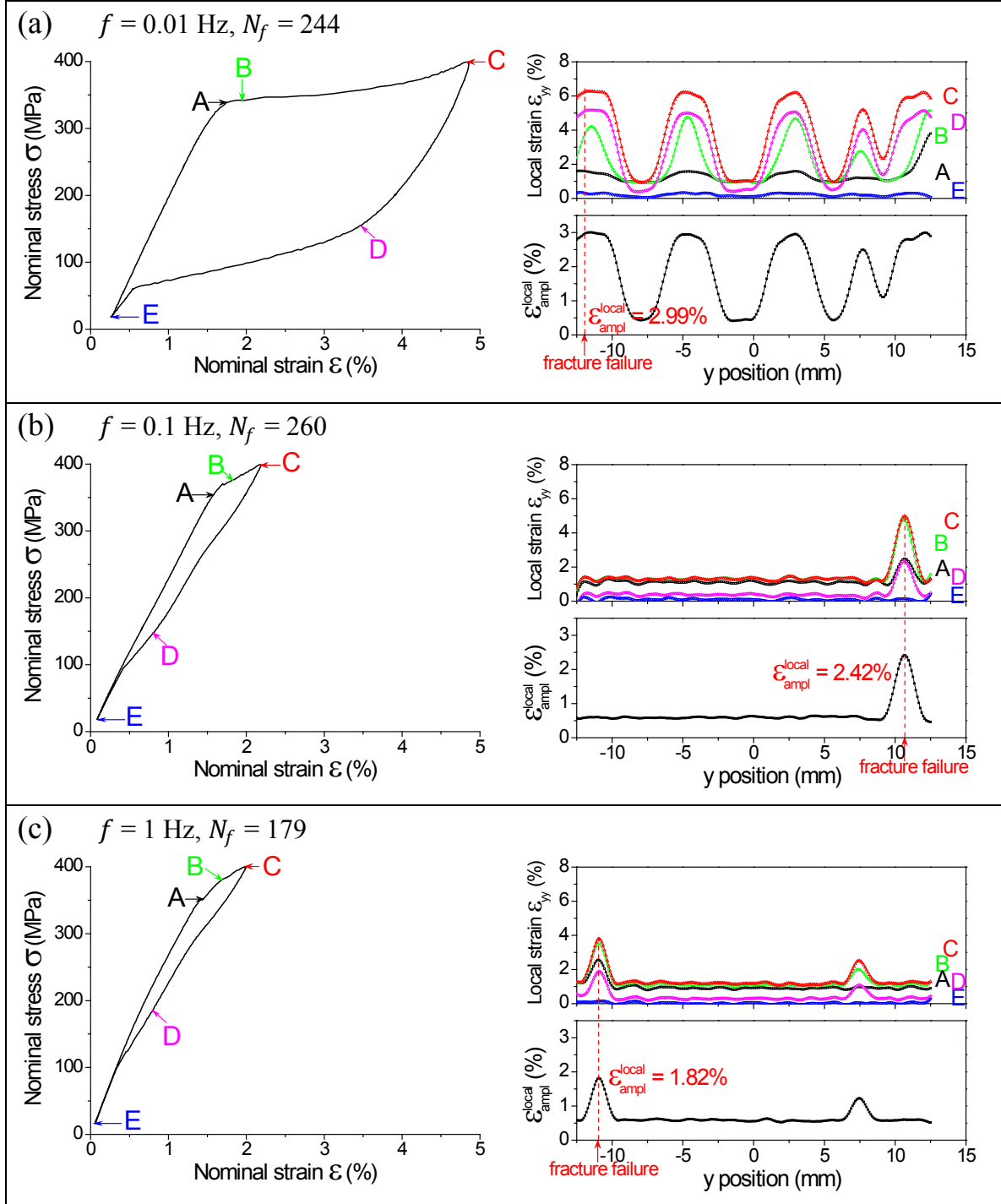


Fig. 4.13 Comparison of the nominal  $\sigma - \epsilon$  curves (left), the strain profiles and the calculated local strain amplitude  $\epsilon_{ampl}^{local}$  (right) in the 50<sup>th</sup> cycles of (a) **Specimen  $A_{400}^{0.01}$** , (b) **Specimen  $A_{400}^{0.1}$** , and (c) **Specimen  $A_{400}^1$** .



#### 4.2.4 Fatigue tests with a low stress level ( $\sigma_{max} = 300$ MPa)

When the applied stress further decreased ( $\sigma_{max} = 300$  MPa, which is much lower than the band-nucleation stress), there was only cyclic “elastic” deformation of Austenite (without Lüders-like band formation) during the fatigue tests (Figs. 4.14(a) and 4.14(b) at  $f = 0.1$  Hz and 1 Hz respectively). Both the two tested Specimens  $A_{300}^{0.1}$  and  $A_{300}^1$  fractured outside the gauge section in the 10853<sup>rd</sup> cycle and the 10274<sup>th</sup> cycle respectively, indicating that the fatigue lives of Austenite taking the “elastic” deformation should be larger than the values measured here ( $N_f > 10853$  for Specimen  $A_{300}^{0.1}$  and  $N_f > 10274$  for Specimen  $A_{300}^1$ ). And these fatigue lives are much larger than those mentioned above with medium and high stress levels of  $\sigma_{max} = 400$  MPa and 500 MPa.

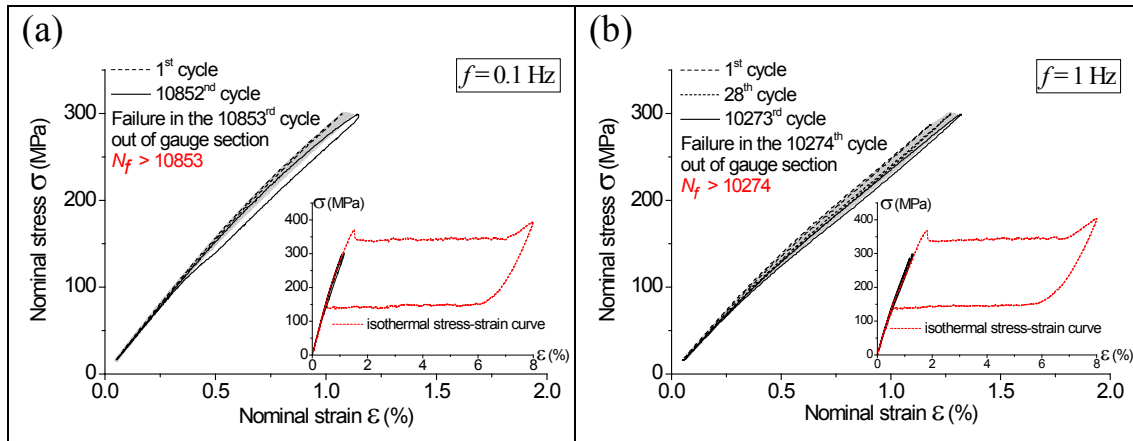


Fig. 4.14 Evolutions of  $\sigma - \epsilon$  curve of the stress-controlled tensile fatigue tests on (a) Specimen  $A_{300}^{0.1}$  with  $\sigma_{max} = 300$  MPa and  $f = 0.1$  Hz and (b) Specimen  $A_{300}^1$  with  $\sigma_{max} = 300$  MPa and  $f = 1$  Hz.

### 4.3 Discussion

The typical patterns and all the fatigue lives  $N_f$  of the tests under the different stresses and frequencies are summarized in Fig. 4.15. The specimens under the cyclic loadings have “active zones” (where fatigue failure occurs due to large strain variations) and “non-active zones” (with only “elastic” deformation of Austenite

or Martensite phase) as shown in Fig. 4.15(a). It is seen that the shaded “active zones” (of cyclic band formation/evolution) depend on both the applied stress and frequency: when the stress is large (significantly larger than the isothermal band-nucleation stress  $\sigma_0^N$ ), the number of “active zones” increases with the frequency, and the zones become slimmer due to temperature effects [68]; when the stress is only slightly higher than  $\sigma_0^N$ , the volume of the “active zones” decreases with increasing frequency (and the “active zones” also become slimmer). In all the cases, the fatigue failures occur in the “active zones”, because the “active zones” have a larger strain variation (oscillation amplitude  $\varepsilon_{ampl}^{local}$ ) than the “non-active zones”. Figure 4.15(b) indicates that, the higher is  $\varepsilon_{ampl}^{local}$  in the “active zones”, the shorter fatigue life they have; moreover, increasing the applied frequency (increasing the temperature effect) leads to a shorter life, even though a high frequency leads to slim “active zones” with a low strain amplitude  $\varepsilon_{ampl}^{local}$  (see Fig. 4.13). Besides the dependence on the local strain variation, fatigue life  $N_f$  also relies on the stress level as shown in Fig. 4.15(c), where  $N_f$  basically decreases with increasing the stress level. Particularly, when the stress is close to the isothermal band-nucleation stress  $\sigma_0^N$ , the formation/nucleation of the bands also depends on the initial defects of specimens, leading to a large scattering of the fatigue lives; for example, the fatigue life scatters from 179 to 2160 for the cases of  $\sigma_{max} = 400$  MPa and  $f = 1$  Hz (see the data of both the red open and solid circles in Fig. 4.15(c)).

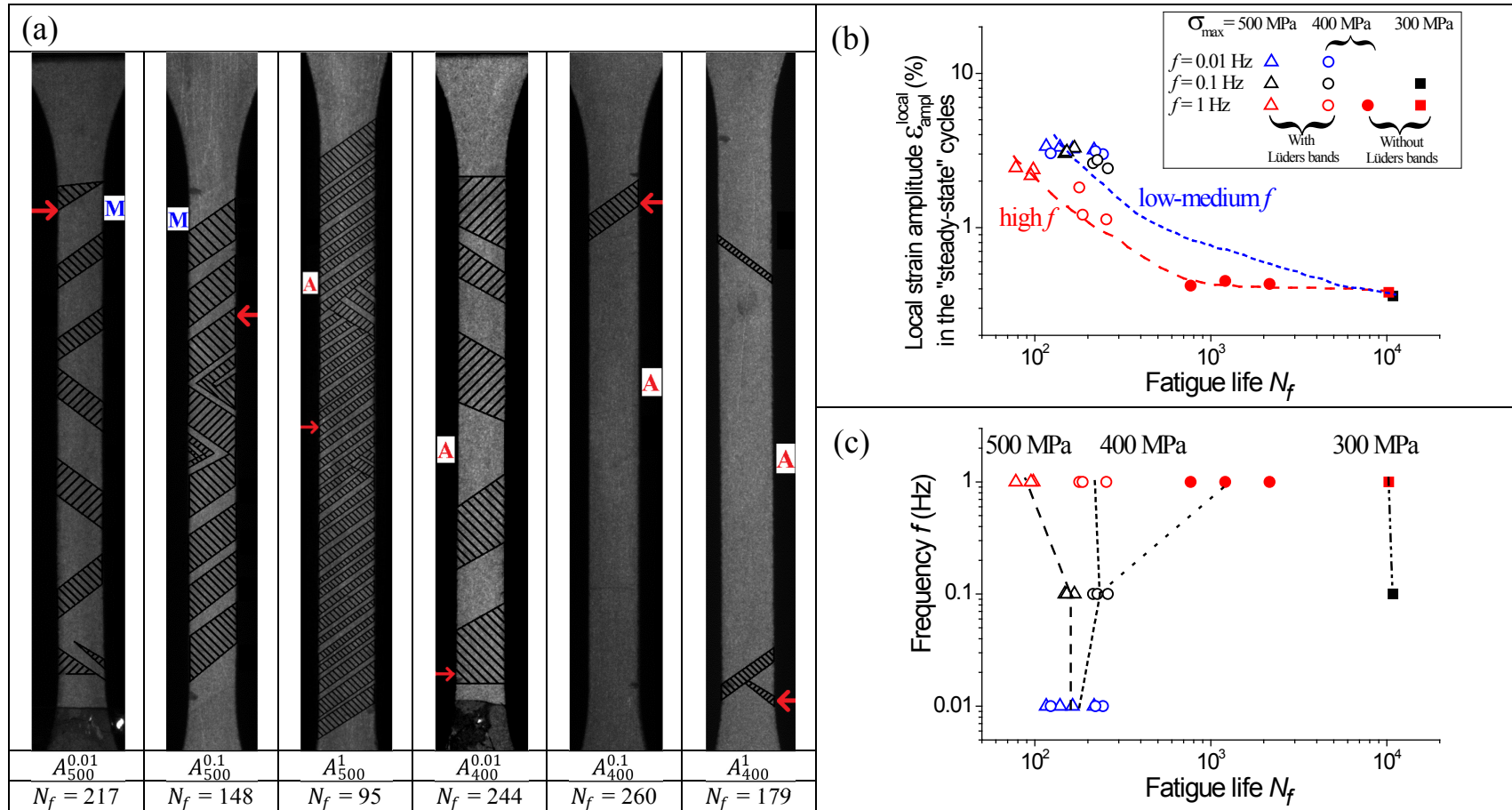


Fig. 4.15 (a) Typical Lüders-like band patterns under different loading conditions (shaded “active zones” with cyclic  $A \leftrightarrow M$  phase transformation and the unshaded “non-active zones” with cyclic “elastic” deformation of residual Martensite or residual Austenite) demonstrate the effects of the applied stress and frequency; the fatigue failure always occurred in one of the “active zones” indicated by the arrows; (b) The dependence of the fatigue life  $N_f$  on the local strain amplitude  $\epsilon_{ampl}^{local}$  in the “steady stage”; (c) The dependence of  $N_f$  on the applied stress and frequency, where  $N_f$  basically decreases with increasing the stress level. (The dashed lines just guide the eyes.)

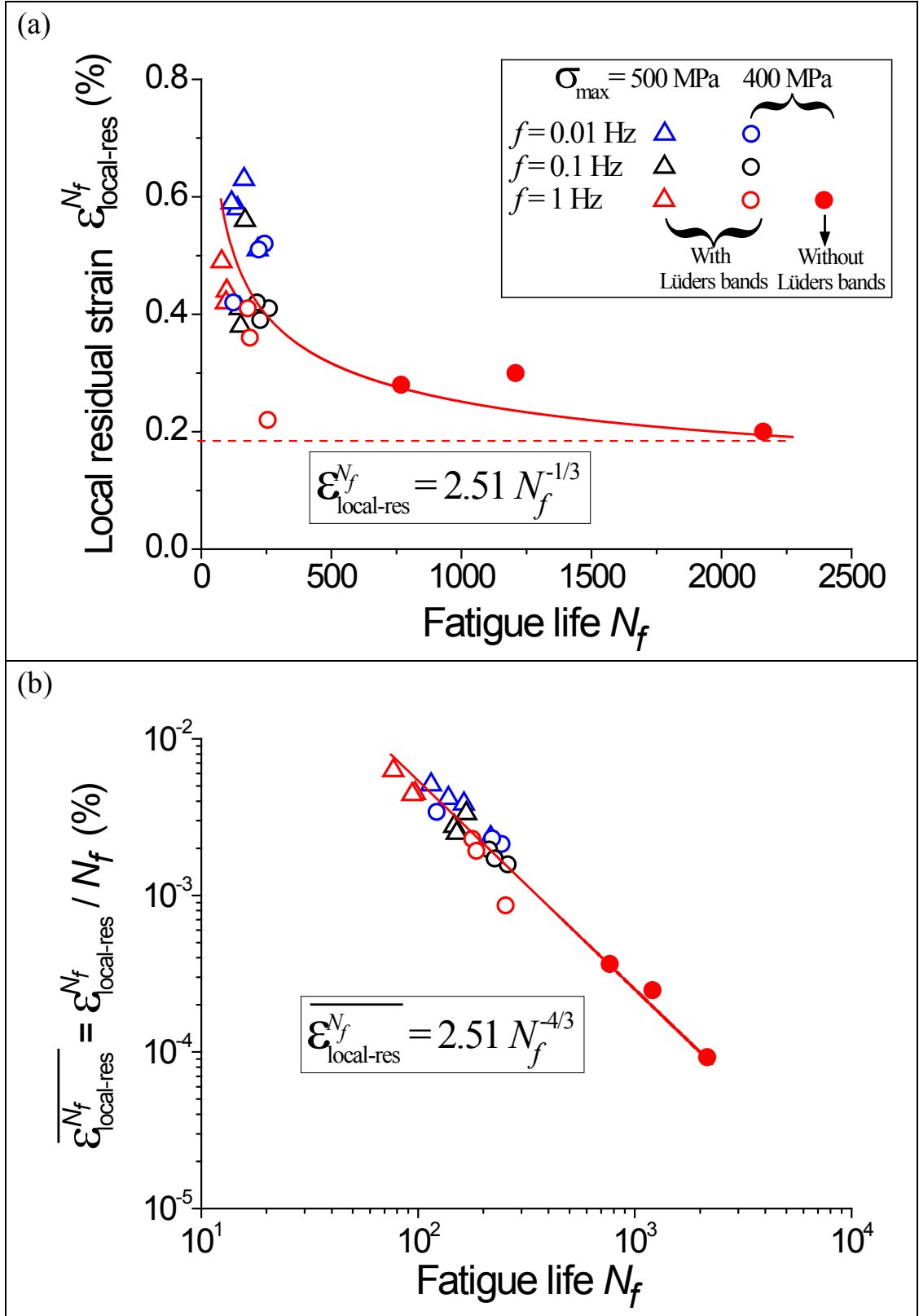


Fig. 4.16 The dependences of the fatigue life  $N_f$  on (a) the local residual strain  $\epsilon_{local-res}^{N_f}$  and (b) the average accumulation rate of the local residual strain  $\overline{\epsilon_{local-res}^{N_f}} = \epsilon_{local-res}^{N_f} / N_f$ .

In addition to the local strain oscillation amplitude, the residual strain is expected to have a close relation with the material's microstructure degradation and fatigue [5, 54, 56]; the accumulation of the residual strain in the stress-controlled cyclic tests is termed as “ratcheting” effects by [52, 82]. Here, instead of the nominal residual strain (the apparent residual strain from the cyclic nominal stress-strain curve), the local residual strain in the “active zones” (measured by DIC method) is discussed in correlation with the material's fatigue, because the nominal strain is usually not the same as the local strain in the “active zones” where the fatigue failure occurs. Figure 4.16(a) summarizes the local residual strains in the “active zones” in the last fatigue cycle (i.e., local residual strain accumulation after  $N_f$  cycles of loading),  $\varepsilon_{local-res}^{N_f}$ , while Fig. 4.16(b) plots the average increase in the local residual strain per cycle (i.e., local residual strain accumulation rate, defined as  $\overline{\varepsilon_{local-res}^{N_f}} = \varepsilon_{local-res}^{N_f}/N_f$ ). It is seen that the relation between  $\varepsilon_{local-res}^{N_f}$  and  $N_f$  can be roughly described by an equation:

$$\varepsilon_{local-res}^{N_f} = \frac{2.51}{\sqrt[3]{N_f}} \quad (2)$$

It is interesting to note that the “fatigue limit” in term of the residual strain is around 0.2% (i.e., the fatigue failure would not occur before the material's local residual strain accumulation reaches 0.2%). From Eq. (2), the local residual strain accumulation rate can be derived as:

$$\overline{\varepsilon_{local-res}^{N_f}} = \frac{2.51}{N_f^{4/3}} \quad (3)$$

which provides a simple prediction on the fatigue life (as shown in Fig. 4.16(b)): if the cyclically-loaded material accumulates residual strain very quickly, its fatigue life would be short. It should be noted that the prediction is based on the local material residual strain, not the structural nominal residual strain. For example, although the

accumulation rate (per cycle) of the nominal residual-strain of the low-frequency test ( $f = 0.1$  Hz) in Fig. 4.6(a) is much faster than that of the high-frequency test ( $f = 1$  Hz) in Fig. 4.8(a), the accumulation rate of the local residual strain (in the “active zones”) of the low-frequency test is less than that of the high-frequency test (see the data of the black and red triangles in Fig. 4.16(b)). So, the local residual strain, rather than the nominal residual strain is a good indicator on the material’s damage leading to the fatigue failure.

#### 4.4 Conclusions

The fatigue behaviors of pseudoelastic NiTi polycrystalline strips under stress-controlled tensile loadings with different stress levels ( $\sigma_{max} = 300$  MPa, 400 MPa, and 500 MPa) and frequencies ( $f = 0.01$  Hz, 0.1 Hz, and 1 Hz) were investigated via the in-situ Lüders-like band pattern observation. The mechanical stress-strain responses and the patterns of the localized martensitic phase transformation (Lüders-like bands) evolve with the cycle number and depend on the applied  $\sigma_{max}$  and  $f$  due to the thermo-mechanical coupling and the microstructure degradation. With the in-situ optical observation on the Lüders-like band evolution and the associated local strain measurement (by Digital Image Correlation), the frequency- and stress-dependence of the pattern evolution and the material’s fatigue behaviors can be demonstrated and understood. The following conclusions can be drawn from this chapter.

- The NiTi specimens under cyclic tensile loadings can have two types of zones: “active zones” (with large strain variation due to forward/reverse martensitic phase transformation) and “non-active zones” (with small strain variation for the “elastic” deformation of Austenite or Martensite phase). The applied stress level and the frequency significantly influence the volume of the “active zones”,

and a high frequency leads to slim “active zones” (Fig. 4.15(a)); in all these cases, the fatigue failure occurs in the “active zones”.

- By tracing the deformation history (local strain evolution) of the “active zones” in a whole fatigue test (up to fracture failure), it is found that there are strong correlations between the fatigue life, the local strain oscillation amplitude and oscillation frequency, and the accumulation rate of the irrecoverable residual strain (Fig. 4.15(b) and Fig. 4.16(b)). The larger local strain amplitude, higher frequency, or faster irrecoverable-strain accumulation rate leads to a shorter fatigue life. Particularly, to characterize the material damage, the local residual strain is better than the structural nominal residual strain (derived from the nominal stress-strain curves), because the NiTi SMA specimen’s deformation under tensile loading is usually inhomogeneous (with Lüders-like band formation).
- The applied stress and frequency have important effects on the material’s fatigue life, especially when they qualitatively change the Lüders-like band formation (Fig. 4.15(c)): a high/low stress with/without triggering cyclic band formation like 500MPa/300MPa leads to a short/long fatigue life. Particularly, at a certain critical condition (like  $\sigma_{max} = 400$  MPa and  $f = 1$  Hz), the band formation is very sensitive to the initial defects of the individual specimens so that the fatigue life varies largely, from  $\sim 200$  (with cyclic band formation) to  $\sim 2000$  (without band formation). That poses a question about the theoretical prediction on the material fatigue: a good fatigue criterion should adopt the stress (so-called “S-N” curve), the local strain variation (like Fig. 4.15(b)), or other appropriate parameters? More experiments and theories are needed to answer this question in the future study.

## 5. Conclusions and Prospects

In this thesis, the in-situ observation on the Lüders-like band patterns (due to the localized martensitic phase transformation) was performed, for the first time, in the fatigue analysis of Nickel-Titanium Shape Memory Alloy (NiTi SMA). The multi-scale patterns (macro-scale Martensite/Austenite bands, meso-scale band fronts, micro-scale grain boundaries and Martensite twins, etc.) interacting with the plastic deformation/dislocations make it difficult to explain the material's fatigue behaviors. But on the other hand, such patterns implying the physical principles/mechanisms in the material system provide a new method to tackle the fatigue problem. So, by observing the pattern formation and evolution and measuring the local strains of the NiTi strips in the tensile fatigue tests, the material's localized behaviors were better understood. This fatigue analysis with both qualitative explanation and quantitative measurement would certainly be helpful for understanding and modeling the material's fundamental behaviors.

In Chapter 2, the stress-controlled tensile tests were conducted on the pseudoelastic NiTi polycrystalline strips to investigate the effects of the Lüders-like bands on the fatigue process. It is found that the fatigue process in NiTi polycrystals mainly included three stages: transient stage (shakedown), “steady stage” (“steady-state” cycles), and fracture failure, where the “steady stage” was the main part (about 70% of the total fatigue life) of the entire process. The cyclic localized phase transformation in the “steady stage” caused larger microstructure degradation and led to shorter fatigue lives, compared with the cyclic homogeneous deformation (without Lüders-like bands). Moreover, the fatigue failure always occurred within the Lüders-like band or at the band front, because the band formation was an indicator of the weak zone in a specimen and the cyclic band nucleation/annihilation accelerated the



microstructure degradation in this weak zone. More precisely, the fatigue failure crack nucleated within (at) one of the bands (band fronts) of the “steady-state” cycles; the failure position was not always in the original weakest zone (the 1<sup>st</sup> band-nucleation site). It was also identified that a fatigue criterion for NiTi polycrystals should adopt the local material responses rather than the structural global responses as the governing terms, because the mechanical responses (e.g., deformation strain and energy dissipation) inside the Lüders-like bands were significantly different from the nominal global ones.

Based on the findings in Chapter 2, it was natural to locally observe the Lüders-like band front in order to trace the deformation history of the fatigue-failure material points. It is demonstrated in Chapter 3 that the band-front motion triggering the localized cyclic phase transformation led to a short fatigue life of the material; by contrast, the material under cyclic “elastic” deformation (i.e., without the band-front motion) had a longer fatigue life whose level depended on the material state. In general, the Austenite phase had a longer fatigue life than the Martensite phase under macroscopically elastic deformation; moreover, two Martensite phases (“loading Martensite” and “unloading Martensite”) were identified due to the change of the loading path and had different fatigue lives. It is suggested that the “unloading Martensite” experienced higher stresses had more martensitic phase transformation or/and martensite reorientation so that there were fewer boundaries and less internal friction, compared with the “loading Martensite”. Interestingly, the fatigue failure crack didn’t nucleate at the immobile band front. The optical observation on the band evolution and the full-field strain measurement help explain the non-trivial dependence of the fatigue life of a NiTi SMA structure (strip) on the nominal strain

variation and provide hints for developing a material fatigue criterion in terms of local material strain variation.

In Chapter 4, systematic fatigue tests under stress-controlled tensile loadings were conducted with the typical stress levels and loading frequencies. The mechanical stress-strain responses and macro patterns of the localized martensitic phase transformation evolved with the cycle number and depended on the applied stress level and frequency in a complicated way. Some evolutions included a “transient stage” and a “steady stage” while the others just had a “transient stage” (i.e., fatigue failure occurred before reaching a “steady stage”). Moreover, a specimen’s gauge section could be divided into two types of zones: “active zones” with cyclic Austenite ↔ Martensite phase transformation of a large local strain oscillation and “non-active zones” with cyclic macroscopically elastic deformation of the untransformed Austenite or/and the residual Martensite. In all the tests, the fatigue failure occurred in the “active zones”. The applied stress level and the frequency significantly influenced the number and volume of the “active zones”. Specially, under a high stress level, low frequencies led to a large part of residual Martensite bands (“non-active zones”) stabilized by the low temperature at the unloading end, which contributed to a major part of nominal residual strain; on the contrary, a high frequency led to a large number of slim “active zones” and incomplete forward phase transformation at the loading end due to the high temperature. By tracing the local strain evolution in the “active zones”, strong correlations were found between the fatigue life, the local strain oscillation amplitude and oscillation frequency, and the accumulation rate of the local residual strain: the larger local strain amplitude, higher frequency, or faster local residual-strain accumulation rate led to a shorter fatigue life. Particularly, to characterize the material damage, the local residual strain is better than the structural nominal residual strain

(derived from the nominal stress-strain curves), because the NiTi SMA specimen's deformation under tensile loading is usually inhomogeneous (with Lüders-like band formation).

There are several topics of interest when considering directions for ongoing and future research. Actually, there are still several factors (such as the specimen geometry, material texture, boundary condition, grain size, etc.) whose effects on the fatigue behaviors need to be evaluated to make the current fatigue criterion more solid and general. Experiments directly following the line of thought of those reported in Chapter 4 will be to repeat the stress-controlled fatigue tests with synchronized full-field strain and full-field temperature (by an infrared camera) measurement, so both the local strain and local temperature of the fatigue-failure material point can be obtained and the material fatigue criterion could be refined by clarifying the frequency/thermal effect. It will be also worth repeating the strain-controlled fatigue tests of Chapter 3 (by carefully varying the applied nominal mean strain or/and strain amplitude within the upper stress plateau) within the lower stress plateau to further examine effects of the loading path. The test with the in-situ observation on the crack propagation by microscope (Fig. 3.7) will also deserve to be repeated, through which more microscopic details about the crack nucleation from the Lüders-like band front would be revealed. Also from a microscopic point of view, the fatigue fracture surface or/and the cycled but non-fractured specimen's surface can be systematically investigated by SEM, X-ray diffraction, Electron backscatter diffraction, or other techniques to understand the failure mechanisms and to quantify the microstructure degradation caused by the cyclic localized phase transformation (in the “active zones”) or the cyclic “elastic” deformation (in the “non-active zones”) of different material phases (Austenite, “loading Martensite”, and “unloading Martensite”, which were

identified in Chapter 3). To sum up, this thesis is only a beginning work to study the SMA fatigue by observing the localized martensitic phase transformation at macro and meso scales, and the so-called “active zones” and “non-active zones” strongly depend on the resolution of optical observation system. So, the derived fatigue criterion based on the local strains is limited by the resolution of DIC method and needs to be refined and include the rate/thermal effect after checking the local temperatures.

Since it has been recognized that based on the cycle-nominal mechanical responses there were no exact “steady-state” cycles in some cases — the specimens fractured before reaching the “steady-state” cycles, it will be interesting to compare the evolution of microstructure degradation, the evolution of local responses, and the evolution of macroscopic patterns, in order to find a relation between these evolutions of multi-scales. In a global picture, the studied macroscopic patterns in NiTi SMA (a complex system) belong to the emergent phenomena which can be widely found in many domains; one such relation between micro-behaviors and macro-patterns, combined with theoretical analysis and computational models, will help to understand or clearly describe universal features of the emergent phenomena in nature.

## Appendix: Experimental results of Specimens *B*, *C*, *E*~*H* of Chapter 2

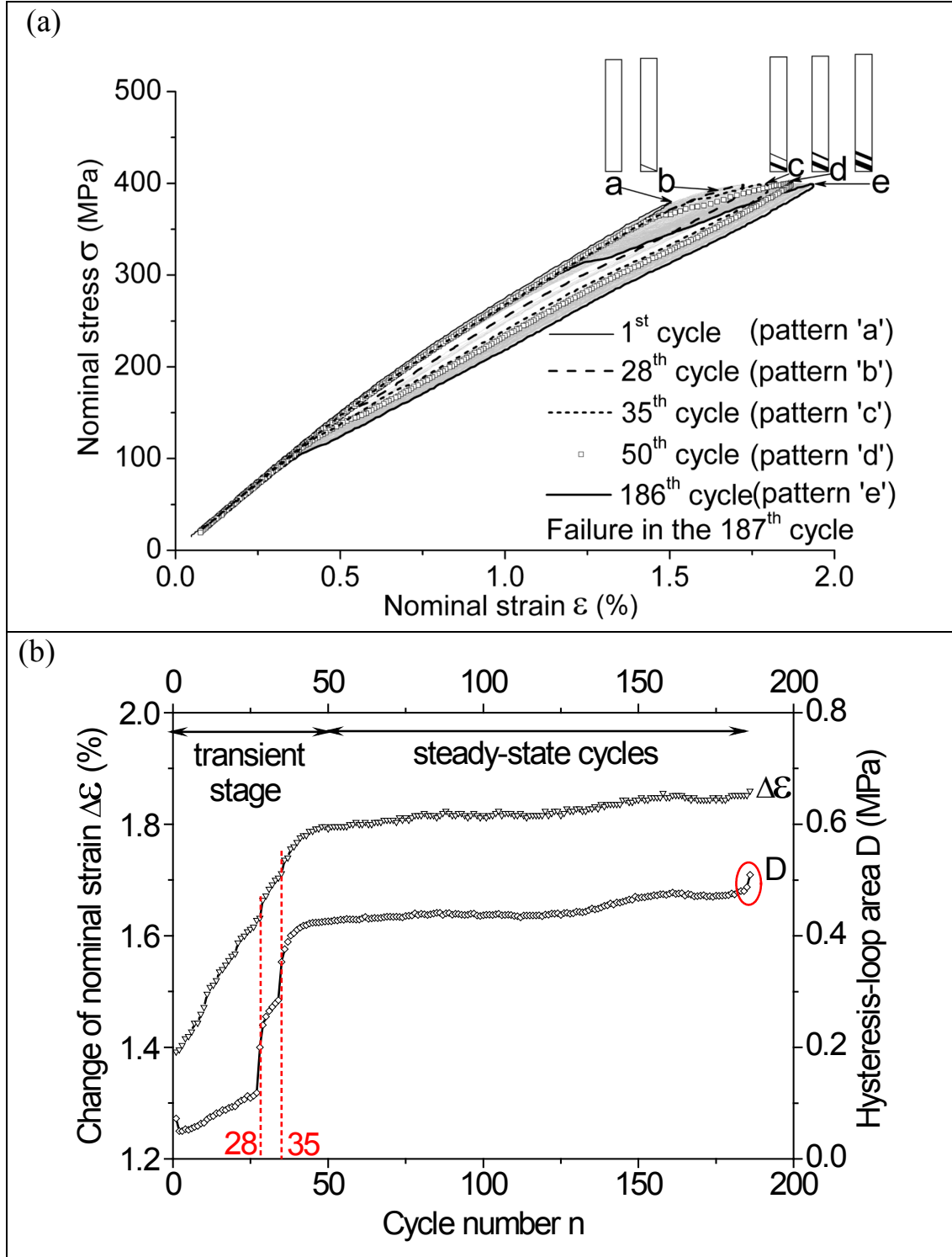


Fig. A1 The stress-controlled tensile fatigue test on Specimen *B* with  $\sigma_{max} = 400$  MPa and  $f = 1$  Hz (Lüders-like band appeared **before** the “steady-state” cycles): (a) stress-strain curve evolution and schematic patterns, (b) evolutions of the cycle features  $\Delta\epsilon$  and  $D$ , and (c) optical observation on the Lüders-like band pattern.

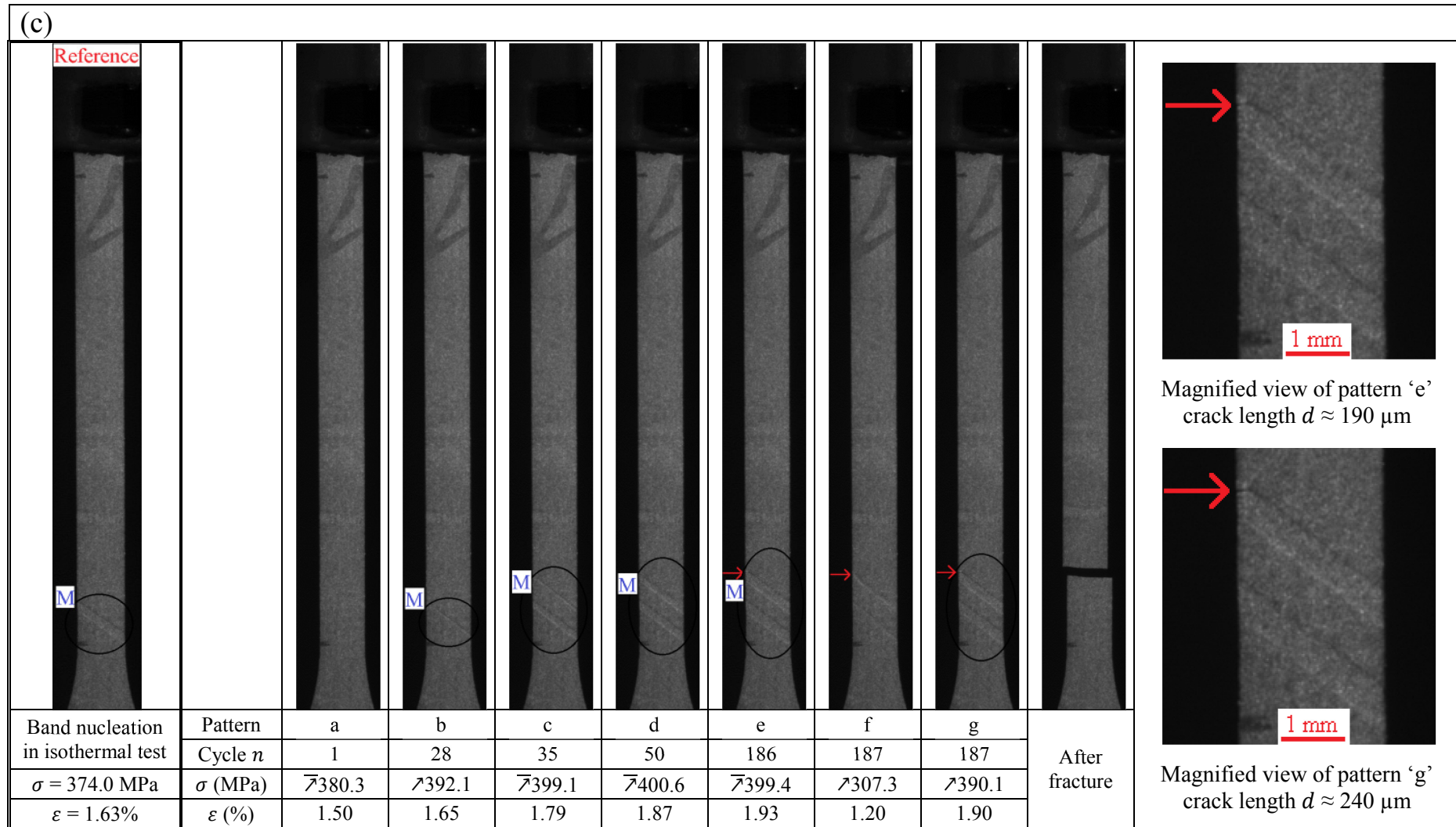


Fig. A1 *Continued.* (An acoustic emission (AE) sensor was attached to the upper end attempting to acquire the AE signals.)

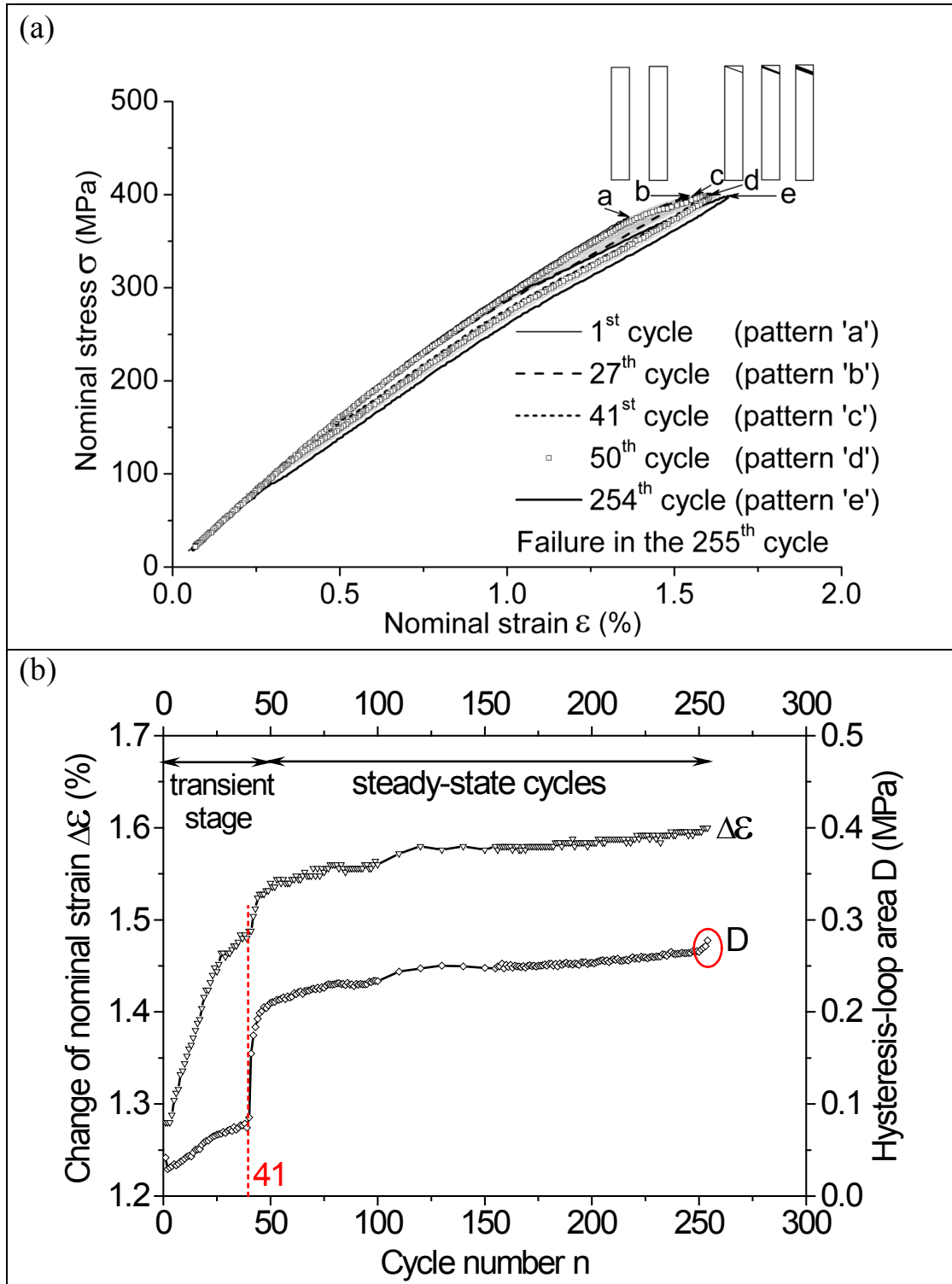


Fig. A2 The stress-controlled tensile fatigue test on Specimen *C* with  $\sigma_{max} = 400$  MPa and  $f = 1$  Hz (Lüders-like band appeared *before* the “steady-state” cycles): (a) stress-strain curve evolution and schematic patterns, (b) evolutions of the cycle features  $\Delta\epsilon$  and  $D$ , and (c) optical observation on the Lüders-like band pattern.

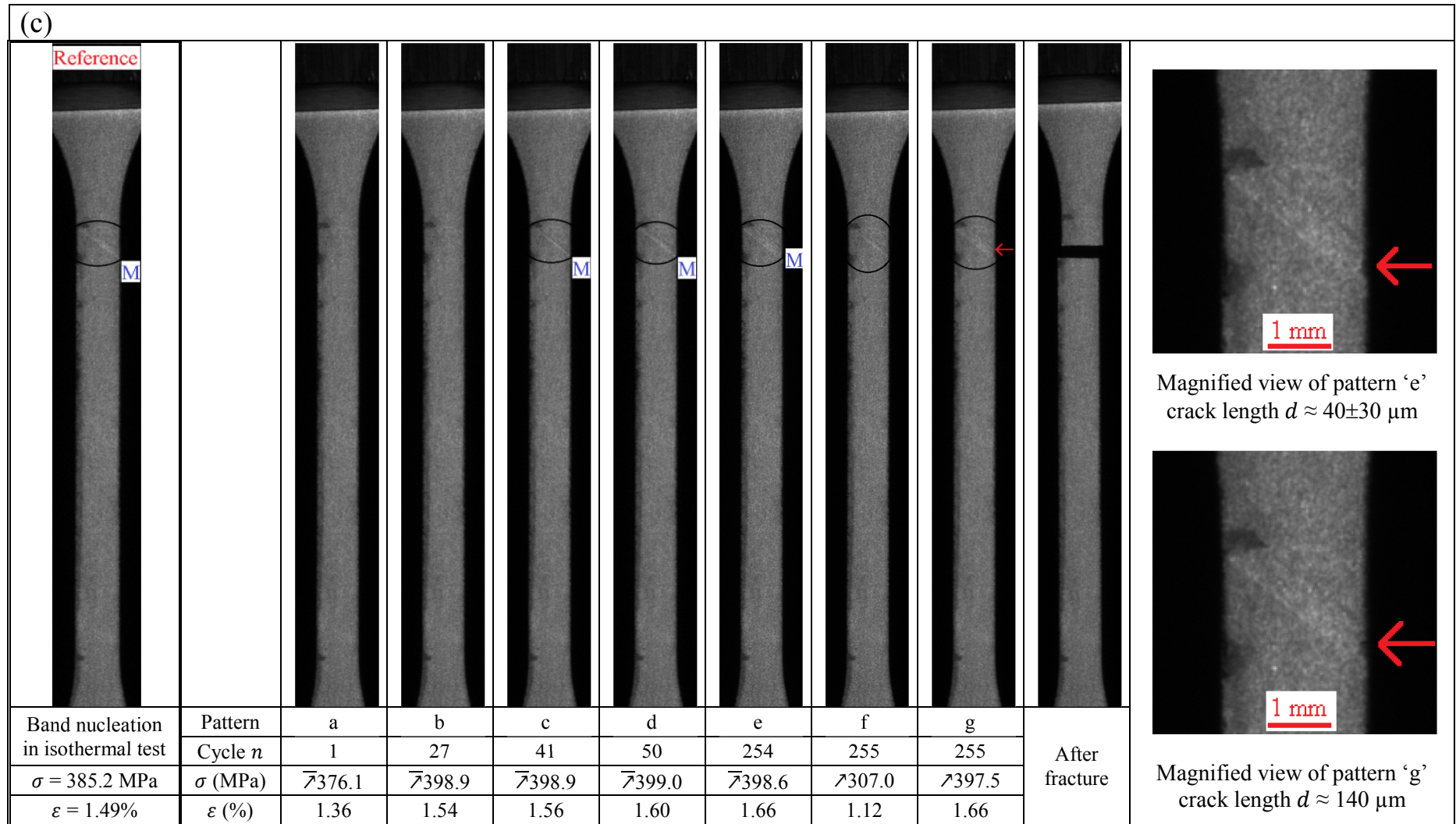


Fig. A2 Continued.



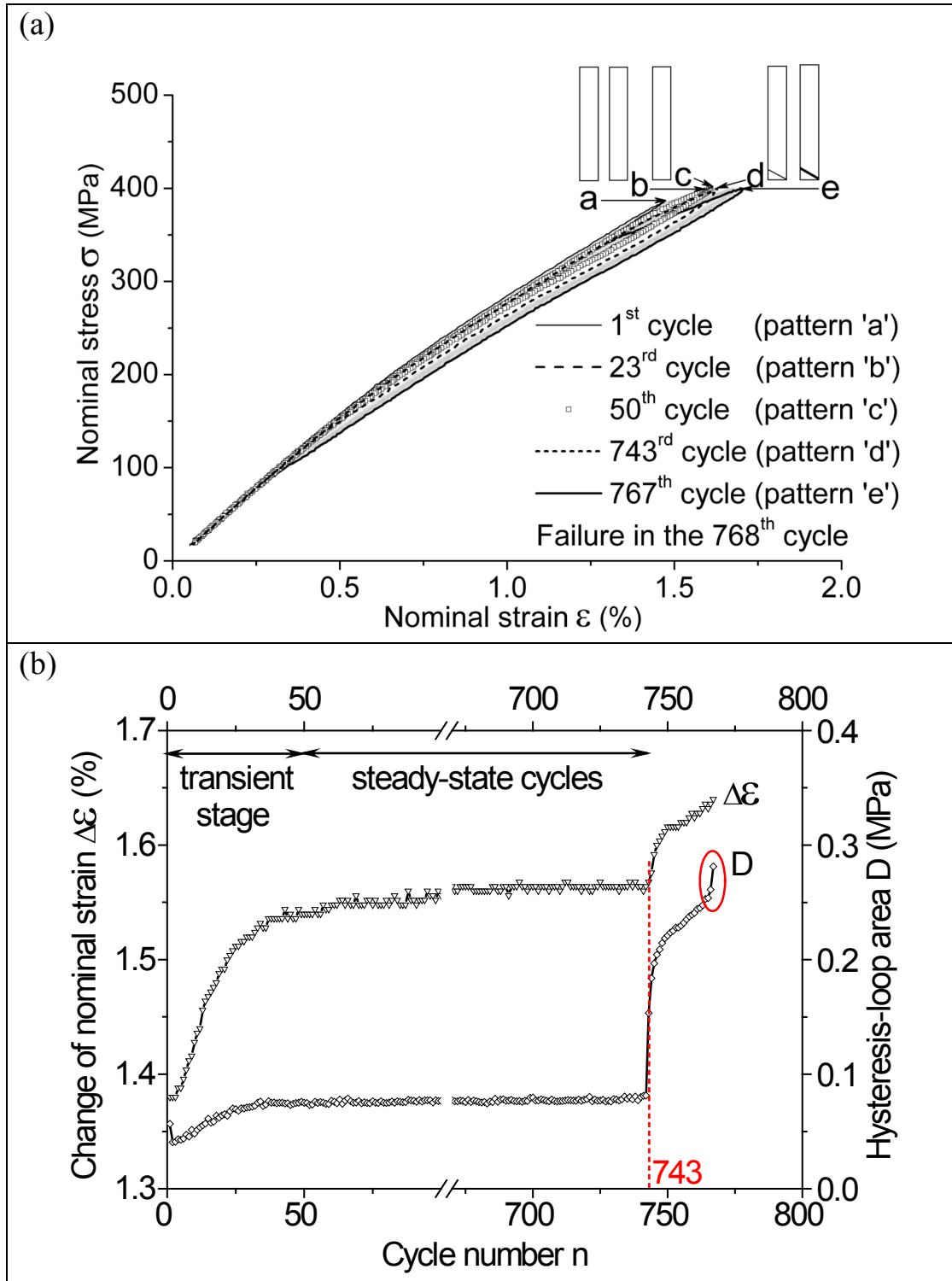


Fig. A3 The stress-controlled tensile fatigue test on Specimen *E* with  $\sigma_{max} = 400$  MPa and  $f = 1$  Hz (Lüders-like band appeared **after** the “steady-state” cycles): (a) stress-strain curve evolution and schematic patterns, (b) evolutions of the cycle features  $\Delta\varepsilon$  and  $D$ , and (c) optical observation on the Lüders-like band pattern.

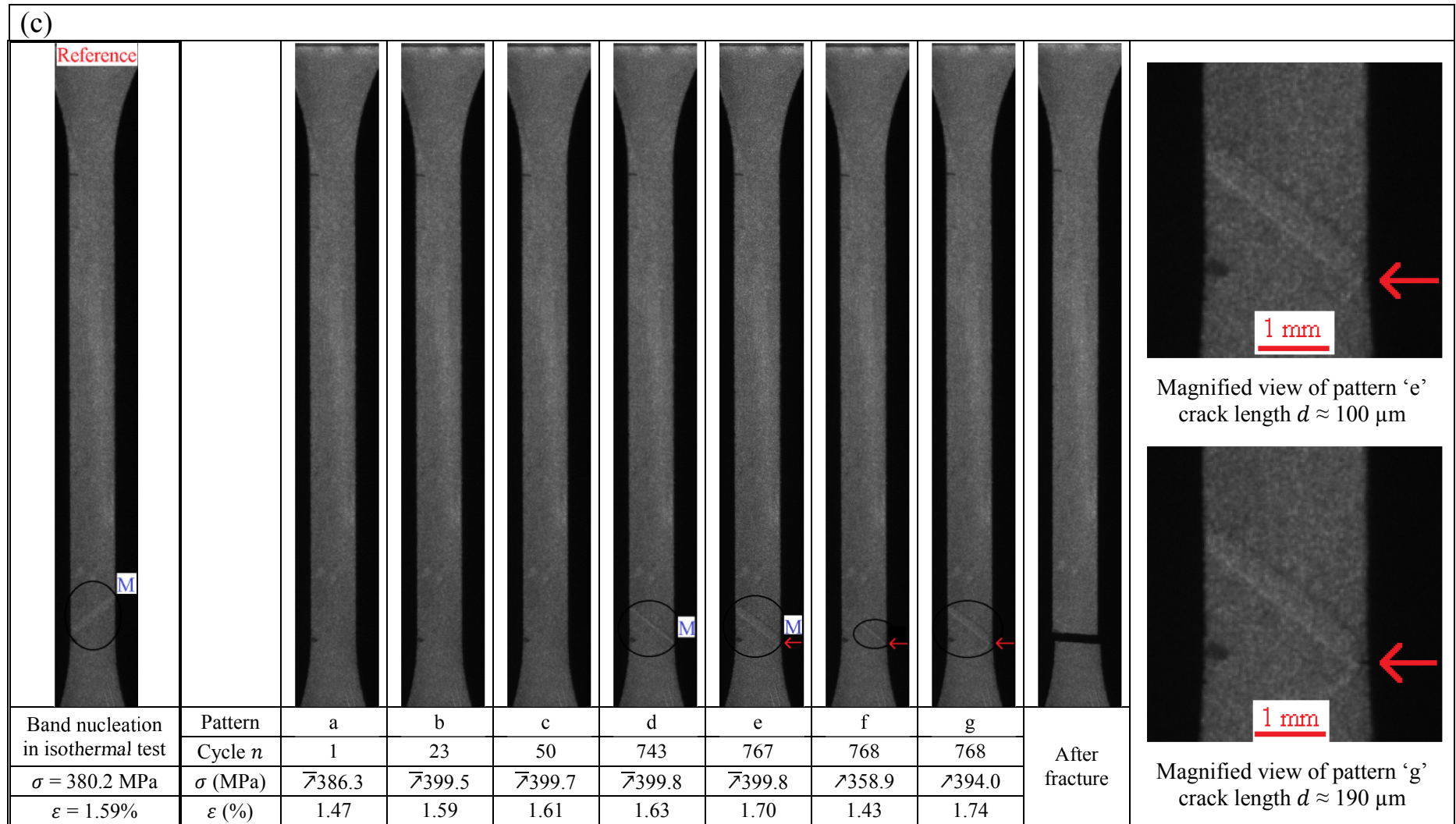


Fig. A3 Continued.

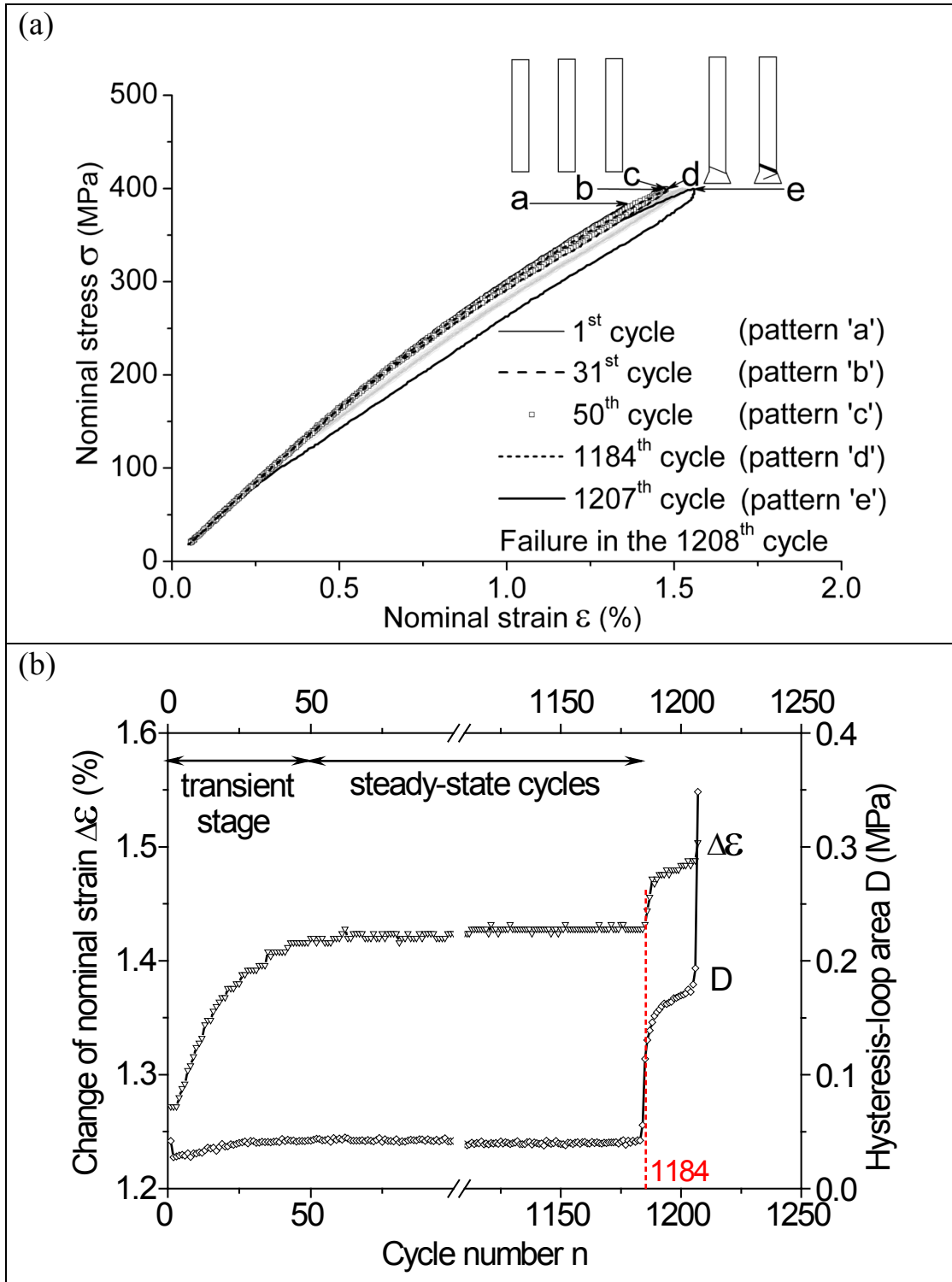


Fig. A4 The stress-controlled tensile fatigue test on Specimen  $F$  with  $\sigma_{max} = 400$  MPa and  $f = 1$  Hz (Lüders-like band appeared **after** the “steady-state” cycles): (a) stress-strain curve evolution and schematic patterns, (b) evolutions of the cycle features  $\Delta\epsilon$  and  $D$ , and (c) optical observation on the Lüders-like band pattern.

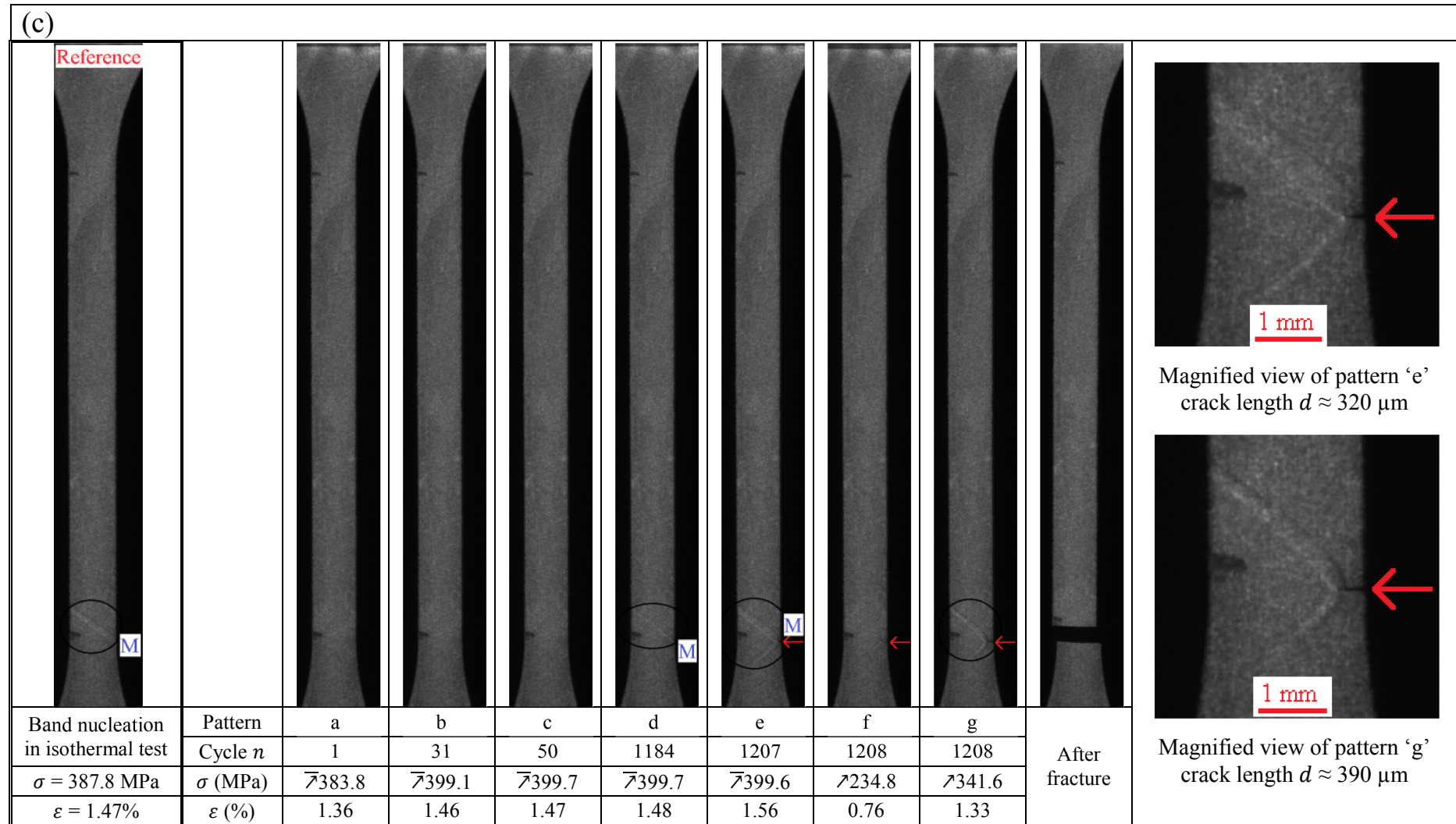


Fig. A4 Continued.

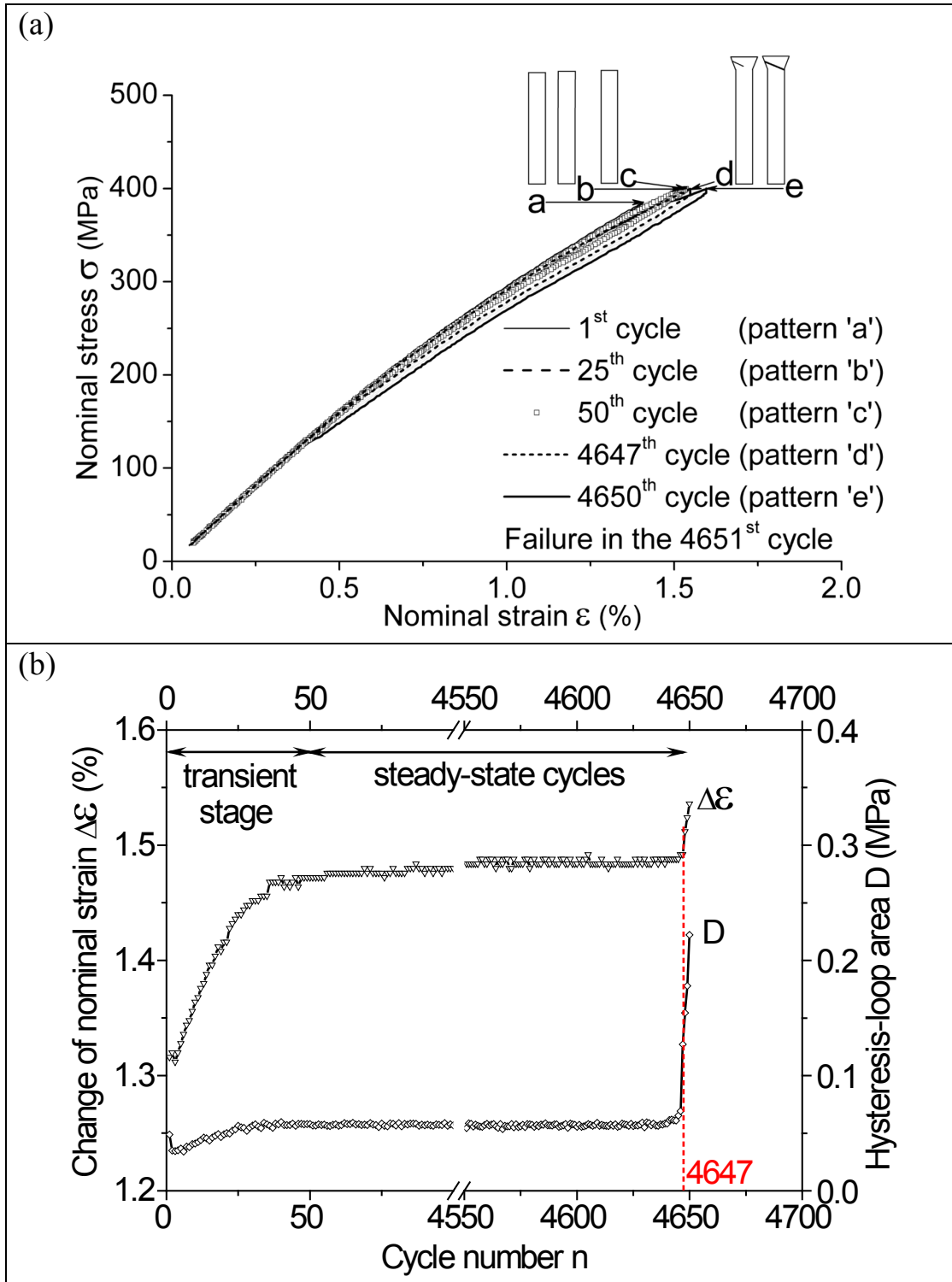


Fig. A5 The stress-controlled tensile fatigue test on Specimen *G* with  $\sigma_{max} = 400$  MPa and  $f = 1$  Hz (Lüders-like band appeared **after** the “steady-state” cycles): (a) stress-strain curve evolution and schematic patterns, (b) evolutions of the cycle features  $\Delta\epsilon$  and  $D$ , and (c) optical observation on the Lüders-like band pattern.



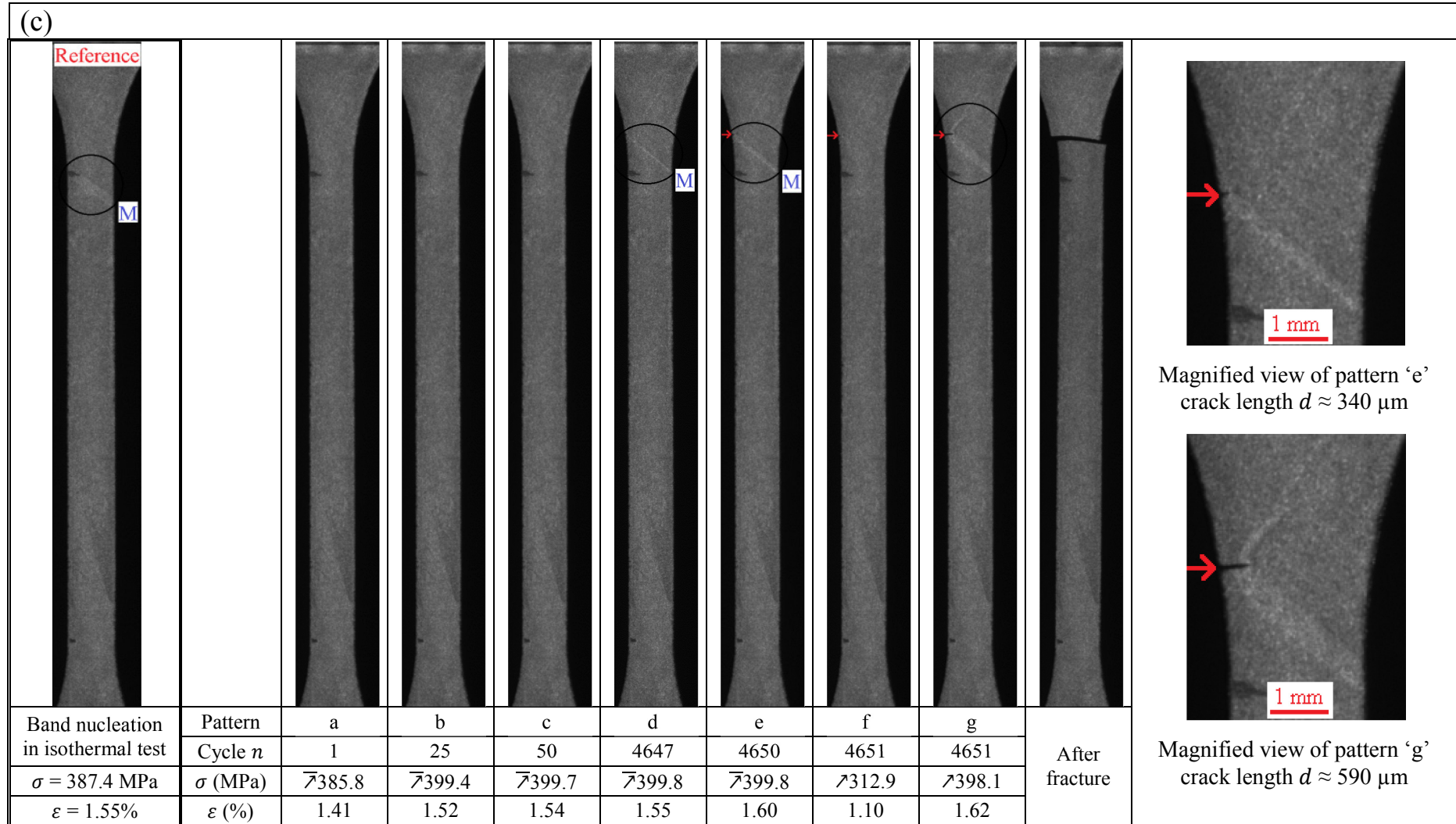


Fig. A5 Continued.

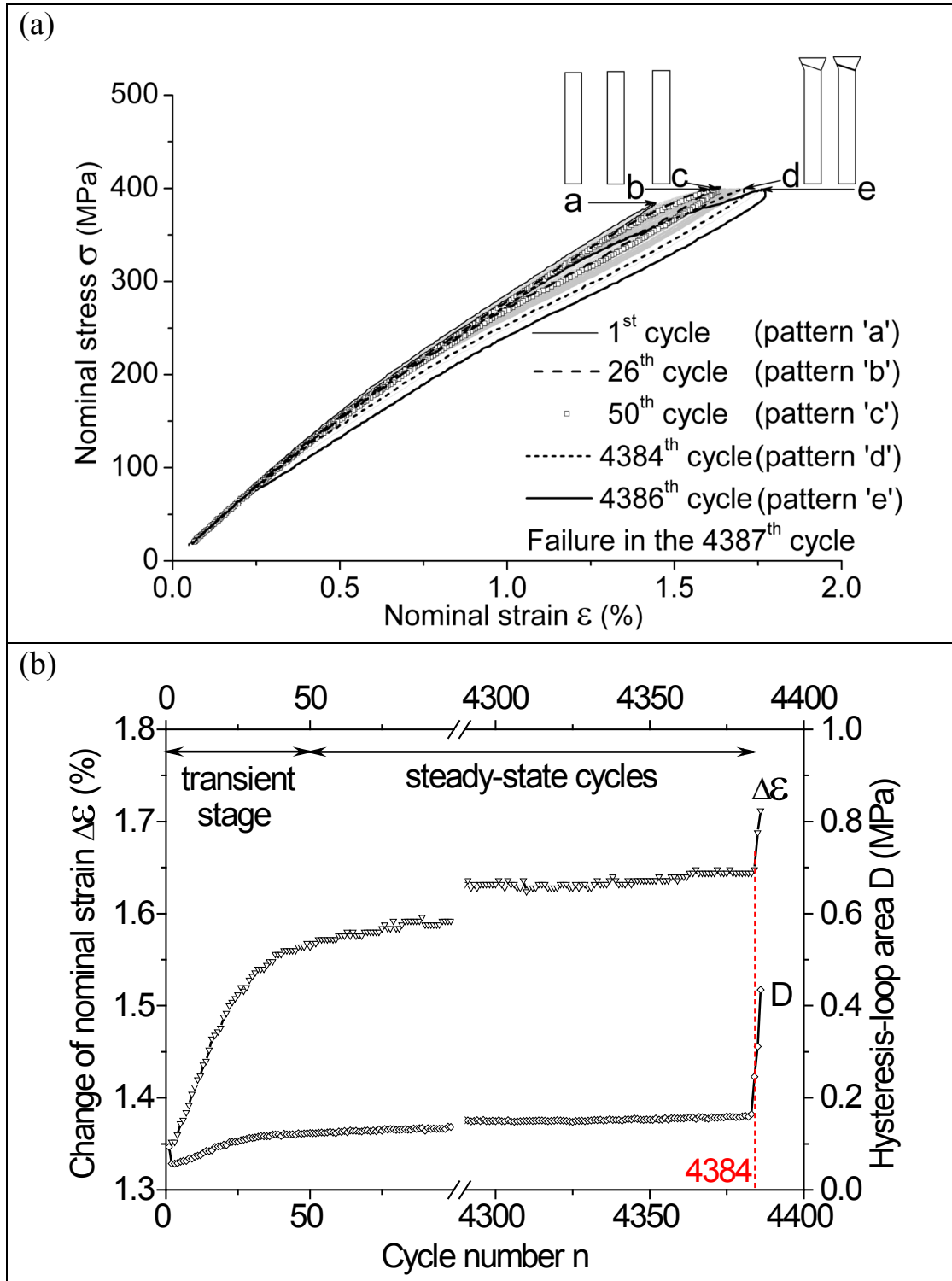


Fig. A6 The stress-controlled tensile fatigue test on Specimen *H* with  $\sigma_{max} = 400$  MPa and  $f = 1$  Hz (Lüders-like band appeared *after* the “steady-state” cycles): (a) stress-strain curve evolution and schematic patterns, (b) evolutions of the cycle features  $\Delta\epsilon$  and  $D$ , and (c) optical observation on the Lüders-like band pattern.

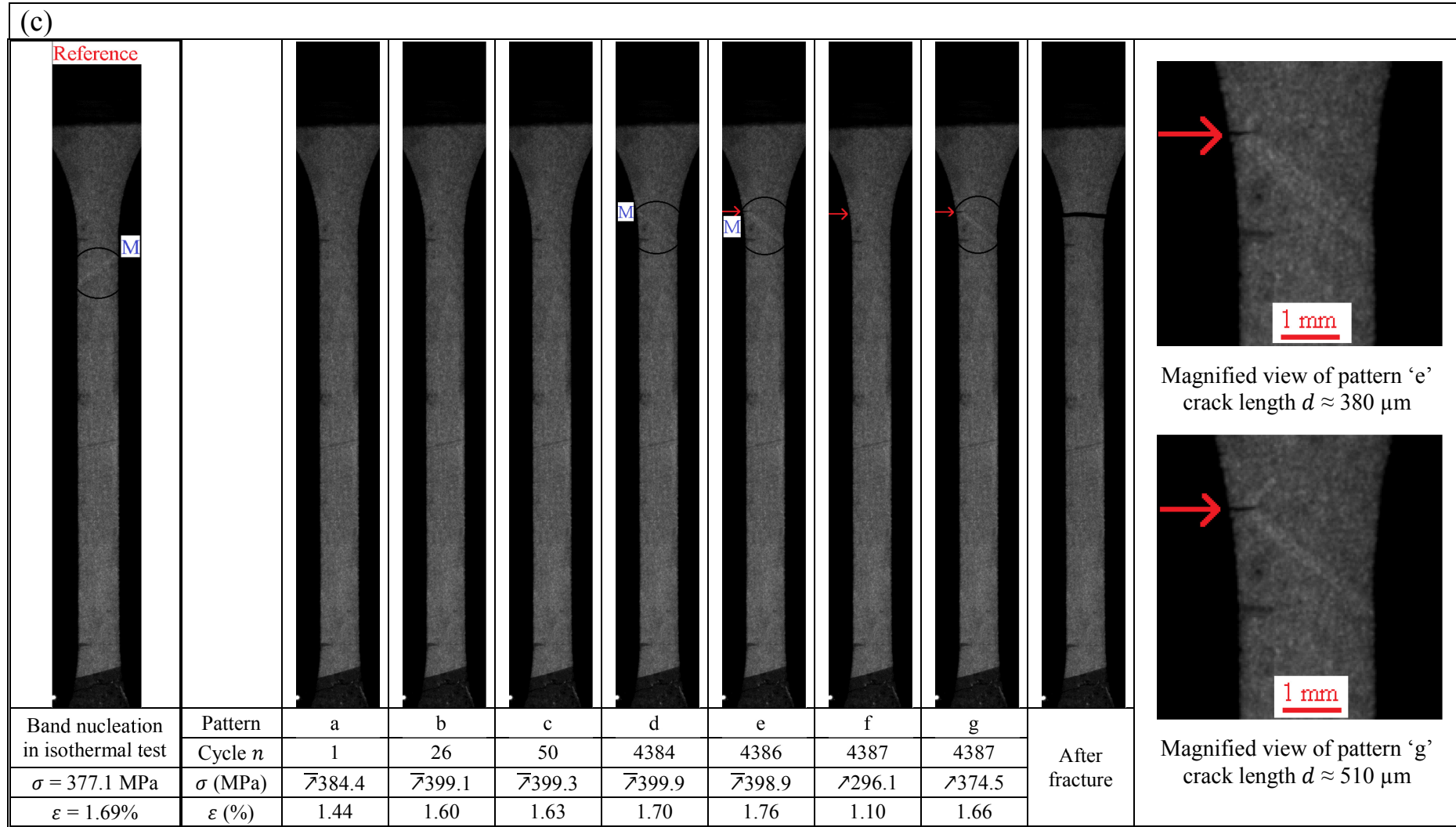


Fig. A6 *Continued*. (A thermocouple was attached to the lower end attempting to measure the average temperature.)



## References

- [1] S.W. Robertson, A.R. Pelton, R.O. Ritchie, Mechanical fatigue and fracture of Nitinol, *Int. Mater. Rev.* 57 (2012) 1–37. doi:10.1179/1743280411Y.0000000009.
- [2] J. Mohd Jani, M. Leary, A. Subic, M.A. Gibson, A review of shape memory alloy research, applications and opportunities, *Mater. Des.* 56 (2014) 1078–1113. doi:10.1016/j.matdes.2013.11.084.
- [3] M.J. Mahtabi, N. Shamsaei, M.R. Mitchell, Fatigue of Nitinol: The state-of-the-art and ongoing challenges, *J. Mech. Behav. Biomed. Mater.* 50 (2015) 228–254. doi:10.1016/j.jmbbm.2015.06.010.
- [4] G. Eggeler, E. Hornbogen, A. Yawny, A. Heckmann, M. Wagner, Structural and functional fatigue of NiTi shape memory alloys, *Mater. Sci. Eng. A.* 378 (2004) 24–33. doi:10.1016/j.msea.2003.10.327.
- [5] K.N. Melton, O. Mercier, Fatigue of NiTi thermoelastic martensites, *Acta Metall.* 27 (1979) 137–144. doi:10.1016/0001-6160(79)90065-8.
- [6] S. Miyazaki, T. Imai, Y. Igo, K. Otsuka, Effect of cyclic deformation on the pseudoelasticity characteristics of Ti-Ni alloys, *Metall. Trans. A.* 17 (1986) 115–120. doi:10.1007/BF02644447.
- [7] J. Van Humbeeck, Cycling effects, fatigue and degradation of shape memory alloys, in: *J. Phys. IV*, 1991: pp. C4–199. doi:http://dx.doi.org/10.1051/jp4:1991429.
- [8] Z. Moumni, A. Van Herpen, P. Riberty, Fatigue analysis of shape memory alloys: energy approach, *Smart Mater. Struct.* 14 (2005) S287–S292. doi:10.1088/0964-1726/14/5/017.
- [9] W. Predki, M. Klönne, A. Knopik, Cyclic torsional loading of pseudoelastic NiTi shape memory alloys: Damping and fatigue failure, *Mater. Sci. Eng. A.* 417 (2006) 182–189. doi:10.1016/j.msea.2005.10.037.
- [10] J. Olbricht, A. Yawny, A.M. Condó, F.C. Lovey, G. Eggeler, The influence of temperature on the evolution of functional properties during pseudoelastic cycling of ultra fine grained NiTi, *Mater. Sci. Eng. A.* 481–482 (2008) 142–145. doi:10.1016/j.msea.2007.01.182.
- [11] G. Kang, Q. Kan, L. Qian, Y. Liu, Ratchetting deformation of super-elastic and shape-memory NiTi alloys, *Mech. Mater.* 41 (2009) 139–153. doi:10.1016/j.mechmat.2008.09.001.
- [12] C. Maletta, E. Sgambitterra, F. Furgiuele, R. Casati, A. Tuissi, Fatigue of pseudoelastic NiTi within the stress-induced transformation regime: a modified Coffin–Manson approach, *Smart Mater. Struct.* 21 (2012) 112001. doi:10.1088/0964-1726/21/11/112001.
- [13] H. Yin, Y. He, Q. Sun, Effect of deformation frequency on temperature and stress oscillations in cyclic phase transition of NiTi shape memory alloy, *J. Mech. Phys. Solids.* 67 (2014) 100–128. doi:10.1016/j.jmps.2014.01.013.
- [14] Q. Kan, C. Yu, G. Kang, J. Li, W. Yan, Experimental observations on rate-dependent cyclic deformation of super-elastic NiTi shape memory alloy, *Mech. Mater.* 97 (2016) 48–58. doi:10.1016/j.mechmat.2016.02.011.
- [15] A. Rao, A.R. Srinivasa, J.N. Reddy, *Design of Shape Memory Alloy (SMA) Actuators*, Springer, Technology & Engineering, 2015, pp125–126.
- [16] S. Suresh, *Fatigue of Materials*, 2<sup>nd</sup> Edition, Cambridge University Press, 2001.
- [17] M. Frotscher, K. Neuking, R. Böckmann, K.-D. Wolff, G. Eggeler, In situ scanning electron microscopic study of structural fatigue of struts, the characteristic elementary building

- units of medical stents, *Mater. Sci. Eng. A.* 481-482 (2008) 160–165. doi:10.1016/j.msea.2007.04.129.
- [18] M. Frotscher, P. Nörtershäuser, C. Somsen, K. Neuking, R. Böckmann, G. Eggeler, Microstructure and structural fatigue of ultra-fine grained NiTi-stents, *Mater. Sci. Eng. A.* 503 (2009) 96–98. doi:10.1016/j.msea.2008.02.059.
- [19] L. Zheng, Y. He, Z. Moumni, Effects of Lüders-like bands on NiTi fatigue behaviors, *Int. J. Solids Struct.* 83 (2016) 28–44. doi:10.1016/j.ijsolstr.2015.12.021.
- [20] G. Kang, Q. Kan, C. Yu, D. Song, Y. Liu, Whole-life transformation ratchetting and fatigue of super-elastic NiTi Alloy under uniaxial stress-controlled cyclic loading, *Mater. Sci. Eng. A.* 535 (2012) 228–234. doi:10.1016/j.msea.2011.12.071.
- [21] D. Song, G. Kang, Q. Kan, C. Yu, C. Zhang, Damage-based life prediction model for uniaxial low-cycle stress fatigue of super-elastic NiTi shape memory alloy microtubes, *Smart Mater. Struct.* 24 (2015) 85007. doi:10.1088/0964-1726/24/8/085007.
- [22] Y. Zhang, J. Zhu, Z. Moumni, A. Van Herpen, W. Zhang, Energy-based fatigue model for shape memory alloys including thermomechanical coupling, *Smart Mater. Struct.* 25 (2016) 035042. doi:10.1088/0964-1726/25/3/035042.
- [23] J.F. Hallai, S. Kyriakides, Underlying material response for Luders-like instabilities, *Int. J. Plast.* 47 (2013) 1–12. doi:10.1016/j.ijplas.2012.12.002.
- [24] S. Miyazaki, T. Imai, K. Otsuka, Y. Suzuki, Lüders-like deformation observed in the transformation pseudoelasticity of a Ti-Ni alloy, *Scr. Metall.* 15 (1981) 853–856. doi:10.1016/0036-9748(81)90265-9.
- [25] J.A. Shaw, S. Kyriakides, Thermomechanical aspects of NiTi, *J. Mech. Phys. Solids.* 43 (1995) 1243–1281. doi:10.1016/0022-5096(95)00024-D.
- [26] J.A. Shaw, S. Kyriakides, On the nucleation and propagation of phase transformation fronts in a NiTi alloy, *Acta Mater.* 45 (1997) 683–700. doi:10.1016/S1359-6454(96)00189-9.
- [27] J.A. Shaw, S. Kyriakides, Initiation and propagation of localized deformation in elasto-plastic strips under uniaxial tension, *Int. J. Plast.* 13 (1997) 837–871. doi:10.1016/S0749-6419(97)00062-4.
- [28] Z.Q. Li, Q.P. Sun, The initiation and growth of macroscopic martensite band in nano-grained NiTi microtube under tension, *Int. J. Plast.* 18 (2002) 1481–1498. doi:10.1016/S0749-6419(02)00026-8.
- [29] Q.P. Sun, Z.Q. Li, Phase transformation in superelastic NiTi polycrystalline microtubes under tension and torsion—from localization to homogeneous deformation, *Int. J. Solids Struct.* 39 (2002) 3797–3809. doi:10.1016/S0020-7683(02)00182-8.
- [30] P. Feng, Q.P. Sun, Experimental investigation on macroscopic domain formation and evolution in polycrystalline NiTi microtubing under mechanical force, *J. Mech. Phys. Solids.* 54 (2006) 1568–1603. doi:10.1016/j.jmps.2006.02.005.
- [31] B. Reedlunn, C.B. Churchill, E.E. Nelson, J.A. Shaw, S.H. Daly, Tension, compression, and bending of superelastic shape memory alloy tubes, *J. Mech. Phys. Solids.* 63 (2014) 506–537. doi:10.1016/j.jmps.2012.12.012.
- [32] N.J. Bechle, S. Kyriakides, Localization in NiTi tubes under bending, *Int. J. Solids Struct.* 51 (2014) 967–980. doi:10.1016/j.ijsolstr.2013.11.023.
- [33] N.J. Bechle, S. Kyriakides, Evolution of localization in pseudoelastic NiTi tubes under biaxial stress states, *Int. J. Plast.* 82 (2016) 1–31. doi:10.1016/j.ijplas.2016.01.017.
- [34] L.C. Brinson, I. Schmidt, R. Lammering, Stress-induced transformation behavior of a polycrystalline NiTi shape memory alloy: micro and macromechanical investigations via in situ optical microscopy, *J. Mech. Phys. Solids.* 52 (2004) 1549–1571.

doi:10.1016/j.jmps.2004.01.001.

- [35] H. Kato, K. Sasaki, Transformation-induced plasticity as the origin of serrated flow in an NiTi shape memory alloy, *Int. J. Plast.* 50 (2013) 37–48. doi:10.1016/j.ijplas.2013.03.011.
- [36] W.W. Schmahl, J. Khalil-Allafi, B. Hasse, M. Wagner, A. Heckmann, C. Somsen, Investigation of the phase evolution in a super-elastic NiTi shape memory alloy (50.7at.%Ni) under extensional load with synchrotron radiation, *Mater. Sci. Eng. A.* 378 (2004) 81–85. doi:10.1016/j.msea.2003.11.081.
- [37] N. Nayan, D. Roy, V. Buravalla, U. Ramamurty, Unnotched fatigue behavior of an austenitic Ni–Ti shape memory alloy, *Mater. Sci. Eng. A.* 497 (2008) 333–340. doi:10.1016/j.msea.2008.07.025.
- [38] J. Zurbitu, R. Santamarta, C. Picornell, W.M. Gan, H.G. Brokmeier, J. Aurrekoetxea, Impact fatigue behavior of superelastic NiTi shape memory alloy wires, *Mater. Sci. Eng. A.* 528 (2010) 764–769. doi:10.1016/j.msea.2010.09.094.
- [39] E. Polatidis, N. Zotov, E. Bischoff, E.J. Mittemeijer, The effect of cyclic tensile loading on the stress-induced transformation mechanism in superelastic NiTi alloys: an in-situ X-ray diffraction study, *Scr. Mater.* 100 (2015) 59–62. doi:10.1016/j.scriptamat.2014.12.013.
- [40] P. Sedmák, P. Šittner, J. Pilch, C. Curfs, Instability of cyclic superelastic deformation of NiTi investigated by synchrotron X-ray diffraction, *Acta Mater.* 94 (2015) 257–270. doi:10.1016/j.actamat.2015.04.039.
- [41] N.B. Morgan, C.M. Friend, A review of shape memory stability in NiTi alloys, *J. Phys. IV Fr.* 11 (2001) Pr8–325–Pr8–332. doi:10.1051/jp4:2001855.
- [42] M. Rahim, J. Frenzel, M. Frotscher, J. Pfetzing-Micklich, R. Steegmüller, M. Wohlschlögel, et al., Impurity levels and fatigue lives of pseudoelastic NiTi shape memory alloys, *Acta Mater.* 61 (2013) 3667–3686. doi:10.1016/j.actamat.2013.02.054.
- [43] A.M. Condó, F.C. Lovey, J. Olbriht, C. Somsen, A. Yawny, Microstructural aspects related to pseudoelastic cycling in ultra fine grained Ni–Ti, *Mater. Sci. Eng. A.* 481–482 (2008) 138–141. doi:10.1016/j.msea.2007.05.106.
- [44] T. Simon, A. Kröger, C. Somsen, A. Dlouhy, G. Eggeler, On the multiplication of dislocations during martensitic transformations in NiTi shape memory alloys, *Acta Mater.* 58 (2010) 1850–1860. doi:10.1016/j.actamat.2009.11.028.
- [45] R. Delville, B. Malard, J. Pilch, P. Sittner, D. Schryvers, Transmission electron microscopy investigation of dislocation slip during superelastic cycling of Ni–Ti wires, *Int. J. Plast.* 27 (2011) 282–297. doi:10.1016/j.ijplas.2010.05.005.
- [46] A.R. Pelton, Nitinol Fatigue: A Review of Microstructures and Mechanisms, *J. Mater. Eng. Perform.* 20 (2011) 613–617. doi:10.1007/s11665-011-9864-9.
- [47] A.-L. Gloanec, G. Bilotta, M. Gerland, Deformation mechanisms in a TiNi shape memory alloy during cyclic loading, *Mater. Sci. Eng. A.* 564 (2013) 351–358. doi:10.1016/j.msea.2012.11.051.
- [48] M.A. Iadicola, J.A. Shaw, *Journal of Intelligent Material Systems and Structures The Effect of Uniaxial Cyclic Deformation on the Evolution of Phase Transformation Fronts in Pseudoelastic NiTi Wire*, *J. Intell. Mater. Syst. Struct.* 13 (2002) 143–155. doi:10.1106/104538902028220.
- [49] A. Heckmann, E. Hornbogen, Microstructure and pseudo-elastic low-cycle high amplitude fatigue of NiTi, *J. Phys. IV.* 112 (2003) 831–834. doi:10.1051/jp4:20031010.
- [50] A. Yawny, M. Sade, G. Eggeler, Pseudoelastic cycling of ultra-fine-grained NiTi shape-memory wires, *Zeitschrift Fur Met.* 96 (2005) 608–618. doi:10.3139/146.101078.
- [51] D. Roy, V. Buravalla, P.D. Mangalgiri, S. Allegavi, U. Ramamurty, Mechanical

characterization of NiTi SMA wires using a dynamic mechanical analyzer, *Mater. Sci. Eng. A*. 494 (2008) 429–435. doi:10.1016/j.msea.2008.04.052.

[52] Q. Kan, G. Kang, Constitutive model for uniaxial transformation ratchetting of super-elastic NiTi shape memory alloy at room temperature, *Int. J. Plast.* 26 (2010) 441–465. doi:10.1016/j.ijplas.2009.08.005.

[53] C. Yu, G. Kang, Q. Kan, D. Song, A micromechanical constitutive model based on crystal plasticity for thermo-mechanical cyclic deformation of NiTi shape memory alloys, *Int. J. Plast.* 44 (2013) 161–191. doi:10.1016/j.ijplas.2013.01.001.

[54] J.M. Young, K.J. Van Vliet, Predicting in vivo failure of pseudoelastic NiTi devices under low cycle, high amplitude fatigue, *J. Biomed. Mater. Res. - Part B Appl. Biomater.* 72 (2005) 17–26. doi:10.1002/jbm.b.30113.

[55] M.F.-X. Wagner, N. Nayan, U. Ramamurty, Healing of fatigue damage in NiTi shape memory alloys, *J. Phys. D. Appl. Phys.* 41 (2008) 185408. doi:10.1088/0022-3727/41/18/185408.

[56] D.C. Lagoudas, D.A. Miller, L. Rong, P.K. Kumar, Thermomechanical fatigue of shape memory alloys, *Smart Mater. Struct.* 18 (2009) 085021. doi:10.1088/0964-1726/18/8/085021.

[57] C. Maletta, E. Sgambitterra, F. Furgiele, R. Casati, A. Tuissi, Fatigue properties of a pseudoelastic NiTi alloy: Strain ratcheting and hysteresis under cyclic tensile loading, *Int. J. Fatigue*. 66 (2014) 78–85. doi:10.1016/j.ijfatigue.2014.03.011.

[58] S. Daly, G. Ravichandran, K. Bhattacharya, Stress-induced martensitic phase transformation in thin sheets of Nitinol, *Acta Mater.* 55 (2007) 3593–3600. doi:10.1016/j.actamat.2007.02.011.

[59] G. Murasawa, K. Kitamura, S. Yoneyama, S. Miyazaki, K. Miyata, A. Nishioka, et al., Macroscopic stress–strain curve, local strain band behavior and the texture of NiTi thin sheets, *Smart Mater. Struct.* 18 (2009) 055003. doi:10.1088/0964-1726/18/5/055003.

[60] X. Zhang, P. Feng, Y. He, T. Yu, Q. Sun, Experimental study on rate dependence of macroscopic domain and stress hysteresis in NiTi shape memory alloy strips, *Int. J. Mech. Sci.* 52 (2010) 1660–1670. doi:10.1016/j.ijmecsci.2010.08.007.

[61] K. Kim, S. Daly, Martensite Strain Memory in the Shape Memory Alloy Nickel-Titanium Under Mechanical Cycling, *Exp. Mech.* 51 (2011) 641–652. doi:10.1007/s11340-010-9435-2.

[62] E.A. Pieczyska, H. Tobushi, K. Kulasinski, Development of transformation bands in TiNi SMA for various stress and strain rates studied by a fast and sensitive infrared camera, *Smart Mater. Struct.* 22 (2013) 035007. doi:10.1088/0964-1726/22/3/035007.

[63] J.A. Shaw, Simulations of localized thermo-mechanical behavior in a NiTi shape memory alloy, *Int. J. Plast.* 16 (2000) 541–562. doi:10.1016/S0749-6419(99)00075-3.

[64] M.A. Iadicola, J.A. Shaw, Rate and thermal sensitivities of unstable transformation behavior in a shape memory alloy, *Int. J. Plast.* 20 (2004) 577–605. doi:10.1016/S0749-6419(03)00040-8.

[65] P. Šittner, Y. Liu, V. Novak, P. Šittner, Y. Liu, V. Novak, On the origin of Lüders-like deformation of NiTi shape memory alloys, *J. Mech. Phys. Solids*. 53 (2005) 1719–1746. doi:10.1016/j.jmps.2005.03.005.

[66] Y.J. He, Q.P. Sun, Effects of structural and material length scales on stress-induced martensite macro-domain patterns in tube configurations, *Int. J. Solids Struct.* 46 (2009) 3045–3060. doi:10.1016/j.ijsolstr.2009.04.005.

[67] Y.J. He, Q.P. Sun, Scaling relationship on macroscopic helical domains in NiTi tubes,

Int. J. Solids Struct. 46 (2009) 4242–4251. doi:10.1016/j.ijsolstr.2009.08.013.

[68] Y.J. He, Q.P. Sun, Rate-dependent domain spacing in a stretched NiTi strip, Int. J. Solids Struct. 47 (2010) 2775–2783. doi:10.1016/j.ijsolstr.2010.06.006.

[69] H. Ahmadian, S. Hatefi Ardakani, S. Mohammadi, Strain-rate sensitivity of unstable localized phase transformation phenomenon in shape memory alloys using a non-local model, Int. J. Solids Struct. 63 (2015) 167–183. doi:10.1016/j.ijsolstr.2015.02.049.

[70] R.D. James, K.F. Hane, Martensitic transformations and shape-memory materials, Acta Mater. 48 (2000) 197–222. doi:10.1016/s1359-6454(99)00295-5.

[71] K. Bhattacharya, Microstructure of Martensite: Why it Forms and How It Gives Rise to the Shape-Memory Effect, Oxford University Press, 2003.

[72] W. Zhang, Y. Jin, A. Khachaturyan, Phase field microelasticity modeling of heterogeneous nucleation and growth in martensitic alloys, Acta Mater. 55 (2007) 565–574. doi:10.1016/j.actamat.2006.08.050.

[73] J. Kundin, E. Pogorelov, H. Emmerich, Numerical investigation of the interaction between the martensitic transformation front and the plastic strain in austenite, J. Mech. Phys. Solids. 76 (2015) 65–83. doi:10.1016/j.jmps.2014.12.007.

[74] R.M. Tabanli, N.K. Simha, B.T. Berg, Mean stress effects on fatigue of NiTi, Mater. Sci. Eng. A. 273-275 (1999) 644–648. doi:10.1016/S0921-5093(99)00340-8.

[75] N. Nayan, V. Buravalla, U. Ramamurty, Effect of mechanical cycling on the stress-strain response of a martensitic Nitinol shape memory alloy, Mater. Sci. Eng. A. 525 (2009) 60–67. doi:10.1016/j.msea.2009.07.038.

[76] N.B. Morgan, J. Painter, A.J. Moffat, Mean strain effects and microstructural observation during in-vitro fatigue testing of NiTi, in: Proc. Int. Conf. Shape Mem. Superelastic Technol., 2004: pp. 3–10. <http://eprints.soton.ac.uk/49958/1/SMST2003.PDF>.

[77] J.E. Schaffer, D.L. Plumley, Fatigue performance of nitinol round wire with varying cold work reductions, J. Mater. Eng. Perform. 18 (2009) 563–568. doi:10.1007/s11665-009-9363-4.

[78] A.R. Pelton, J. Fino-Decker, L. Vien, C. Bonsignore, P. Saffari, M. Launey, et al., Rotary-bending fatigue characteristics of medical-grade Nitinol wire, J. Mech. Behav. Biomed. Mater. 27 (2013) 19–32. doi:10.1016/j.jmbbm.2013.06.003.

[79] S. Gupta, A.R. Pelton, J.D. Weaver, X.-Y. Gong, S. Nagaraja, High compressive pre-strains reduce the bending fatigue life of nitinol wire, J. Mech. Behav. Biomed. Mater. 44 (2015) 96–108. doi:10.1016/j.jmbbm.2014.12.007.

[80] S.W. Robertson, R.O. Ritchie, A fracture-mechanics-based approach to fracture control in biomedical devices manufactured from superelastic Nitinol tube, J. Biomed. Mater. Res. Part B Appl. Biomater. 84B (2008) 26–33. doi:10.1002/jbm.b.30840.

[81] A. Runciman, D. Xu, A.R. Pelton, R.O. Ritchie, An equivalent strain/Coffin-Manson approach to multiaxial fatigue and life prediction in superelastic Nitinol medical devices., Biomaterials. 32 (2011) 4987–93. doi:10.1016/j.biomaterials.2011.03.057.

[82] D. Song, G. Kang, Q. Kan, C. Yu, C. Zhang, Experimental observations on uniaxial whole-life transformation ratchetting and low-cycle stress fatigue of super-elastic NiTi shape memory alloy micro-tubes, Smart Mater. Struct. 24 (2015) 075004. doi:10.1088/0964-1726/24/7/075004.

[83] D. Tolomeo, S. Davidson, M. Santinoranont, Cyclic properties of superelastic nitinol: design implications, in: SMST-2000 Proc. Int. Conf. Shape Mem. Superelastic Technol. (SM Russell AR Pelt. Eds.), Pacific Grove, California, USA, 2001: pp. 471–476.

[84] A. Pelton, V. Schroeder, M.R. Mitchell, X.-Y. Gong, M. Barney, S.W. Robertson,

- Fatigue and durability of Nitinol stents, *J. Mech. Behav. Biomed. Mater.* 1 (2008) 153–164. doi:10.1016/j.jmbbm.2007.08.001.
- [85] M. Frotscher, S. Wu, T. Simon, C. Somsen, A. Dlouhy, G. Eggeler, Elementary Deformation and Damage Mechanisms During Fatigue of Pseudoelastic NiTi Microstents, *Adv. Eng. Mater.* 13 (2011) B181–B186. doi:10.1002/adem.201180001.
- [86] S.W. Robertson, M. Launey, O. Shelley, I. Ong, L. Vien, K. Senthilnathan, et al., A statistical approach to understand the role of inclusions on the fatigue resistance of superelastic Nitinol wire and tubing, *J. Mech. Behav. Biomed. Mater.* 51 (2015) 119–131. doi:10.1016/j.jmbbm.2015.07.003.
- [87] K. Gall, J. Tyber, G. Wilkesanders, S.W. Robertson, R.O. Ritchie, H.J. Maier, Effect of microstructure on the fatigue of hot-rolled and cold-drawn NiTi shape memory alloys, *Mater. Sci. Eng. A.* 486 (2008) 389–403. doi:10.1016/j.msea.2007.11.033.
- [88] E. Choi, T. Nam, Y.-S. Chung, Variation of mechanical properties of shape memory alloy bars in tension under cyclic loadings, *Mater. Sci. Eng. A.* 527 (2010) 4412–4417. doi:10.1016/j.msea.2010.03.098.
- [89] V.L. Sateesh, P. Senthilkumar, G.N. Dayananda, A posteriori processing for estimation of low cycle fatigue failure in SESMA wires, *Mater. Sci. Eng. A.* 594 (2014) 212–217. doi:10.1016/j.msea.2013.11.069.
- [90] G. Tan, Y. Liu, P. Sittner, M. Saunders, Lüders-like deformation associated with stress-induced martensitic transformation in NiTi, *Scr. Mater.* 50 (2004) 193–198. doi:10.1016/j.scriptamat.2003.09.018.
- [91] G. Tan, Y. Liu, Comparative study of deformation-induced martensite stabilisation via martensite reorientation and stress-induced martensitic transformation in NiTi, *Intermetallics.* 12 (2004) 373–381. doi:10.1016/j.intermet.2003.11.008.
- [92] Y. Liu, The superelastic anisotropy in a NiTi shape memory alloy thin sheet, *Acta Mater.* 95 (2015) 411–427. doi:10.1016/j.actamat.2015.03.022.
- [93] A. Ahadi, Q. Sun, Effects of grain size on the rate-dependent thermomechanical responses of nanostructured superelastic NiTi, *Acta Mater.* 76 (2014) 186–197. doi:10.1016/j.actamat.2014.05.007.
- [94] A. Ahadi, Q. Sun, Grain size dependence of fracture toughness and crack-growth resistance of superelastic NiTi, *Scr. Mater.* 113 (2016) 171–175. doi:10.1016/j.scriptamat.2015.10.036.
- [95] S. Miyazaki, K. Mizukoshi, T. Ueki, T. Sakuma, Y. Liu, Fatigue life of Ti–50 at.% Ni and Ti–40Ni–10Cu (at.%) shape memory alloy wires, *Mater. Sci. Eng. A.* 273–275 (1999) 658–663. doi:10.1016/S0921-5093(99)00344-5.
- [96] H. Tobushi, T. Nakahara, Y. Shimeno, T. Hashimoto, Low-Cycle Fatigue of TiNi Shape Memory Alloy and Formulation of Fatigue Life, *J. Eng. Mater. Technol.* 122 (2000) 186. doi:10.1115/1.482785.
- [97] C. Morin, Z. Moumni, W. Zaki, Thermomechanical coupling in shape memory alloys under cyclic loadings: Experimental analysis and constitutive modeling, *Int. J. Plast.* 27 (2011) 1959–1980. doi:10.1016/j.ijplas.2011.05.005.
- [98] C. Grabe, O.T. Bruhns, On the viscous and strain rate dependent behavior of polycrystalline NiTi, *Int. J. Solids Struct.* 45 (2008) 1876–1895. doi:10.1016/j.ijsolstr.2007.10.029.
- [99] Y.J. He, Q.P. Sun, Frequency-dependent temperature evolution in NiTi shape memory alloy under cyclic loading, *Smart Mater. Struct.* 19 (2010) 115014. doi:10.1088/0964-1726/19/11/115014.

- [100] E.A. Pieczyska, S.P. Gadaj, W.K. Nowacki, H. Tobushi, Phase-Transformation Fronts Evolution for Stress- and Strain-Controlled Tension Tests in TiNi Shape Memory Alloy, *Exp. Mech.* 46 (2006) 531–542. doi:10.1007/s11340-006-8351-y.
- [101] X. Xie, Q. Kan, G. Kang, F. Lu, K. Chen, Observation on rate-dependent cyclic transformation domain of super-elastic NiTi shape memory alloy, *Mater. Sci. Eng. A.* 671 (2016) 32–47. doi:10.1016/j.msea.2016.06.045.





**Titre :** Analyse Multi-échelle de la Fatigue des Alliages à Mémoire de Forme

**Mots clés :** Alliage à Mémoire de Forme; Pseudoélasticité; Transformation Martensitique; Fatigue; Bandes de Lüders.

**Résumé:** L'Alliage à Mémoire de Forme (AMF) est un matériau intelligent ayant de nombreuses applications dans l'industrie aéronautique, le génie civil, ainsi que dans le domaine biomédical. Dans toutes ces applications, le matériau est soumis à un chargement cyclique ce qui le rend vulnérable vis-à-vis du phénomène de la fatigue. Une des questions importantes dans l'étude de la fatigue de l'AMF polycristallin est l'interaction entre l'endommagement local et la transformation de phase martensitique; cette transformation se déroule dans un mode homogène macroscopique ou un mode hétérogène se traduisant par la formation de bandes de Lüders en raison de la localisation de la déformation et du changement de phase. La formation et l'évolution de ces bandes influence fortement les mécanismes physiques de déformation ainsi que l'endommagement par fatigue du matériau.

Dans la littérature, on ne trouve pas d'études permettant de faire le lien entre la formation et l'évolution des bandes de localisation et la fatigue du matériau. Dans cette thèse, des expériences systématiques de fatigue en traction sont réalisées sur les éprouvettes pseudo-élastiques du Nickel-Titane avec des observations optiques in-situ de l'évolution des macro-bandes. Ces observations ont permis de retracer l'histoire de la déformation locale dans les zones où la rupture se produit. Ces résultats expérimentaux permettent de mieux comprendre le comportement de fatigue ainsi que sa dépendance par rapport à la contrainte appliquée ainsi que la fréquence du chargement. En particulier, il a été prouvé que la déformation locale résiduelle représente un meilleur indicateur de l'endommagement du matériau que la déformation résiduelle nominale/globale de la structure.

**Title :** Multi-scale Analysis of the Fatigue of Shape Memory Alloys

**Keywords:** Shape Memory Alloy; Pseudoelasticity; Martensitic Transformation; Fatigue; Lüders-like Bands.

**Abstract:** Shape Memory Alloy (SMA) is a typical smart material having many applications from aerospace industry, mechanical and civil engineering, to biomedical devices, where the material's fatigue is a big concern. One of the challenging issues in studying the fatigue behaviors of SMA polycrystals is the interaction between the material damage and the martensitic phase transformation which takes place in a macroscopic homogeneous mode or a heterogeneous mode (forming macroscopic patterns (Lüders-like bands) due to the localized deformations and localized heating/cooling). Such pattern formation and evolution imply the governing physical mechanisms in the material system such as the fatigue process, but there is still no fatigue study of SMAs by tracing the macro-band patterns and the local material responses.

To bridge this gap, systematic tensile fatigue experiments are conducted on pseudoelastic NiTi polycrystalline strips by in-situ optical observation on the band-pattern evolutions and by tracing the deformation history of the cyclic phase transformation zones where fatigue failure occurs. These experimental results help to better understand the stress- and frequency-dependent fatigue behaviors. Particularly, it is found that the local residual strain rather than the structural nominal/global residual strain is a good indicator on the material's damage leading to the fatigue failure, which is important for understanding and modeling the fatigue process in SMAs.